

UNIVERSITY OF OKLAHOMA

GRADUATE COLLEGE

FABRICATION, CHARACTERIZATION AND MODELING OF ALIGNED
POLYACRYLONITRILE-BASED ELECTROSPUN CARBON NANOFIBERS

A DISSERTATION

SUBMITTED TO THE GRADUATE FACULTY

in partial fulfillment of the requirements for the

Degree of

DOCTOR OF PHILOSOPHY

By

MEHMET SELIM DEMIRTAS

Norman, Oklahoma

2018

FABRICATION, CHARACTERIZATION AND MODELING OF ALIGNED
POLYACRYLONITRILE-BASED ELECTROSPUN CARBON NANOFIBERS

A DISSERTATION APPROVED FOR THE
SCHOOL OF AEROSPACE AND MECHANICAL ENGINEERING

BY

Dr. Mrinal C. Saha, Chair

Dr. M. Cengiz Altan (Co-Chair)

Dr. Zahed Siddique

Dr. Yingtao Liu

Dr. Shivakumar Raman

© Copyright by MEHMET SELIM DEMIRTAS 2018

All Rights Reserved.

ACKNOWLEDGEMENTS

I would like to express my gratitude to all those people giving me the possibility to complete this dissertation. First, I would like to acknowledge The Minister of National Education Turkey for the financial support.

I would like to thank Dr. Mrinal C. Saha and Dr. M. Cengiz Altan for advising, encouragement, and insightful suggestion during my research work at The University of Oklahoma. I wish to thank Dr. Shivakumar Raman, Dr. Zahed Siddique, and Dr. Yingtao Liu for their comments, suggestions, and serving on my dissertation committee. I would like to thank former graduate student Dr. Bipul Barua who initiated the research and trained me on using all test equipment. I also would like to thank Dr. Yingtao Liu for training on how to use the SEM and providing its use it whenever I needed. I owe gratitude to Dr. Preston Larson for sputter coating my SEM samples.

I would like to express my gratitude to Mr. Billy Mays and Mr. Gregory Williams for helping me at machine shop. I would like to thank Dr. M. Akif Yalcinkaya, Dr. Orhan Ozelik, and Gorkem E. Guloglu for not only helping my research but also being excellent friends. The experimental research presented in this dissertation would not have been compiled without their help. I would like to express my gratitude to all of the AME faculty and staff. My deepest appreciations are going to my family and friends for their long-standing support, motivation, and encouragement.

TABLE OF CONTENTS

ACKNOWLEDGEMENTS.....	iv
TABLE OF CONTENTS.....	v
LIST OF TABLES.....	viii
LIST OF FIGURES.....	ix
ABSTRACT.....	xvi
Chapter 1 : INTRODUCTION.....	1
1.1 Carbon Fibers.....	1
1.1.1 Pitch.....	3
1.1.2 Polyacrylonitrile (PAN).....	6
1.1.3 Current Status of Carbon Fibers and Limitation of Further Improvement.....	8
1.1.4 Vapor Grown Carbon Nanofibers (VGCFNs).....	11
1.1.5 Carbon Nanotubes (CNTs).....	12
1.2 Electrospinning.....	14
1.2.1 History of Electrospinning.....	14
1.2.2 Fundamental Theory.....	15
1.2.3 Applications of Electrospun Nanofibers.....	17
1.2.4 Electrospun Carbon Nanofibers (ECNFs) and Fabrication.....	17
1.2.5 Post Electrospinning Stretching and Heat Treatment.....	19
1.3 Scope of the Work.....	20
Chapter 2 : ELECTROSPINNING DESIGN and PROCESS PARAMETERS.....	21
2.1 Introduction.....	21
2.3 Electrospinning Setup Design.....	25
2.4 Process Parameters.....	27
2.4.1 Solution Parameters.....	27
2.4.2 Governing Parameters.....	29
2.4.3. Ambient Parameters.....	31
2.5 Relative Humidity Effects on Fiber Properties.....	31
2.5.1 Experimental.....	32
2.5.1.1 Materials and Processing.....	32
2.5.1.2 Characterizations.....	33
2.5.2. Results.....	33
2.6 Chapter Conclusion.....	38

Chapter 3 : INVESTIGATION OF COLLECTOR DESIGN AND SPEED EFFECTS ON FIBER PROPERTIES.....	39
3.1 Introduction.....	39
3.2 Electric Field Analysis with Finite Element Method (FEA)	40
3.3 Experimental.....	40
3.3.1 Electrospinning Process.....	40
3.3.2 Stabilization and Carbonization.....	41
3.3.3 Fiber Angle and Diameter Distribution Characterization.....	42
3.3.4 Fiber Mat Porosity Characterization.....	42
3.3.5 Mechanical Test Sample Preparation.....	43
3.3.6 Tensile Properties Measurement.....	45
3.4 Results and Discussion	46
3.4.1 Effect of Collector Design on Electric Field.....	46
3.4.1.1 Wire Opening Effect on Electric Field	46
3.4.1.2 Collector Geometry Effect on Electric Field	46
3.4.2 Collector Speed Effects on Fiber Mat Porosity	49
3.4.3 Collector Speed and Geometry Effects on Diameter Distribution and Fiber Alignment of Electrospun, Stabilized and Carbonized Fiber	50
3.4.4 Mechanical Properties of Electrospun, Stabilized and Carbonized Nanofibers	55
3.5 Chapter Conclusions	57
Chapter 4 : INVESTIGATION OF ELECTRODE GEOMETRY	58
4.1. Introduction.....	58
4.2 Finite Element Analysis of Different Electrode Geometry.....	60
4.3 Experimental.....	61
4.3.1 Optic and High-Speed Camera Analysis	61
4.3.2 Taylor Cone Straight Jet Formation Analysis.....	61
4.3.3 Fiber Angle and Diameter Analysis.....	62
4.4 Results and Discussion	62
4.4.1 Electrode Geometry Effects on Electric Field Distribution.....	62
4.4.2 Electrode Geometry Effect on Taylor Cone and Jet Formation	65
4.4.3 Electrode Geometry Effect on Morphology. Diameter, and Alignment.....	71
4.4.4 Mechanical Properties.....	74
4.5 Chapter Conclusions	75

Chapter 5 : STRETCHING AND PRE-STRESS CONDITION EFFECTS ON ELECTROSPUN POLYACRYLONITRILE AND STABILIZED NANOFIBERS	77
5.1 Introduction.....	77
5.2 Experimental.....	79
5.2.1 Hot Stretching	79
5.2.2 Stabilization by Applying Pre-Stress.....	80
5.2.3 In situ Characterization	81
5.2.4 Powder X-ray Diffraction (XRD) Characterization.....	82
5.3 Results and Discussion	82
5.3.1 Hot Stretching Effects on Fiber Diameter of Electrospun PAN Nanofibers	82
5.3.2 Tensile Properties of Stretched PAN Nanofibers	84
5.3.3 Crystallinity Analysis.....	86
5.3.4 Investigation of Stretching Effect on Stabilization Reaction.....	88
5.3.5 Pre-Loading Effects on Mechanical Properties	94
5.4 Chapter Conclusions	95
Chapter 6 : SINGLE FIBER STRENGTH CALCULATION FROM BUNDLE TEST ...	97
6.1 Introduction.....	97
6.2 Statistical Carbon Fiber (CF) Strength Analysis	99
6.2.1 Weibull Distribution	99
6.2.2 Statistical Strength Analysis of Single CF.....	100
6.2.2 Statistical Strength Analysis of CF Bundle	101
6.2.2.1 Slope Method.....	102
6.2.2.2 Maximum Point Method.....	103
6.2.2.3 Non-linear Elasticity Effect	104
6.3 Experimental.....	105
6.3.1 Sample Preparation	105
6.4 Results and Discussion	107
6.4.1 Calculation of Single Filament CF Tensile Strength from Bundle Test.....	107
6.4.2 Estimation of Single Filament ECFNF Tensile Strength from Bundle Test.....	112
6.4.3 Alignment Effect on Tensile Strength of ECFNF.....	118
6.5 Chapter Conclusions	122
Chapter 7 : CONCLUDING REMARKS	124
7.1 Conclusions.....	124
7.2 Recommendations for Future Work.....	126

References.....	128
-----------------	-----

LIST OF TABLES

Table 2.1 Schematic of common type rotating collector equipped electrospinning setups with and their advantages and disadvantages.	24
Table 2.2 Summary of diameter distribution of as-spun, stabilized and carbonized nanofibers at different RH.	36
Table 2.3 Tensile properties of as-spun, stabilized and carbonized respected to RH.....	37
Table 3.1 Porosity of carbon nanofibers films for different collector geometries, derived by employing image method.....	50
Table 3.2 Summary of diameter distribution of as-spun, stabilized, and carbonized nanofibers at different rpm.....	54
Table 3.3 Tensile Properties of As-Spun, Stabilized and Carbonized Respected to rpm. .	57
Table 4.1 Summary of optic camera analysis of Taylor cone angle, area and jet type at different flow rates.....	67
Table 4.2 Summary of high speed camera image analysis of jet.....	70
Table 4.3 Summary of average diameter for different needle tip and fiber alignment.....	74
Table 5.1 Average diameter in nanometers of electrospun, stabilized nanofibers respect to stretching ratio.	83
Table 5.2 Crystallinity calculation results based on powder XRD of PAN nanofibers at different stretched ratio and unstretched.....	86
Table 5.3 Cyclization peak temperature and cyclization heat derived by calculating the area under the curve from DSC result in nitrogen for PAN electrospun nanofiber stretched and unstretched.....	90

Table 5.4 Summary of tensile test results of stabilized nanofibers.....	95
Table 6.1 Summary of Weibull bundle analysis of AS4 CF.....	111
Table 6.2 Summary of Weibull bundle analysis of ECNF.	115
Table 6.3 Single filament CNF test result from literature.	116
Table 6.4 Tensile strength of ECNF derived from bundle test as a function of standard deviation of the fiber angle distributions.	121

LIST OF FIGURES

Figure 1.1 Schematic of the melt spinning process and variables [7].	5
Figure 1.2 Chemical structure of PAN.	7
Figure 1.3 Schematic view of manufacturing steps of PAN-based CFs from precursor.....	8
Figure 1.4 Schematic view of major types of structural imperfections in CFs [16].	10
Figure 1.5 Tensile strength of CFs as a function diameter [27].....	11
Figure 1.6 Schematic of growing filaments formed by catalytic particles [28].....	12
Figure 1.7 Schematic view of SWCNT and MWCNT [32].....	13
Figure 1.8 Number of scientific articles published about electrospinning (Source: Compendex, keyword: electrospinnig).	15
Figure 1.9 A schematic representation of electrospinning consisting of a syringe and pump, high voltage source and grounded collector.	16
Figure 1.10 SEM images of (a) VGCNF [75] (b) helically coiled CNTs [76] (c) ECNFs [77].	18
Figure 2.1 Typical electric field manipulating approaches of electrospinning systems: (a) Auxiliary parallel plates [80]. (b) Secondary electric field [81]. (c) Modified parallel	

electrode [82]. (d) Parallel auxiliary electrode arrangement. (e) Electric field profile from spinneret to the parallel electrodes [46].	23
Figure 2.2 3D model of the shaft design with dimensions in mm.	26
Figure 2.3 Schematic view of the electrospinning setup.	26
Figure 2.4 Actual photography of the electrospinning setup and components.	27
Figure 2.5 SEM images of PBS electrospun nanofibers. The concentration (a) 14 wt% (b) 17 wt% [95].	29
Figure 2.6 Favorable flow rate range for continuous flow jet as a function of applied voltage for 10 wt% PAN in DMF [48].	30
Figure 2.7 Effect of RH on the surface morphology of as-spun nanofiber produced from 10% PAN/DMF solution [109].	34
Figure 2.8 SEM images of electrospun nanofibers and diameter distribution at various RH. (a) 22% (b) 40% and (c) 60%.	35
Figure 2.9 Stress strain curve PAN nanofiber where RH is 22%, 40% and 60%.	36
Figure 3.1 Collector types copper foil thickness 0.1 mm and 12 mm wide, mesh wire diameter 0.3 mm opening size 2 mm, wire diameter 0.3 mm.	41
Figure 3.2 Image analysis method that followed for porosity calculation by converting the SEM images to binary.	43
Figure 3.3 (a) Cutting cartoon board window frame via the mold (b) placing double-sided tape on both ends of the frame (c) sticking fibers on tape by gently pressing foil (d) Trimming yarn from top and bottom sides of the window frame (e) removing collector (f) closing other side of the double-sided tape with cartoon slides so that it will not stick test fixture.	44

Figure 3.4 FEA simulation results of electric field distribution for wire type of collector wire diameter is 0.3 mm opening size (a) 1 mm (b) 2 mm (c) 3 mm.	47
Figure 3.5 Electric field density distribution of foil (a), mesh (b) and wire (c) type of collector.....	48
Figure 3.6 Electric field change along the collector surface for foil, mech and wire type of collector.....	49
Figure 3.7 Porosity of nanofiber film as a function of collector speed for foil type of collector calculated by using apparent density method.	50
Figure 3.8 Histograms of PAN nanofibers angle distributions relative to mean orientation, a-c copper foil collector, d-) metal mesh and e-) wire collector. Red arrows indicate the rotation direction of the disc.	53
Figure 3.9 Standard deviation of electrospun PAN angle distributions as the function of collector plate speed.....	54
Figure 3.10 Stress-strain curve of as-spun fibers fabricated at 1500 rpm.	55
Figure 3.11 Stress strain curve carbonized nanofiber for three different collector geometry where rpm is 1500.....	56
Figure 4.1 Scheme of the different types spinneret; (a) flat; [125](b) twisted wire electrospinning setup, the polymer solution is fed to the top; [129](c) stepped pyramid; [131](d) metal roller type spinneret and system components; (d-1) the roller; (d-2) solution reservoir; (d-3) fiber formation direction; (d-4) deposited fibers; (d-5) collector [130].....	59
Figure 4.2 Schematic view of different electrode types, a- blind needle, b- flash, c- protruded.	60

Figure 4.3 High speed camera setup.	61
Figure 4.4 FEA result of electric field intensity from electrode through the collector, potential difference is 15kv for needle, flash type OD= 2, 6, and 12 mm.	62
Figure 4.5 FEA plots of electric field intensity around needle tip where the potential difference is 15kv for (a) needle, (b) flash, and (b) protruded type of electrode.	63
Figure 4.6 Electric field intensity from electrode through the collector where potential difference is 15kv for needle, flash, and protruded type of electrode.	64
Figure 4.7 FEA result of electric field intensity as a function of applied voltage from electrode through the collector.	65
Figure 4.8 Taylor cone shape at 13 μ l/min flow rate and 15kV for (a) needle tip, (b) flash (c) protruded.	66
Figure 4.9 Demonstration of Taylor cone half angle α , straight jet length, and θ cone angle.	66
Figure 4.10 High speed camera image of (a) needle, (b) flash, and (c) protruded type of electrode (15 kV, 13 μ l/min flow rate, 1000 fps, and 100 μ s exposure).	68
Figure 4.11 High speed camera image of needle, flash, and protruded type of electrode (19 kV, 13 μ l/min flow rate, 1000 fps, and 100 μ s exposure).	69
Figure 4.12 Fiber mat images deposited with (a) needle tip, (b) flash and (c) sputtered electrode (13 μ l/min flow rate, 15 kV, and 600 rpm)	71
Figure 4.13 SEM images of PAN yarn fabricated with (a) needle, (b) flash, and (c) protruded type of electrode.	72
Figure 4.14 Morphology SEM images of PAN yarn fabricated with (a) needle, (b) flash, and (c) protruded type of electrode.	73

Figure 4.15 Stress-strain curve of electrospun PAN yarn fabricated with needle, flash, and protruded type of electrode (600 rpm collector speed, 15 kV applied voltage, 13 μ l/min flow rate).	75
Figure 5.1 Schematic explanation of the chemical reaction during stabilization of PAN fiber [142].	78
Figure 5.2 Fiber stretching process (5 mm/min strain rate and in 135°C Instron 5969 environmental chamber).	79
Figure 5.3 Stress-Strain curve of PAN electrospun fiber during stretching at 135°C.	80
Figure 5.4 Illustration of stabilization under pre-stresses conditions. Dead loads are hanged on fiber depending on corresponding stresses.....	81
Figure 5.5 Calculation method of the crystallinity from XRD data (a) baseline to determine pikes (b) pike area [142].	82
Figure 5.6 SEM images of electrospun PAN nanofibers with stretching ratios, $\lambda=0, 1, 2,$ and 3.....	84
Figure 5.7 Tensile test results of PAN nanofiber at different stretching ratios.	85
Figure 5.8 XRD pattern of PAN nanofiber yarn at different stretching ratio.	87
Figure 5.9 DSC plots of PAN electrospun nanofiber in nitrogen heating at 5 °C/min.	88
Figure 5.10 DSC plots of PAN electrospun nanofiber in air heating at 5 °C/min.	89
Figure 5.11 Derivative of TGA plot in nitrogen for electrospun PAN stretched and unstretched nanofibers.	90
Figure 5.12 PAN unstretched electrospun nanofiber shrinkage behavior during stabilization at different constant loads (5 °C/min ramp, 180 min isothermal at 260 °C). 92	

Figure 5.13 PAN unstretched and stretched electrospun nanofiber shrinkage behavior during stabilization under 1 MPa tension(5 °C/min ramp, 180 min isothermal at 260 °C).	93
Figure 5.14 Amount of shrinkage as a function of tension during stabilization for unstretched and stretched PAN electrospun nanofibers.	93
Figure 5.15 DMA in situ stabilization strain derivative of time constant load 1 MPa	94
Figure 6.1 Schematic showing of tensile test fixture and mounting of single filament fibers.	98
Figure 6.2 Misalignment of single fiber mounting on window frame.	99
Figure 6.3 Effect of cutting direction on stress distribution for the single filament test window frame. (a) cutting the side from perpendicular to the face (b) cutting the side from inside.	105
Figure 6.4 800x magnified SEM images of (a) ECNFs (b) AS4 CF.	106
Figure 6.5 AS4 bundle test sample preparation (a) aluminum sample holder 2” by 1” and 1/8” thick (b) gluing the bundle between two aluminum plate inside the cylindrical channel with epoxy (c) bundle test sample with 6 mm gauge length which is adjustable.	107
Figure 6.6 Stress-strain curve of 3k filament AS-4 micro carbon fiber.	109
Figure 6.7 Strength distribution of single AS-4 micro carbon fiber.	109
Figure 6.8 Effect of non-linear elasticity on AS4 3k bundle test, α range is -4 to 4.	110
Figure 6.9 Stress-strain curve of 1500 filament ECNFs (average diameter 204 nm, .2.7° standard deviation of the angle distribution, and gauge length 6mm).	113

Figure 6.10 Effect of non-linear elasticity on theoretical stress-strain curve of ECFN bundle (average diameter 204 nm, and 6mm gauge length) 1.5k bundle test, α (non-linear elasticity coefficient) range is -4 to 4.....	114
Figure 6.11 Effect of gauge length on Weibull modulus of PAN base CF T1000GB [172].	117
Figure 6.12 Failure strength estimation from bundle test as a function of gauge length for ECFN.	118
Figure 6.13 Effect of standard deviation of the angle distribution on ECFN theoretical stress-strain curve of ECFN bundle.	119
Figure 6.14 Weibull shape parameter of ECFN derived from bundle test as a function average fiber angle.	120
Figure 6.15 Weibull shape modulus of ECFN derived from bundle test as a function standard deviation of the angle distributions.	120

ABSTRACT

Electrospinning is widely used to produce carbon nanofiber from polyacrylonitrile (PAN). The alignment of fibers may vary depending on electrospinning condition. In this study, an electrospinning setup is developed to fabricate aligned and uniform yarns from PAN, employing an adjustable rotating disc. Effects of relative humidity (RH) on fiber diameter and mechanical properties of electrospun, stabilized and carbonized nanofibers are investigated. Average fiber diameter increases from 365 nm to 602 nm by increasing RH 22% to 60%. Additionally, mechanical properties are reduced by increasing RH. Nanofibers are generated at low RH show poor mechanical properties. 22% RH yields the best mechanical properties.

Collector geometry and rotating speed influence electrospun nanofiber alignment. The nanofiber diameter distribution, porosity, orientation, and mechanical properties are investigated. A unique approach is adopted to test the nanofiber films in tension using a dynamic mechanical analyzer (DMA). Furthermore, 2-dimensional FEM analysis is performed to investigate electric field distribution around the collector. It is observed that speed of the rotating disc can help improve the alignment of nanofibers in the film. It is also absolved that the electric field is more intense and uniform on the collector surface for wire and mesh type collectors compared to foil collectors. Nanofibers electrospun with wire type collector show the highest alignment due to intense uniform electric field and tensile properties of carbonized nanofiber films. Electrode geometry is another electrospinning element that influences the fiber alignment. Three different tip electrode systems are investigated; single blind needle, flash needle, where the needle is located in a copper cylinder and completely flush with the edge of the cylinder, and protruded needle,

where the needle passes through a copper cylinder and protrudes 0.5 mm past the edge of the cylinder. Similarly, 2D FEM is studied to obtain electric field distribution of the needle region. The alignment and diameter of nanofibers vary by changes in the needle system when all other electrospinning parameters are kept constant. The flash and protruded type of electrode yields more uniform and better fiber alignment. Furthermore, Taylor cone and straight jet formation dependence on flow rate and applied voltage are investigated using a high speed camera. an average fiber diameter of 422 nm is obtained for needle type while 389 nm is obtained for the protruded needle and fiber alignment was also improved with varying electrode types.

Stabilization conditions influence mechanical properties of carbon nanofibers. The effects of hot drawing of electrospun PAN nanofiber yarns and pre-stress during stabilization on the mechanical properties of stabilized yarns is investigated. The as-spun PAN nanofibers are mechanically stretched to stretch ratios (λ) of 1, 2 and 3 at 135 °C and subsequently stabilized at 260°C in air for 180 min under different mechanical pre-stress conditions, up to 5 MPa. Fiber diameter distribution is investigated via SEM, and tensile properties are measured via dynamic DMA. It has been found that stretching significantly improves the tensile strength of electrospun and stabilized fibers, while decreasing average fiber diameter. Pre-stress during stabilization has an important role on mechanical properties. Unstretched fibers show weaker mechanical properties comparing to stretched fibers. A tensile strength of about 401 MPa is obtained for $\lambda=2$ produced at 1 MPa pre-stress while stabilizing, compared to about 191 MPa for $\lambda=0$.

Determining mechanical properties of a single filament carbon nanofibers is an extremely complicated and requires expensive equipment. A statistical model is developed to determine single filament tensile strength from bundle test. A Weibull statistical model

is modified to analysis to estimate tensile strength of single filament electrospun carbon nanofiber from bundle test. The tensile strength is obtained 2.52 GPa where the standard deviation of fiber angle distribution is 2.7° . Tensile strength is calculated 1.66 GPa for standard deviation 15.8° while 2.7° is 2.52 GPa. A relation between Weibull parameters and alignment is obtained from experimental results. Tensile strength and failure strain of 0° standard deviation is calculated from estimated Weibull parameters.

Chapter 1 : INTRODUCTION

Fibers have been used since the beginning of civilization, and their use has grown over the years due to their improving properties. Early civilizations utilized natural fibers in many ways, including uses in structural materials and textile. The discovery of synthetic fibers has significantly increased the demand of high performance applications, and led to new applications of fibers in many industrial areas. Due to manufacturing challenges, early man-made fibers had micron level diameters. Significant changes have taken place in today's technology due to the benefits of nanomaterials. In addition, the increasing demand of nanotechnology motivates scientific research in this area. Decreasing fiber dimension size to the nanoscale has brought forth many advantages, such as increased surface area, high surface energy, and favorable mechanical properties. Even though nanofiber can be produced in many different ways, electrospinning is a versatile and simple method to fabricate continuous nanofiber by utilizing a high voltage power source. Electrospun carbon nanofibers (ECNFs) have many advantages over other carbon one dimensional (1-D) nanomaterials. In this chapter, background, manufacturing methods, and the current technologic status are reviewed.

1.1 Carbon Fibers

Carbon is a nonmetallic chemical element with the symbol "C" in the periodic table. The atomic number of carbon is 6, with a molar mass of 12.011 g/mol. Carbon can create bonds with other carbon atoms. This property induces it to create stable chemical products, such as chains and rings. There are various crystalline forms of carbon. These structures are named allotropes, and they include diamond, graphite, fullerenes and carbon nanotubes. Although all carbon allotropes consist of only carbon atoms, properties of each structure

are different due to atomic arrangement. For instance, diamond is the hardest natural material, and thus, is used as a high performance cutting tool, yet graphite is soft enough to be a pencil insert [1].

Carbon fiber (CF) consists of a molecule with 92% or more carbon atoms that are bonded, in crystals aligned parallel to the longitudinal axis of the fiber. Due to the alignment through the longitudinal direction, CFs are relatively stronger than other traditional materials of its size. The diameter of a single carbon filament is between 4 - 10 μ m. Depending on the application, CFs are manufactured as short, unidirectional, and woven. CFs are available on the market with strengths as high as 7.02 GPa, and elastic moduli as high 324 GPa [2]. The outstanding properties of CF are not only limited to superior mechanical properties, but also its low density (1.75-2.00 g/cm³) and high temperature resistance [3]. CFs are experiencing an increasing demand in the aerospace, automotive, and other industries where high-performance materials required due to these unique properties.

In modern industry CF has been introduced as a new material forty years ago. The first carbon 1-D material was successfully manufactured as an electric lamp filament by Thomas Alva Edison in 1877. This breakthrough invention is also considered the first CF. He tried more than 1600 materials to synthesis a carbon filament. Finally, Edison used cellulosic materials to fabricate the filament by dissolving cellulose in a solvent and molding into a thread or filament. These filaments were carbonized in a furnace in an oxygen free environment.

The carbon filaments manufactured by Edison were not sufficient enough to become structural material because of their poor mechanical properties. However, in the

1950s new precursors, such as rayon, were used to fabricate stronger CFs. In 1959, The National Carbon Company developed a carbon fabric which was generated from rayon cloth. These pioneer commercial cloths had 60 MPa tensile strength, with unwoven filaments strengths of 345-690 MPa, with a nominal filament diameter of 4.6 μm . In 1964, Union Carbide began providing high performance CF on the market with the commercial name Thornel 25. The material's ultimate tensile strength (UTS) was 1.25 GPa, with a Young's modulus 170 GPa [4]. By 1970, the company had introduced Thornel 100, with UTS of 3.95 GPa and tensile modulus of 690 GPa. Meanwhile in Japan, Industrial Research Institute in Osaka applied for a patent in 1959 for polyacrylonitrile (PAN) based CF. Young's modulus for this pioneer PAN based CF was as high as 170 GPa, while its maximum strength was 980 MPa [1]. Otani et al. developed a technique to manufacture pitch (petroleum product) based CF. The micro structure of the obtained fiber was very similar to other rayon and PAN based CFs [5].

Manufacturing of CF is a flexible process. The properties of the final product depend on process parameters, such as heat treatment conditions, stretching, surface treatment and precursors. Many different organic precursors can be employed to fabricate CFs. Rayon, pitch, and PAN are the most widely used precursor materials in the CF industry. In the late 1950s, cellulosic precursors were widely used to fabricate CFs. However, in time, cellulose based materials were replaced with more robust precursors. Today's CF industry is based on mostly pitch and PAN based CFs [6].

1.1.1 Pitch

Pitch consists of the combination of different polyaromatic molecules and heterocyclic compositions, depending on the source and pre-treatment approach.

Furthermore, carbon content of pitch can be as high as 80%. Pitch is a relatively low-cost material that can be obtained from many different sources. Pitch compounds are divided into 4 main groups:

1-) Saturates: The lowest molecular weight composition in the pitch

2-) Naphthene aromatic: Relatively low molecular weight aromatics and saturated ring configurations

3-) Polar aromatic: Relatively higher molecular weight and more heterocyclic

4-) Asphaltenes: The highest molecular weight portion in pitch with the highest aromaticity and most stable structure in terms of thermal stability [6]. Materials with higher ratio of asphaltene in the pitch are the most convenient for transforming CF.

Production of CFs requires several complex steps: fabricating fiber from the base material, stabilization of fibers, carbonization of stabilized fibers, and, finally, graphitization of CF at high temperature. Quality of final product depends on process parameters.

The melt spinning method is a common approach for manufacturing pitch-based precursor fibers. Figure 1.1 shows a schematic diagram of a common melt spinning process and process parameters. There are three steps to melt spinning: melting the pitch, extrusion through a specially designed spinhead, and drawing fibers in a cooling chamber.

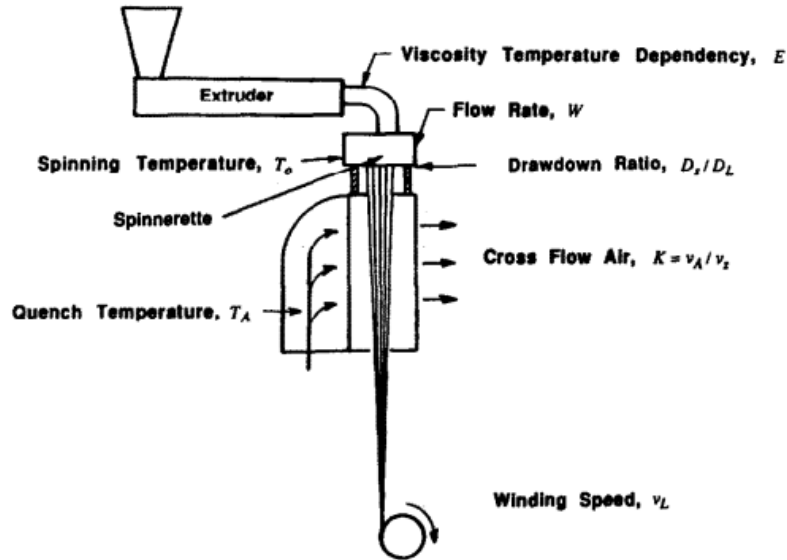


Figure 1.1 Schematic of the melt spinning process and variables [7].

Process parameters have significant roles on the structure and properties of CF. Spinner geometry, melting temperature, flow rate, drawdown ratio, cooling flow rate and temperature are important parameters to build an aligned graphite structure [7]. Every pitch composition has a unique melting temperature that is within a very narrow temperature range. 270-315°C is reported as spinnable for pitch precursors. However, a 15°C change can alter properties significantly [8]. Pitch fibers made below this temperature range yields poor mechanical properties due to brittle fractures. On the other hand, high temperature will increase viscosity and cause thermal degradation.

Stabilization is a necessary heat treatment prior to carbonization. This process occurs in air typically between 250-350°C. Duration may vary from 30 min to several hours. Stabilization can be performed up to 20 °C/min depending on composition of precursors [9]. Oxygen containing groups and development of hydrogen bonding among molecules create three-dimensional cross-linking.

After stabilization, carbonization is performed in an oxygen free environment at a high temperature range, typically 1500-1800°C. The most significant weight loss occurs in this stage. Most of the hydrogen, oxygen, nitrogen, and other elements are removed by imposing high temperatures. Subsequently, CFs can be graphitized at 2500-3000°C to improve their Young's modulus. Singer has reported that alignment of the crystalline lamellae is improved by raising the graphitization temperature [10].

1.1.2 Polyacrylonitrile (PAN)

PAN is a thermoplastic with a linear chemical formula $(C_3H_3N)_n$, containing a high carbon content (68% by weight) [11]. Figure 1.2 shows the chemical structure of PAN. The composition of PAN can be pure homopolymer or comonomers. The homopolymer PAN is not suitable as a precursor due to fast heat expansion during the first oxidation stage, and cannot be easily controlled. As a result, thermal shocks cause poor mechanical properties of CF. By introducing suitable comonomers, the exothermic reaction can be regulated. Additional benefits of comonomers include reduction initial cyclization temperature, improved mobility of the polymer chains that causes preferred orientation, and improved mechanical properties [12]. Nitrile groups make PAN a suitable precursor material due to strong dipole-dipole forces. As a result, PAN has a high melting temperature and solvent durability, except with highly ionizing solvents. Although dipole-dipole forces improve development of crystallinity during heat treatment, entropic and chemical shrinkage occurs. Shrinkage disintegrates the orientation of the fiber and reduce mechanical properties of CF [13]. Stretching during the stabilization process reduces the unfavorable effects of shrinkage and improves mechanical properties [14]. The manufacturing stages of PAN based CFs are shown in Figure 1.3 and are as follows: polymerization of PAN-

based precursors, spinning of fibers, thermal stabilization, carbonization, and graphitization.

Due to strong dipole-dipole bonding, PAN degrades before reaching its melting point. Traditional melt spinning is suitable for PAN precursor. Wet spinning is employed in CF manufacturing industry for PAN based CFs. This method is required for precursors that need to dissolve in a solvent. Fibers are extruded through a spinner that is submerged in a liquid bath, and are solidified in air. The stabilization step is significantly important to fabricate high quality CFs. Optimization of conditions, such as temperature, heating rate, and isothermal time, should be carefully designed depending on the fiber diameter and precursor properties. Generally, the temperature range is between 200-300°C. Subsequently, carbonization at 1500-1600°C in a nitrogen environment, and graphitization at up to 3000°C in an argon environment are performed. Surface treatment is a necessary step to prepare CF's surface for proper sizing. Carbonyl containing groups such as COOH increase bonding between the fiber and epoxy. Creation of carbonyl groups is performed by electrolysis of an acid or salt solution. After surface treatment, CFs should be washed with hot water to remove electrolysis. CFs are brittle materials and sizing also acts as a protector and lubricant. Additionally, sizing material should be selected such that it is compatible to resin [3].

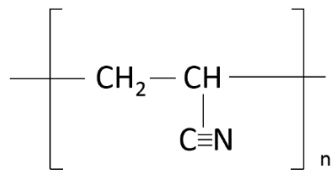


Figure 1.2 Chemical structure of PAN.

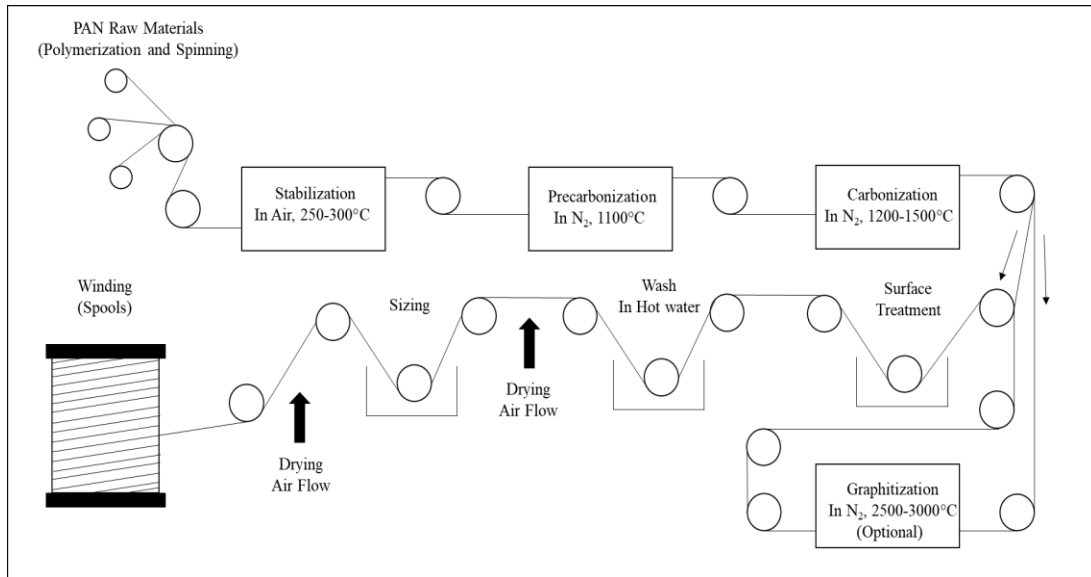


Figure 1.3 Schematic view of manufacturing steps of PAN-based CFs from precursor.

1.1.3 Current Status of Carbon Fibers and Limitation of Further Improvement

In the late 1950s, CFs were introduced commercially. The first generation of CFs were based on cellulosic precursors. Due to lack of knowledge and limitation of precursors, mechanical properties were not favorable. By employing pitch and PAN as precursors, the strength of CFs has been improved significantly. In approximately 20 years, the strength of a single CF has increased almost 10 folds. The Hexcel Corporation introduced PAN based CF, with the commercial name AS4, by the late 1970s. The tensile strength of AS4 was reported at 4.6 GPa. Today, the maximum tensile strength of a commercial CF is 7 GPa (Toray T1100GBC) [15]. CF is a significantly advanced material in terms of its mechanical properties and low density compared to other materials. However, there is still a great gap considering the theoretical strength of CFs is 180 GPa [16].

CF industry has been growing rapidly. The average cost of 1 kg CF was around \$30 in 2012. Today, a kg cost is almost half that price. The yearly demand of CF was 45,010

tonnes for 2012, but the estimated demand for 2020 is expected to be over 141,000 tonnes [17]. Many researchers have been working on the improvement of manufacturing steps, exploring new precursor, such as polystyrene, wood and copolymer modifications [18–21], and optimization of heat treatment processes [22–26], to improve the quality of CF and reduce its cost. There are several types of structural imperfections originated from precursor fibers that induce poor mechanical properties of CFs. Minimizing the structural imperfection is the most effective approach to improve mechanical strength of CFs. Size, distribution, and number of structural defects influence the strength directly. Structural defects in CFs are shown in Figure 1.4 , and can be classified as 1) surface defects like nicks, cracks, punctures, and diametrical bulges, 2) bulk defects like large cavities, small holes, endogenous pores, cracks)induced by internal stress, refractory inclusions, and other voids, and disordered structures, and 3) structural inhomogeneity such as sheath-core structures [16]. Inherently, wet spinning method leads to some disadvantages. Rapid solvent evaporation causes structural imperfection on precursor fibers, such as weak macromolecular orientation. Post stretching after spinning is a method used to improve molecular level alignment. It has been reported that hot stretching improves crystallinity of PAN precursors fiber [14]. Even though significant improvements have been made by optimizing spinning and heat treatment parameters, the maximum strength achieved so far is a small portion of theoretical value.

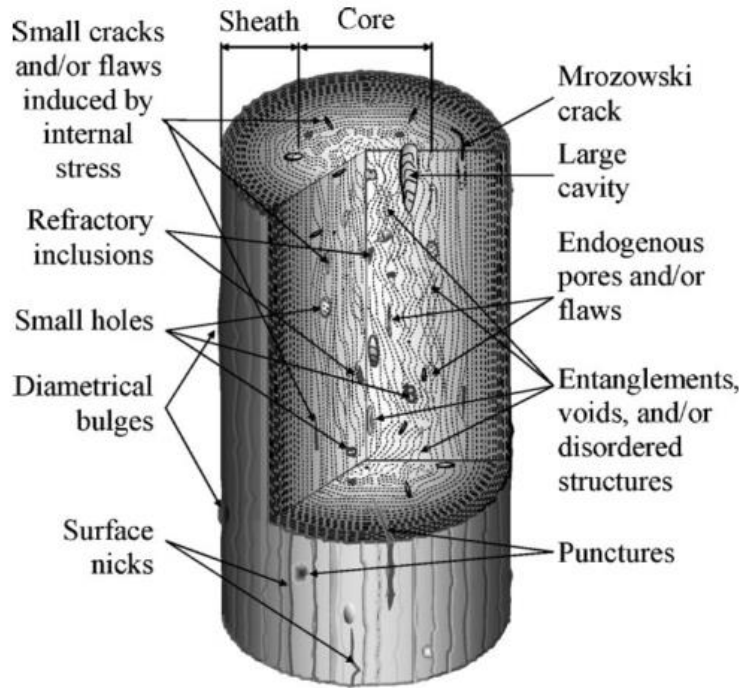


Figure 1.4 Schematic view of major types of structural imperfections in CFs [16].

Another well-known mechanism is decreasing the diameter of CF, leading to higher strength. This phenomenon is also known as size effect. Figure 1.5 shows the strength of PAN based CFs developed via different manufacturers, as a function of their diameter. For AS4, when the diameter reduces from 12 μm to 6 μm , the strength increases three times. There is an explorational trend between fiber diameter and tensile strength [27]. As a result, even a small reduction of fiber diameter will result in great strength increase. However, traditional spinning methods are limited to fabrication of precursor fibers with diameters less than 10 μm . 1D carbon based nanomaterials, such as carbon nanotubes (CNTs), vapor grown carbon nanofibers (VGCNFs), and ECNFs, can be manufactured with today's nanotechnology.

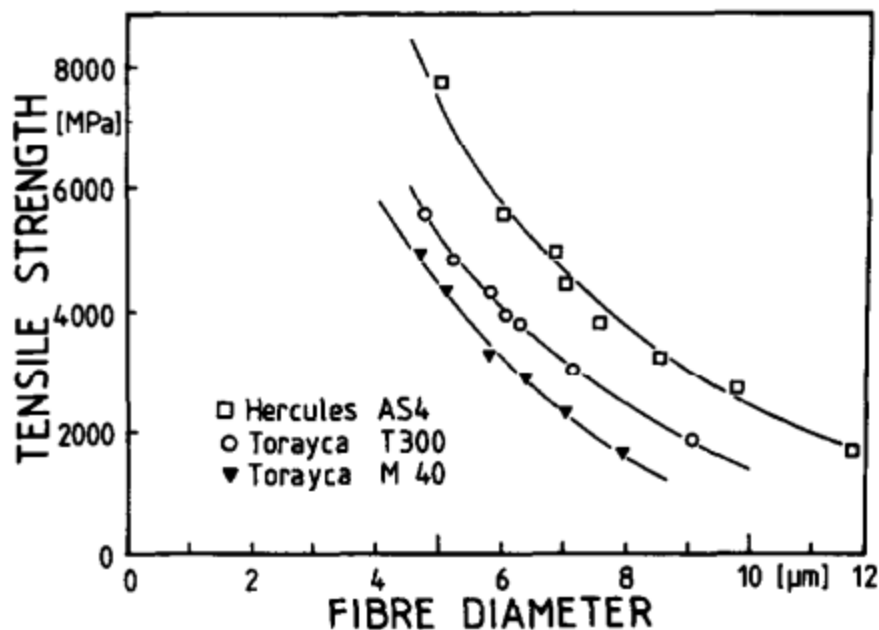


Figure 1.5 Tensile strength of CFs as a function diameter [27].

1.1.4 Vapor Grown Carbon Nanofibers (VGCFNs)

VGCFNs are classified as cylindrical graphene layers arranged into 1-D carbon nanostructures, with a wide diameter range, from a few tens of nanometers to several micrometers. As opposed to the conventional CF manufacturing approach, this method does not employ any precursor. This method is called catalytic chemical vapor deposition (CVD) and employs a metal catalyst, like iron, and a mixture of hydrocarbon gases and hydrogen. The typical vapor growth approach is schematically shown in Figure 1.6. Catalyst particles are exposed to hydrocarbon gases and hydrogen at high temperatures, around 1000°C. The particles will develop as long, cylindrical, hollow-cored filaments of somewhat graphitized carbon. The length of the filament can be several centimeters, with catalytic particles of less than 10 nm in diameter. The thickness and structure can be manipulated by the deposition of carbon from the vapor phase or increasing the temperature

of the hydrocarbon content [28]. Aspect ratios of resulting materials vary from 250 to 2000, with diameters of 50-200nm, and tensile strength and modulus of 2.92 GPa, and 240 GPa, respectively [29].

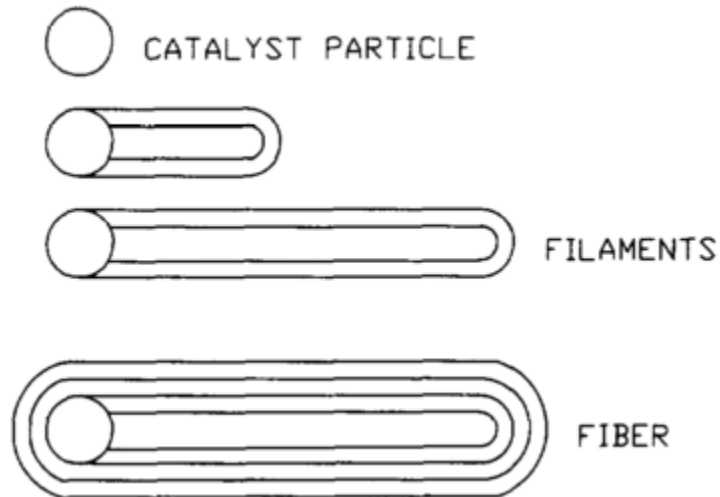


Figure 1.6 Schematic of growing filaments formed by catalytic particles [28].

1.1.5 Carbon Nanotubes (CNTs)

Since their discovery in 1991 by Iijima CNTs receive a great deal of attention due to their unique structure, superior mechanical, thermal and electronic properties [30]. CNTs are the strongest materials, with extremely high tensile strength (100 GPa) and elastic modulus (1 TPa) [31]. CNTs are divided into two main groups depending on the number of its layers, or walls. Single-walled CNTs (SWNTs) are formed of only one rolled-up layer of graphite with, a diameter up to 1.5 nm. The other groups of CNTs are called multi-walled CNTs (MWNTs), consisting of multiple interlinked graphite tubes with, a diameter up to 100 nm (Figure 1.7) [32]. There are a multiple fabrication methods of CNTs, including arc-discharge [30], laser ablation [33], and CVD from hydrocarbons [34].

Aluminum oxide, porous silicon, quartz glass, and silicon crystals are commonly used as substrates [35].

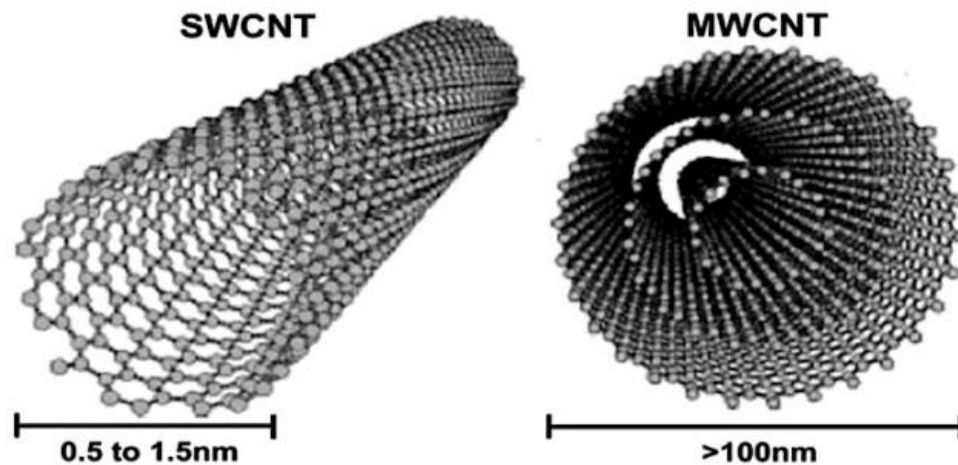


Figure 1.7 Schematic view of SWCNT and MWCNT [32].

Although CNTs are promising materials due to their unique mechanical, electrical, and thermal properties, there are many obstacles to their use in applications. Separating CNTs from substances without altering or damaging the CNTs is one of the biggest concerns in terms of purification. The challenge is to find how to separate the single-walled carbon nanotubes from those substances without changing or damaging the carbon nanotubes. Amorphous carbon, metal catalyst and fullerenes must be cleaned from the soot due to their possible influence on the CNT's properties if included [36]. CNTs inherently stick together in bundles due to their high surface energy. Dispersing CNTs homogeneously within a matrix material is a significant problem facing their use. Ultrasonic dispersion,

high shear mixing and melt spinning approaches are commonly used to improve dispersion. Although all of these methods improve dispersion, none provides a complete solution [36, 37]. On the other hand, electrospun carbon nanofibers (ECNFs) are continuous, do not require complex purification, and can be fabricated already aligned.

1.2 Electrospinning

1.2.1 History of Electrospinning

Electrospinning has a long history that dates back to the discovery of electrostatic attraction of a liquid, discovered by English scientist William Gilbert in 1600 [38]. He observed a cone formation on a droplet of water when an electrically charged rubber stick was brought close to the droplet. In 1900, John Francis Cooley filed a patent with the first visual demonstration of electrospinning [39]. In 1914, John Zeleny studied relations between electrical discharge from liquid points and electric intensity at their surfaces. He published a paper on the characteristic of fluid droplets at the end of metal capillaries [40]. Electrospun fibers were used as filter materials, known as “Petryanov filters”, for the first time in 1938, [38]. In the 1960s, Sir Geoffrey Ingram Taylor developed a significantly important theoretical model about the conic shape formed from a fluid droplet under electric field [41–43]. This shape was named “Taylor Cone.” In 1963, Simons patented an apparatus for the production of patterned non-woven fabrics using electrical spinning [44]. The system consists of a positive electrode attached to a polymer solution, and a negative cylindrical electrode where fibers are deposited. The term electrospinning was first used by Doshi and Reneker in 1995 [45]. Their study showed that many organic polymers could be spun by electrospinning, causing an exponential increase of publication in this area by the research community (Figure 1.8). Many polymers that dissolved in

solvent can be electrospun, as well as some inorganic solvents, such as Al_2O_3 , Fe_2O_3 , ZrO_2 , BaTiO_3 , Al_2O_3 , Fe_2O_3 , ZrO_2 , BaTiO_3 , and NiFe_2O_4 [46]. Even though electrospinning is a promising method and important to fabricate continuous nanofibers, there are many mechanisms still not well understood.

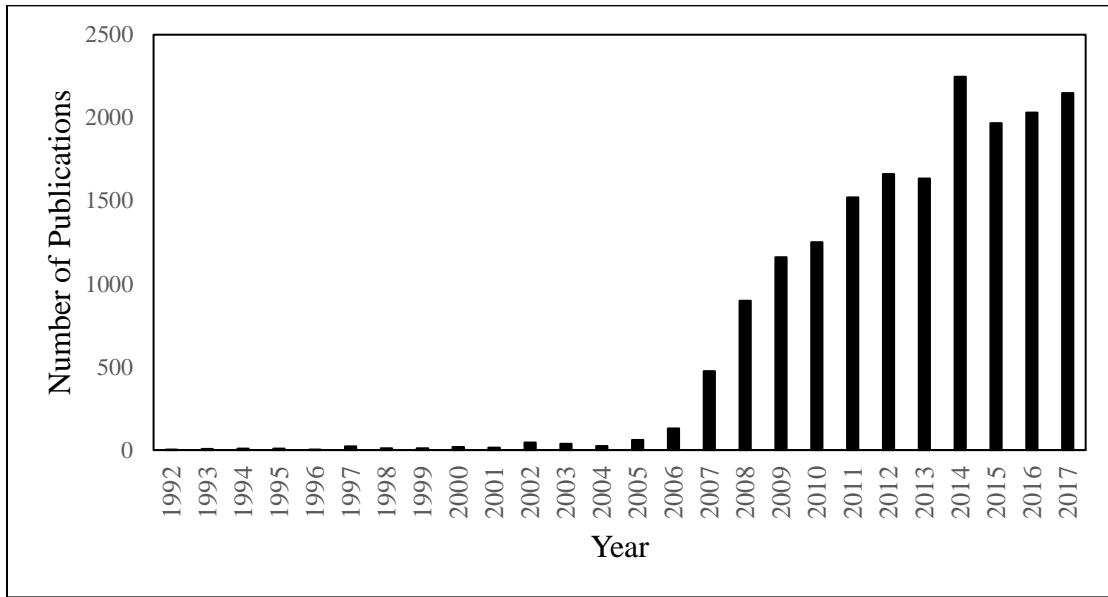


Figure 1.8 Number of scientific articles published about electrospinning (Source: Compendex, keyword: electrospinnig).

1.2.2 Fundamental Theory

Conventional spinning methods, such as dry spinning, melt spinning, and wet spinning employ a mechanical force to decrease fiber diameter. On the other hand, electrospinning utilizes a high electrical potential difference to create a mechanical force that reduces fiber diameter to the nanoscale [47, 48]. Figure 1.9 shows a schematic view of a typical electrospinning setup consisting of three main components: a high voltage power supply, a syringe pump, and a grounded target. Employing a high electrical voltage provides a positive charge to the droplet. An electrostatic repulsive force is generated

between the bordering entities on the droplet. When the electrical force is higher than the required force to overcome the surface tension of the droplet, a jet forms from the Taylor cone [42]. The jet experiences a series of bending loops and whipping, yielding an excessive stretching and creation of nanofibers. Each loop grows larger in diameter as the jet grows longer and thinner. The cycles of bending instability continue until the solvent evaporates, and the remaining is a solid nanofiber [49]. The collector can be designed to produce a desired nanofiber arrangement, such as nonwoven mats, random mats or aligned yarn. Figure 1.9 shows a disc collector to deposit aligned nanofibers.

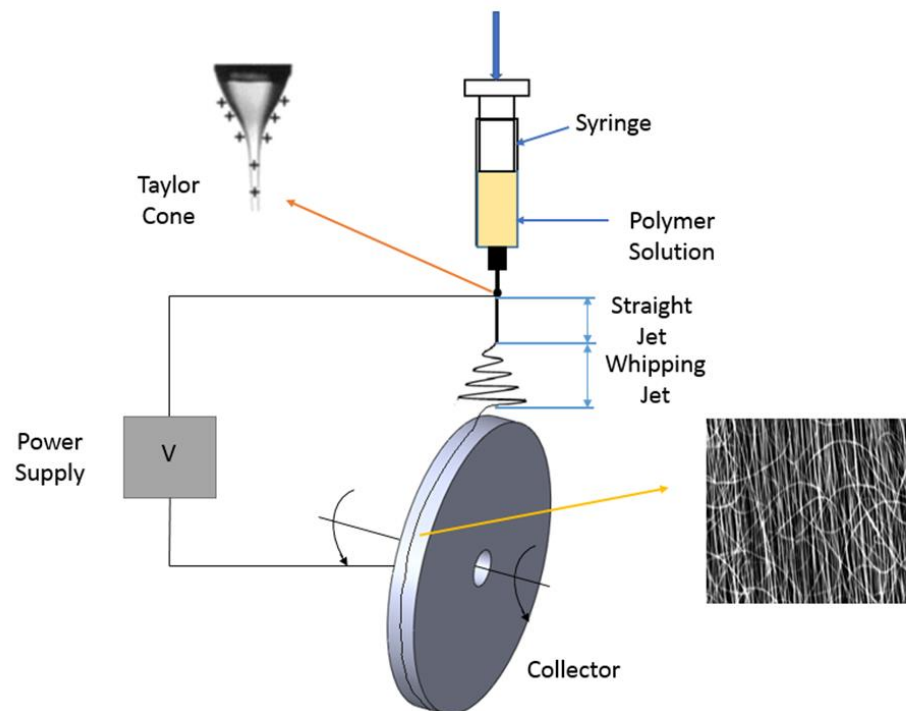


Figure 1.9 A schematic representation of electrospinning consisting of a syringe and pump, high voltage source and grounded collector.

1.2.3 Applications of Electrospun Nanofibers

Electrospinning has been found to be the most effective way to manufacture continuous nanofibers by using a polymer solution (solvent and polymer) due to simplicity of the depositing process [50]. Thus, this approach is attractive for a broad variety of applications. The listed applications below are a few examples of electrospun nanofiber applications.

- Hybrid composites: Reinforcement against interleave [51], delamination [52], fracture and fatigue [53].
- Biomedical: tissue engineering [54, 55], wound dressing [56–58], artificial blood vessels [59, 60], drug delivery [54, 57, 61].
- Filtration [62, 63].
- Energy harvest and storage: Fuel cells [62, 64, 65], batteries [66–68], supercapacitors [65, 69, 70], solar cells [62, 71], hydrogen storage [64, 72].
- Electronic: Sensors [64, 73], transistor [74].

1.2.4 Electrospun Carbon Nanofibers (ECNFs) and Fabrication

ECNFs can be manufactured aligned and continuous, unlike VGCNFs and CNTs. Electrospinning is also a significantly cost-effective method of producing carbon nanofibers compared to other available techniques. Figure 1.10 shows scanning electron microscope (SEM) images of VGCNFs, CNTs and ECNFs showing superior alignment and assembly.

ECNFs have high potential in many applications such as hybrid composites, energy storage, sensors, and tissue engineering due to their small dimension, excellent physicochemical and mechanical properties, and relatively low production cost.

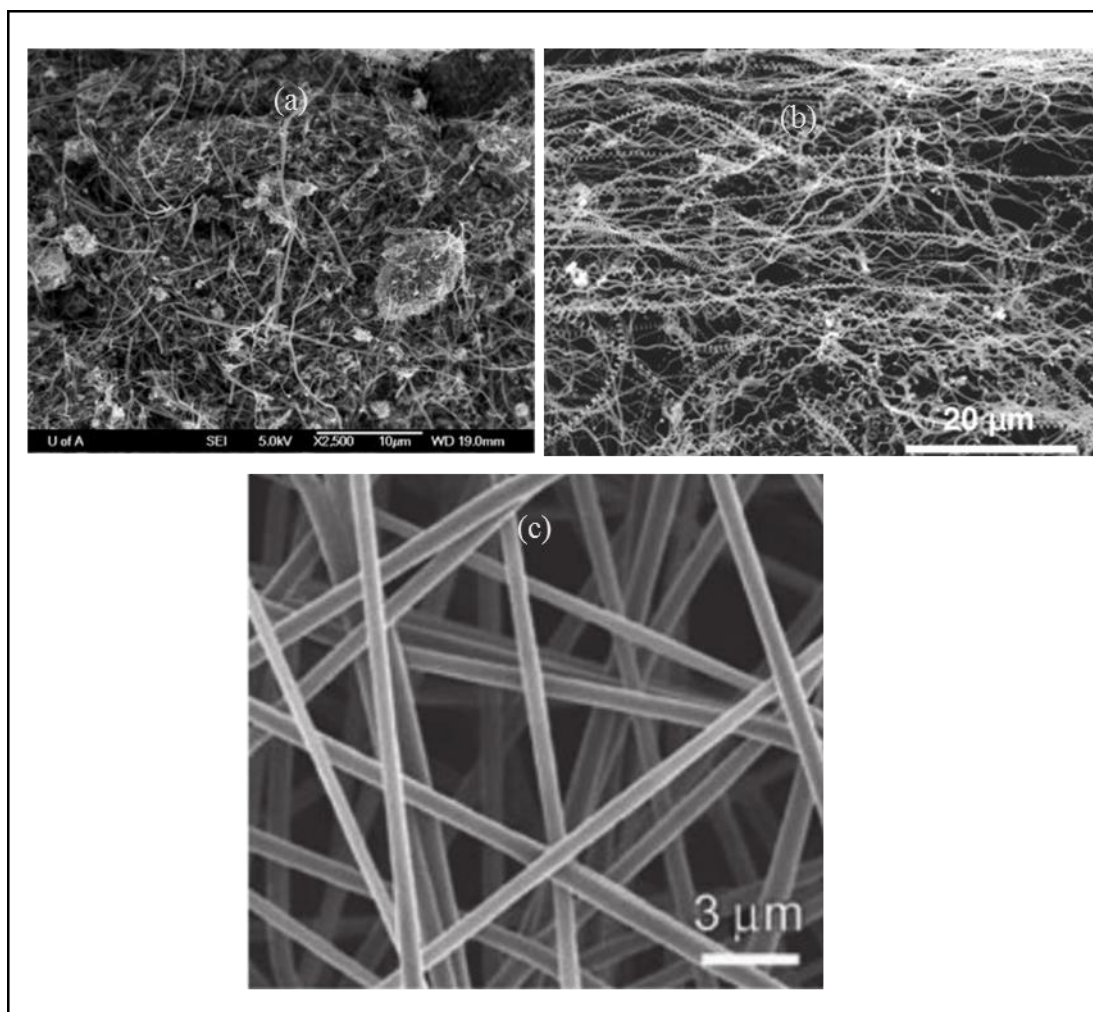


Figure 1.10 SEM images of (a) VGCNF [75] (b) helically coiled CNTs [76] (c) ECNFs [77].

PAN is the most convenient precursors to produce high performance CFs when compared to other precursor (such as pitch, rayon etc.) due to its higher melting point, carbon content and faster rate in pyrolysis [78]. PAN is also the most widely used precursor polymer for fabrication of carbon nanofibers via electrospinning. ECNFs are produced

from electrospun PAN nanofibers by a sequential series of heat treatment steps in different inert gases and temperatures [77].

1.2.5 Post Electrospinning Stretching and Heat Treatment

Heat treatment and stretching are similarly performed to convert the electrospun fibers into ECNFs. There are two main heat treatments necessary to generate ECNFs successfully, stabilization and carbonization. Graphitization can be performed at higher temperatures to increase the resulting fiber's elastic modulus. Stretching of PAN fibers is an optional process that increases molecular level orientation. This results in the improvement of mechanical properties of carbon fibers [79]. The precursor fiber is drawn prior to stabilization below the glass transition temperature ($\sim 135^{\circ}\text{C}$) while it is still a thermoplastic polymer, to improve the molecular orientation [14].

The stabilization stage is a relatively low temperature treatment, compared to carbonization and graphitization. Stabilization is typically performed at a temperature range around $200\text{-}400^{\circ}\text{C}$, in an oxidative environment (mostly air). A ladder structure is formed during stabilization to induce fibers to withstand higher temperature and improve carbon yield.

Carbonization is the stage that noncarbon contents are removed and carbon fibers are generated. The environment must be oxygen free; typically nitrogen is selected as the inert gas atmosphere. The process is conducted at temperatures ranging from 1000°C to 2500°C . During carbonization, a thermally stable pyridinic structure forms, and subsequently converts into a turbostratic stacked ring structure.

The graphitization is completed at temperatures higher than 2500°C . At this high temperature, heat treatment does not cause weight change in the fiber but improves the

orientation of the crystallites in the direction of the fiber axis. As result, the modulus of the carbon fiber increases.

1.3 Scope of the Work

ECNGs have promising properties, such as high surface area, excellent physicochemical and mechanical properties, and relatively low operational cost. However, there is no available reinforcement application of ECNFs yet due to its low mechanical properties when compared to CFs, and disorientation of fibers inherent of electrospinning itself. Fiber alignment is a key parameter for fiber's unidirectional reinforcement. Furthermore, mechanical properties of ECNFs are highly dependent on the molecular level orientation of electrospun fibers and stabilization conditions. This dissertation focuses on improvement of electrospun fiber orientation, fabrication of high quality nanofibers, understanding the stretching effects and pre-loading mechanism during stabilization.

In chapter 2, the electrospinning fabrication process parameters are continued, and high-quality nanofibers will be introduced through a literature review. A new versatile solid electrospinning design to fabricate highly aligned nanofibers will be mentioned. The effect of relative humidity (RH) on fiber diameter and mechanical properties of electrospun, stabilized fiber and ECNFs will be investigated. In chapter 3, the effects of different collector types on nanofiber properties and orientation will be studied. Chapter 4 will focus on how electrode design influences nanofiber orientation, diameter, mechanical properties and Taylor Cone jet formation. In chapter 5, different stretching ratios and pre-loading conditions of stabilization will be investigated. In chapter 6, a statistical model will be introduced to estimate single filament tensile properties of ECNFs from a bundle test.

Chapter 2 : ELECTROSPINNING DESIGN and PROCESS PARAMETERS

2.1 Introduction

Although the electrospinning process is simple, its design influences the quality of the resulting nanofibers and fiber structure. Environmental conditions significantly affect electrospinning. Hence, a controlled chamber is necessary for isolation to maintain ambient conditions and prevent adverse conditions from effecting electric field. The collector design influences fiber structure and fiber properties, such as fiber diameter, tensile strength, etc. The collector is one of the most important elements of the system influencing fiber quality.

In this chapter, different collector designs are reviewed to determine a new design electrospinning setup for further research. Process parameters are reviewed and determined to generate continuous nanofibers, relative humidity (RH) effects on diameter, and tensile properties of eletrospun, stabilized and carbonized nanofibers.

2.2 Collector Design Review

Many modifications on electrospinning collector designs have been made specifically aimed at improving and controlling nanofiber orientation. Employing a rotating disk collector and manipulating an electric field are two main concepts to fabricate aligned nanofibers. Karatay et al. [80] employed two auxiliary parallel electrodes (Figure 2.1 a) connected to function generators and amplifiers to minimize wiping motion. The auxiliary electrodes reduced the bending instabilities of the jet. Acharya et al. [81]

achieved an improvement on fiber alignment by applying a secondary electric field (Figure 2.1 b) perpendicular to fluid jet. Song et al. [82] modified the parallel electrode method by adding a positively charged ring to the parallel electrode collectors (Figure 2.1 c). They reported that the additional ring improves fiber alignment and mechanical properties compared to the traditional single electrode method. Operating two strips separated (Figure 2.1 d) by a gap creates a parallel array fiber along the perpendicular collectors. The insulated gap results in modification on the electric force configuration [46]. Figure 2.1 e shows the electrostatic forces in the opposite directions that results in fibers that are stretched across the gap and aligned. Although manipulating electric fields by using additional electrodes, secondary electric field, or parallel collectors improves alignment, these approaches are limited in terms of fabrication scale. Employing additional electrodes or electric fields requires an extra electric source or complicated control units. Furthermore, fiber length is short due to limitation of electrode geometries.

Table 2.1 summarizes a few common examples of collectors along with their advantages and disadvantages. Rotating collector equipped electrospinning setups are often used due to their flexibility and high production rate. However, each approach has its advantages and disadvantages. The metal disc collector is the simplest one to generate uniaxially aligned nanofiber yarns. In order to utilize the maximum benefits of these methods, some innovative modifications are required. The new system should be stable at high revolutions per minute (rpm) and versatile. The design is required to withstand high rpms. Additionally, all elements of the system, except the collector, should be electrically isolated and disconnected from the ground to allow for deposition of fibers the collector

only. Otherwise, fibers will be deposited on all the metal elements connected to the ground. A new collector design that fulfills these requirements will be introduced in section 2.3.

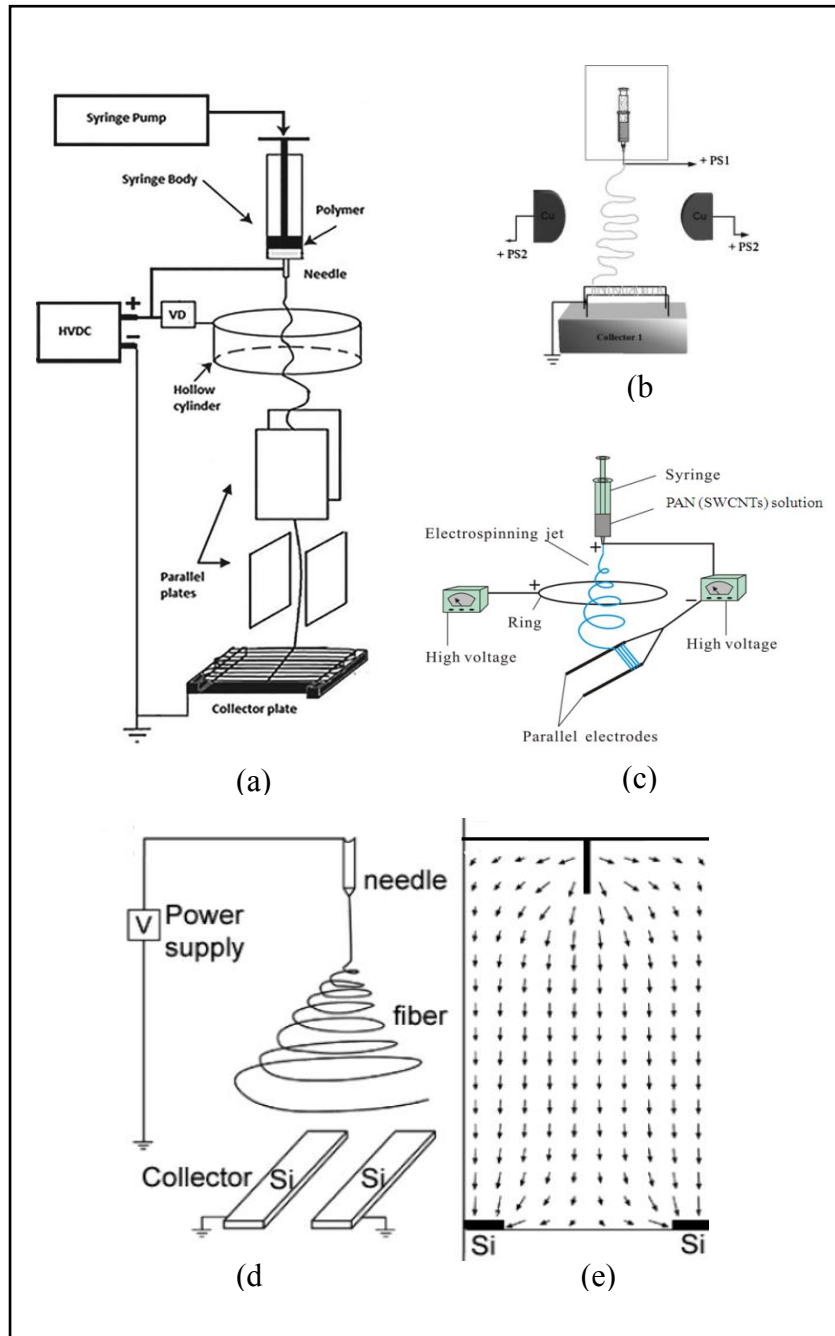

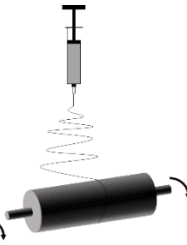
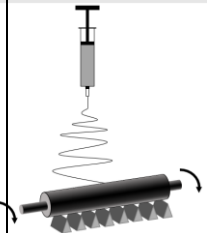
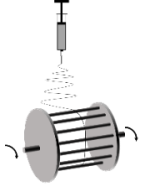



Figure 2.1 Typical electric field manipulating approaches of electrospinning systems: (a) Auxiliary parallel plates [80]. (b) Secondary electric field [81]. (c) Modified parallel electrode [82]. (d) Parallel auxiliary electrode arrangement. (e) Electric field profile from spinneret to the parallel electrodes [46].

Table 2.1 Schematic of common type rotating collector equipped electrospinning setups with and their advantages and disadvantages.

Collector	Schematic	Advantage	Disadvantage
Metal disc		<ul style="list-style-type: none"> Highly aligned fibers are possible 	<ul style="list-style-type: none"> Small area of fiber alignment [83]
Rotating drum		<ul style="list-style-type: none"> Capability of aligned large fiber area [84] Simple 	<ul style="list-style-type: none"> Fiber breakage at high rotating speed [85] High aligned assemblies are difficult to generate [86]
Rotating tube collector with knife-edge electrodes below		<ul style="list-style-type: none"> Aligned fibers cover entire tube 	<ul style="list-style-type: none"> The system requires negative electrode [87]
Rotating wire drum		<ul style="list-style-type: none"> Highly aligned fibers can be deposited 	<ul style="list-style-type: none"> Alignment may not be consistent along the collector [88]
Metal disc with sharp edge		<ul style="list-style-type: none"> Highly aligned fibers possible at lower rpm 	<ul style="list-style-type: none"> The depositing area is limited [89]

2.3 Electrospinning Setup Design

The most critical part of the design is the rotating collector. The design must withstand high speeds to produce aligned fiber successfully. Additionally, all the elements inside the chamber should be non-conductive. The shaft is the component that is exposed to the most mechanical deflection. Elastic shaft materials may cause wobbling that effects fiber arrangement. A rigid core-shell structure shaft is considered to eliminate this problem. Figure 2.2 shows the shaft structure and dimensions. Core material is chosen to be an aerospace grade aluminum 7075 series tube (inner diameter (ID) of 20 mm, outer diameter (OD) of 25 mm, and length of 304 mm) due to its light weight and high strength. The aluminum tube is covered with a tightly fit polyvinyl chloride (PVC) tube (ID 25 mm, OD 32 mm, and length 228 mm) to provide electrical insulation. As seen in the Figure 2.3, the shaft is supported with two ball bearing that are capable withstanding high rpm and isolated outside of the chamber. Two adjustable parallel acrylic discs, with a diameter of 20 cm and wall thickness of 0.5 inches, are used to operate different sized collectors, between 12 mm and 100 mm in width. Depending on the collector width, the disc can be move sideways on the shaft. The collector is supported with 16 individuals 0.25 inch in diameter rods. The chamber is made with see-through acrylic to allow for monitoring of the electrospinning process and isolate the setup. A grounded copper wire is connected to the collector and passes through the shaft. An rpm controlled electric motor was used to adjust the rpm of the disc. A belt drive system is used to minimize vibration. A high voltage DC power supply (1kV-19kV) is employed. The wiring is carefully laid out to avoid any unwanted electric field development that may disturb the electric field between the collector and needle tip. A photograph of the electrospinning setup is shown in Figure 2.4.

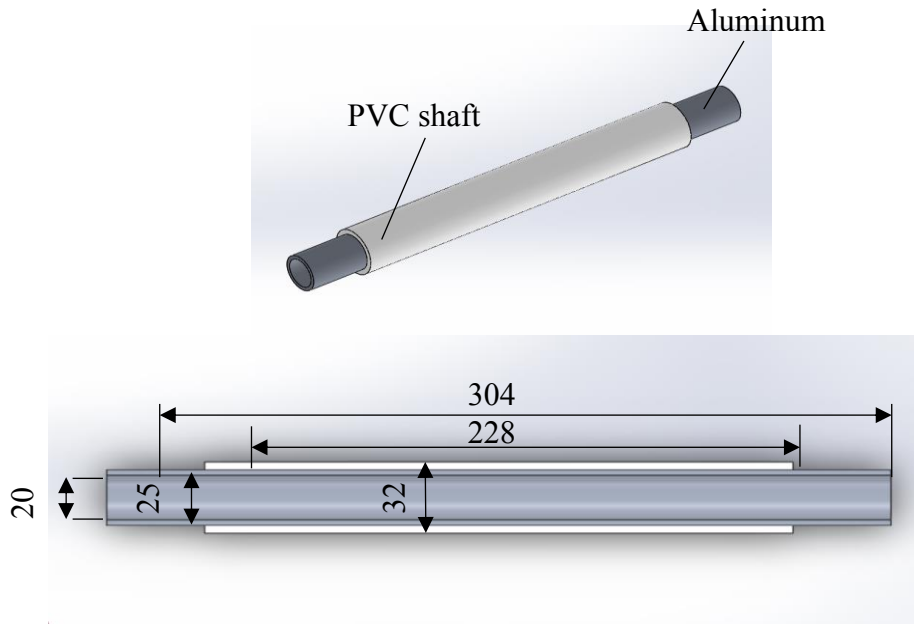


Figure 2.2 3D model of the shaft design with dimensions in mm.

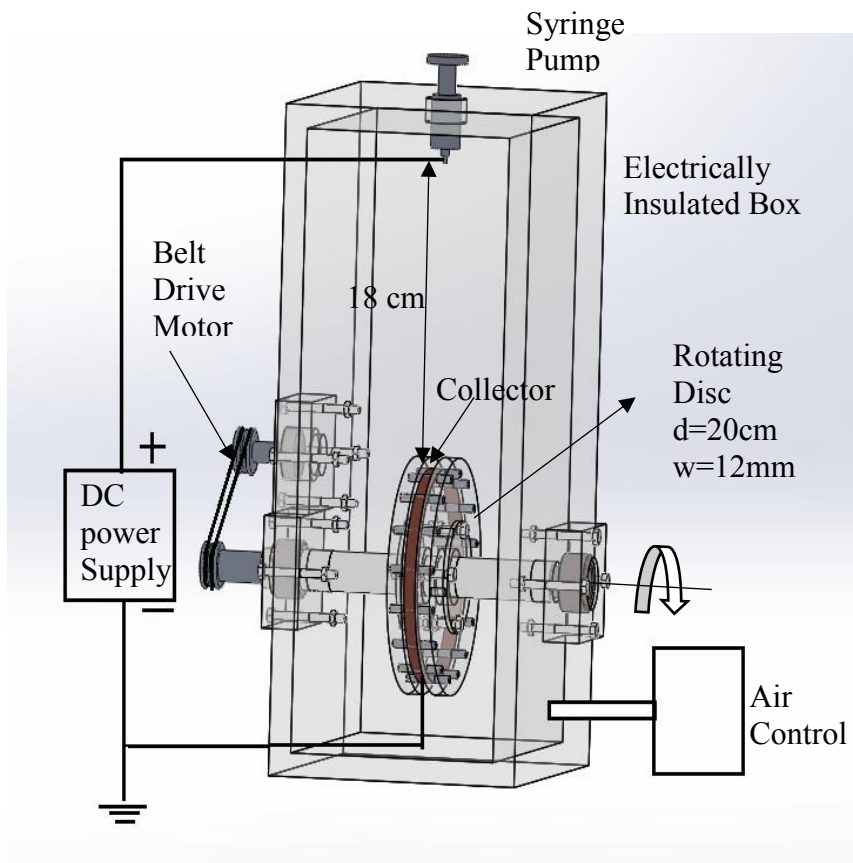


Figure 2.3 Schematic view of the electrospinning setup.

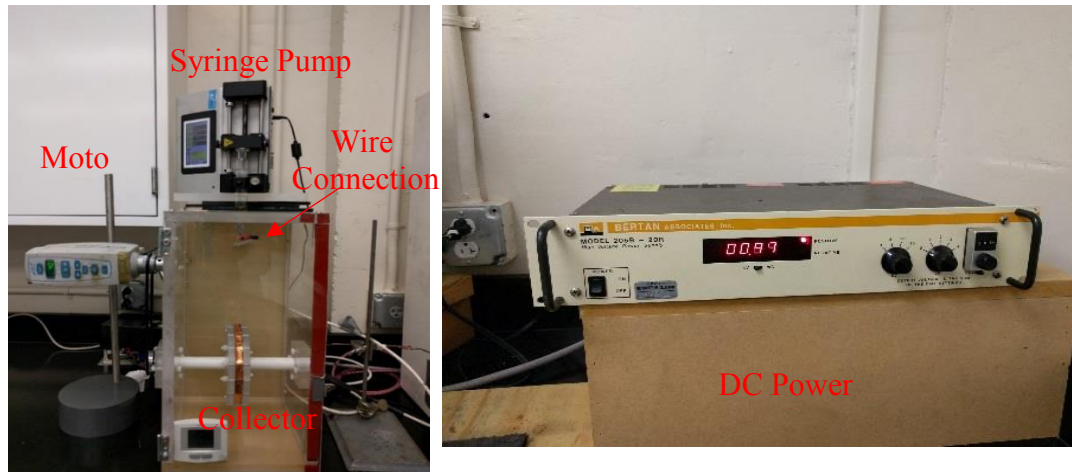


Figure 2.4 Actual photography of the electrospinning setup and components.

A homemade air control system is employed to control RH during electrospinning by purging depending on the desired RH. If the RH is lower than desired RH level, air is circulated with more humid air. If the RH is too high, compressed air is introduced.

2.4 Process Parameters

Electrospinning is known as a simple method that does not require complicated components. However, the process is complex itself due to the number of parameters that effect morphology, fiber diameter, and structural properties. The process parameters are commonly divided into three main groups: solution, operational parameters, and ambient conditions. All these governing parameters influence fiber properties directly. Understanding the mechanism of these parameters is important to fabricate bead free and uniform nanofibers.

2.4.1 Solution Parameters

Approximately 100 different polymers have been electrospun successfully [90]. The spin-ability has been investigated by studying the effect of molecular weight, solution

concentration, viscosity, surface tension, and the solution's electric conductivity. The molecular weight of the polymer is critical in terms of spin ability. Attempting to electrospin low molecular weight solutions results in poor properties such as bead formation. It has been reported that spinning less than 10,000 g/mol polymers causes bead formation [91, 92].

Polymer concentration has an important role on fiber diameter and morphology. Low concentration results in bead formation and droplets [93]. Lee et al. reported that a Polystyrene (PS) solution less than 15 wt% causes bead formation [94]. Figure 2.5 shows the SEM image of two different concentrations that are used to electrospin Poly(butylene succinate) (PBS). Increasing polymer concentration from 14 wt% to 17 wt% results in bead free nanofibers [95]. Furthermore, fiber diameter can be controlled by manipulating solution concentration. Electrospun fibers generated from higher concentration result in larger diameter [92, 96–98]. The number of entanglements between polymer chains is directly related to the concentration of the solvent. An increase in the number of entanglements causes larger diameters due to inhibited jet stretching under electric field.

To create a repulsive force, the polymer solution must be charged sufficient enough to trigger jet formation. The solution's ability of charge carriage is influenced by conductivity. Additionally, subsequent stretching is influenced by increasing conductivity. Solutions with low conductivity result in insufficient elongation, and often lead to bead formation [99]. The addition of salt into solvent increases the conductivity. This method is widely used to increase the conductivity of solvents [100, 101].

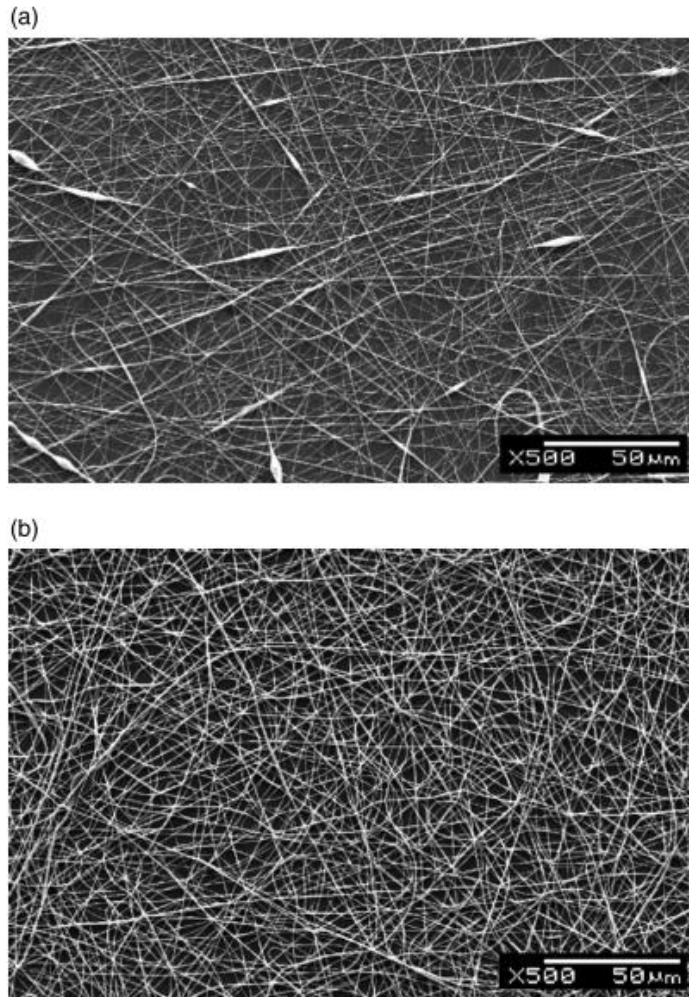


Figure 2.5 SEM images of PBS electrospun nanofibers. The concentration (a) 14 wt% (b) 17 wt% [95].

2.4.2 Governing Parameters

Applied voltage and flow rates are two related governing parameters. Applied voltage should be adjusted to flow rate in order to spin uniform and continuous nanofibers [102]. Although researchers have an agreement about effects of solution properties, flow rate effects on fiber diameter are inconsistent. Bakar et al. reported that when flow rate increases, average diameter of PAN nanofibers decrease [103]. On the other hand, Liu et

al found that average fiber diameter rises with increase on flow rate. Average diameters of 369 nm are obtained for Ethylene-propylenediene (EPDM) electrospun nanofiber with a flow rate is 0.5 ml/h. Average diameter increases approximately twice when the flow rate increased to 2 ml/h. Additionally, standard deviation increases from 15 nm to 53 nm [104].

Fiber diameter of electrospun nanofibers are influenced with applied voltage. Bisphenol-A polysulfone (PSF) electrospun nanofibers diameter showed a slight decrease from 344 nm to 323 nm when voltage was raised from 10 to 20 kV [105]. Additionally, it has been shown that the standard deviation was lower when the nanofiber diameter reached smaller value. Barua and Saha [48] investigated the relationship between flow rate and applied voltage. They reported optimum conditions for continuous flow jet, investigated applied voltage, and flow rate effects on fiber diameter for 10 wt% PAN in N,N-dimethylformamide (DMF). A favorable flow rate range is obtained as a function of applied voltage (Figure 2.6).

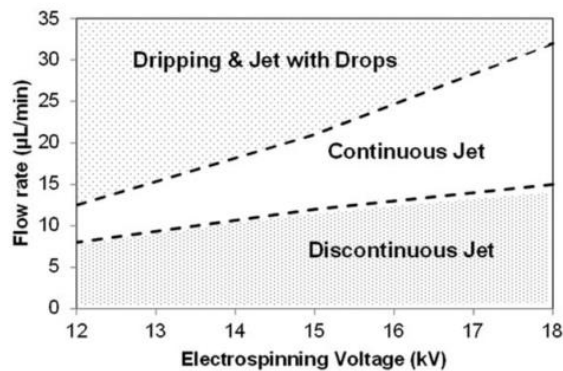


Figure 2.6 Favorable flow rate range for continuous flow jet as a function of applied voltage for 10 wt% PAN in DMF [48].

The gap between and capillary tip are required for solvent evaporation. Although it has been reported that the gap does not influence fiber diameter significantly, the distance must be sufficient to lead nanofiber formation [105, 106].

2.4.3. Ambient Parameters

Electrospinning is sensitive to environmental conditions, such as RH and temperature. Depending on the chemical composition of the solvent, RH may have different effects for water-based solvents. Tripatanasuwan et al. [107] investigated the effects of RH on poly(ethylene oxide) (PEO) aqueous solution. Fiber diameter decreases when the RH humidity increases due to higher vapor concentration, leading to reduction in evaporation and solidification. On the other hand, the average diameter of electrospun nanofibers fabricated from a cellulose acetate (CA)/ Dimethylacetamide (DMAc) solution increased by increasing RH [108]. Barua and Saha investigated RH effects on PAN 10 wt% in DMF electrospun nanofibers. Similarly, higher fiber diameter is observed for higher RH [109].

Morphology is another property that is influenced by relative humidity. The number of pores and average pore size increases as RH is increased [109–111].

The evaporation rate of the solvent and viscosity is highly dependent on ambient temperature. Vrieze et al. [108] investigated the temperature effect on cellulose acetate (CA) and poly(vinylpyrrolidone) (PVP) electrospun fibers. It has been reported that average fiber diameter is reduced when the temperature is increased to 30 °C from 20 °C.

2.5 Relative Humidity Effects on Fiber Properties

RH has been shown to affect the diameter and morphology of the fibers. Its effects on the diameter of fiber depends on the type of solution and composition. Mechanical properties are also influenced by environmental conditions. Electrospun PAN nanofibers fabricated at high RH (40% and 60%) show low mechanical properties compared to produced nanofiber at 22% RH [109].

RH effects on stabilized and carbonized PAN based electrospun nanofibers have not been investigated, even though RH mechanism is reported. Effect of relative RH on morphology, fiber diameter distribution and tensile properties of the as-spun, stabilized and carbonized nanofibers are reported in this section.

2.5.1 Experimental

2.5.1.1 Materials and Processing

PAN with an average molecular weight of about 150,000 g/mol was obtained from Sigma-Aldrich. DMF was used as the solvent and was purchased from Sigma-Aldrich. PAN was dissolved in DMF at 80°C by stirring continuously at 500 rpm 5 hours. Air bubbles appeared in the solution during mixing, but all bubbles are removed before electrospinning.

10% PAN in DMF (by weight) solution was electrospun inside a closed chamber. The spinning solution was held in a vertical syringe with a stainless-steel needle electrically connected to a DC power supply. The distance between the tip of the needle and the surface of the disk was constant at 18 cm. Barua and Saha reported [48] optimum flow rate and electrical charge for continuous and stable flow jet, with an electrospinning voltage of 15 kV and flow rate of 15 μ l/min. In this experimental setup we also adopted the same conditions to achieve a stable jet during the electrospinning process, which lead to improved mechanical properties of as-spun fiber yarns. The RH was controlled by controlling moist to dry air in chamber, adjusting the air flow rate with respect to the desired RH. Once the system reached to the desired RH level, electrospinning was performed while the disc was rotating at 600 rpm. The RH level was monitored to ensure humidity $\pm 2\%$ the desired during the electrospinning. If the variation in RH level was

higher than the $\pm 2\%$ tolerance limit, the yarn was discarded, and a new yarn was made. There were three different RH levels; 22%, 40% and 60%. The temperature was maintained as 20°C. As-spun nanofiber bundles were peeled off the copper foil in the form of a yarn, mounted on a drying rack to keep them in tension, and dried at 60°C for 12 h under vacuum.

After the drying process, the electrospun yarn was fixed on a stainless steel plate by gluing from both ends using ceramic glue. A programmable air convection oven (Model 825, Cole-Parmer) was employed for stabilization. The plate was heated in the oven with a 5 °C/min ramp from room temperature to 260°C for 180 min. Barua and Saha [112] reported that the optimum stabilization time at 260 °C is 180 min.

2.5.1.2 Characterizations

2.5.2. Results

Figure 2.7 shows a few typical SEM images of as-spun nanofibers produced at different humidity conditions. Nanofibers at this low magnification seem uniform and defect free, but careful observation of Figure 2. 7c indicates a few traces of bead formation. Nanofibers also seem mostly aligned along the rotational axis of the drum at 600 rpm. About 100 measurements of individual fibers diameter were also measured from the SEM images taken at different locations of the nanofiber tows, and plotted to show statistical diameter distribution. As seen in Figure 2.7, the average fiber diameter increases with increasing RH. The diameter distribution seems more widespread at 40% and 60% RH compared to 22% RH. Table 2.2 summarizes average fiber diameter and standard deviation of all as-spun, stabilized and carbonized nanofibers for different RH conditions. All nanofibers experience shrinkage during the heat treatment cycles. The highest shrinkage is about 13% during stabilization and about 39% during carbonization, at 22% RH conditions.

The amount of shrinkage is lower at higher RH conditions. This could be due to surface roughness seen on the fiber surface at higher humidity conditions as discuss below.

As the fiber surface cools rapidly due to solvent evaporation, water molecules accumulate on the surface, particularly at higher humidity conditions. The accumulated water molecules leave behind porous structures during evaporation (Figure 2.7) [109, 111]. Another mechanism for porous structure could be due to thermal phase separation during solvent evaporation [110]. It is believed that at higher humidity conditions the formation of porous structure of the fiber surface is related to solvent evaporation, process temperature, and thermal phase separation.

Typical tensile stress vs strain curves of as-spun nanofiber yarns produced at different relative humidity are shown in Figure 2.9. It should be noted that the cross-sectional areas of the nanofiber samples were calculated based on the theoretical equations discussed before. As seen in Figure 2.7, nanofiber yarns produced at 22%RH exhibit the highest tensile strength and strain to failure.

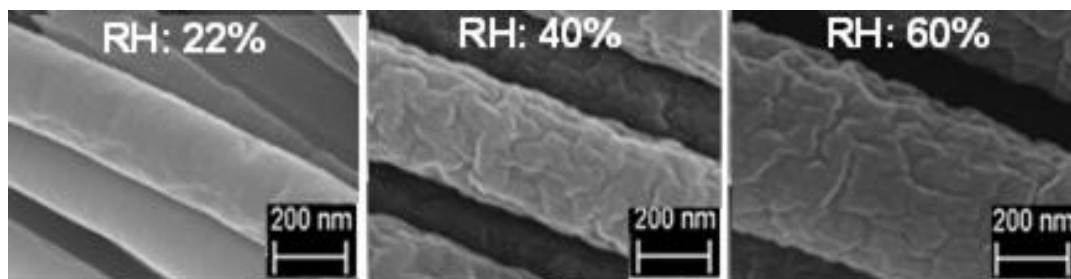


Figure 2.7 Effect of RH on the surface morphology of as-spun nanofiber produced from 10% PAN/DMF solution [109].

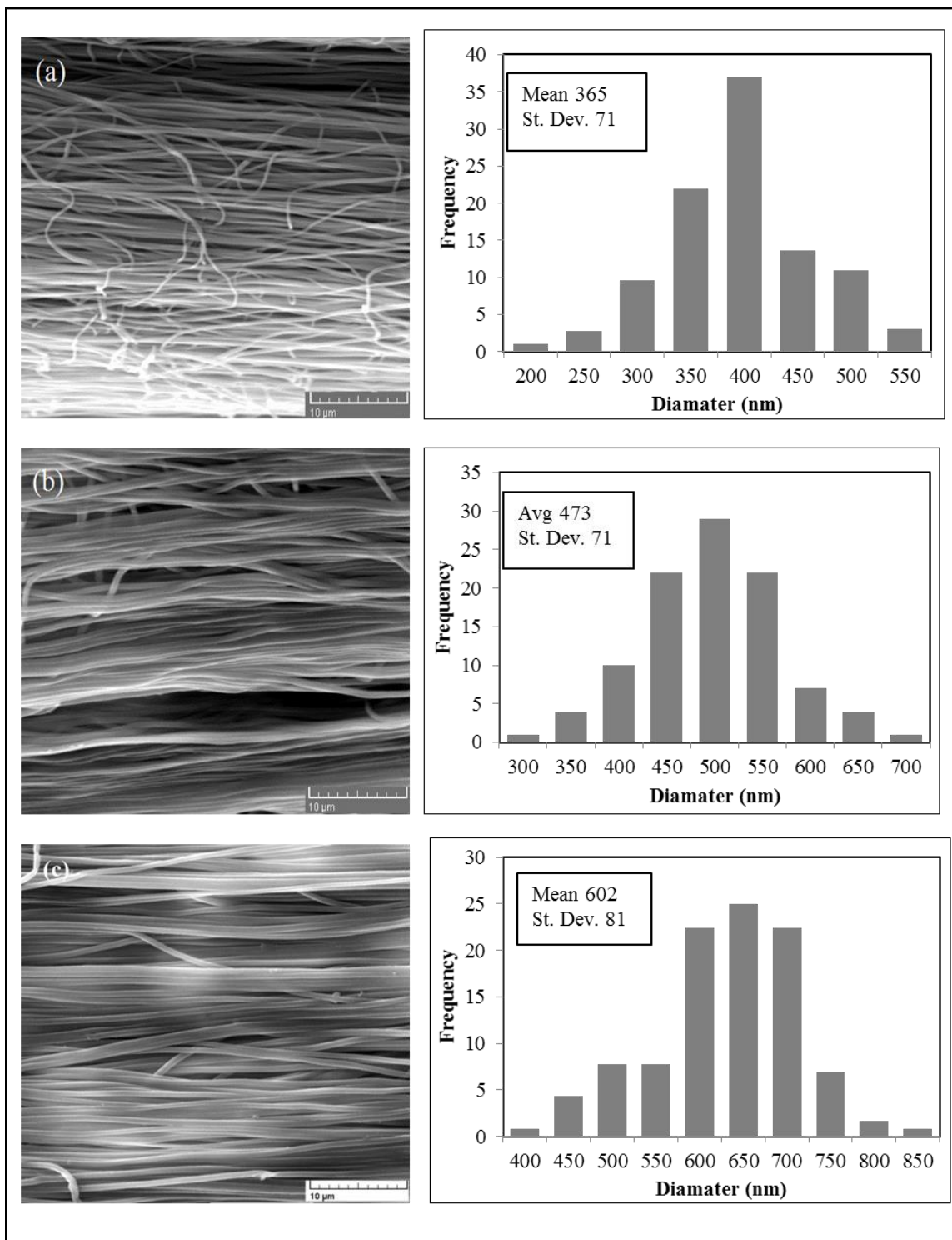


Figure 2.8 SEM images of electrospun nanofibers and diameter distribution at various RH. (a) 22% (b) 40% and (c) 60%.

Table 2.2 Summary of diameter distribution of as-spun, stabilized and carbonized nanofibers at different RH.

RH	As-Spun		Stabilized		Carbonized	
	Mean (nm)	St. Dev.(nm)	Mean (nm)	St. Dev.(nm)	Mean (nm)	St. Dev.(nm)
22%	365	71	319	59	224	37
40%	476	71	439	57	310	49
60%	602	81	538	86	432	74

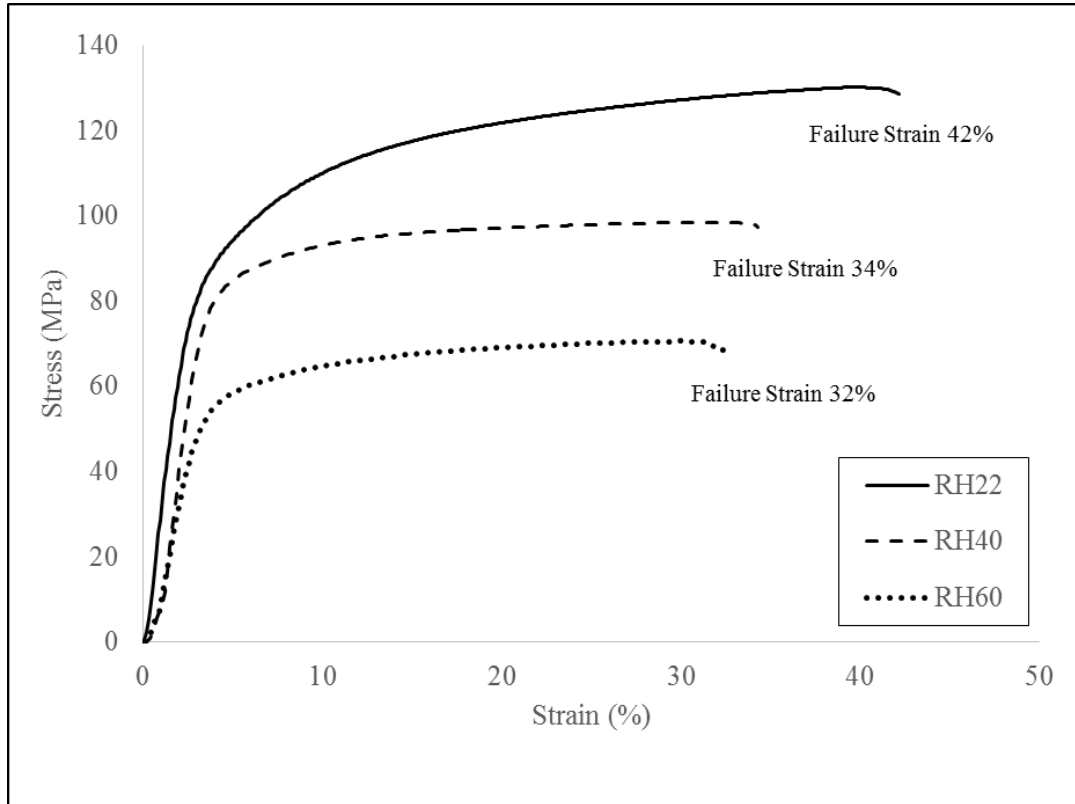


Figure 2.9 Stress strain curve PAN nanofiber where RH is 22%, 40% and 60%.

Table 2.3 summarizes the tensile properties of as-spun, stabilized and carbonized nanofiber yarns at different relative humidity. All nanofiber yarns produced at 22%RH

exhibit the highest tensile properties. The heat treatment process during stabilization and carbonization results in improved properties at 22% RH. However, stabilization degrades properties; a slight improvement in mechanical properties observed due to carbonization. Surface porosity or roughness may cause incomplete stabilization and defect formation in the nanofiber. Incomplete stabilization can affect the formation of ladder type structures which may further affect the carbonization stage. As a result, a catastrophic reduction in mechanical properties is obtained at higher RH conditions. The fiber diameter has a significant role on mechanical properties. Papkov et al. reported that the strength of PAN nanofibers increases from 15 MPa to 1750 MPa when fiber diameter reduces from 2.8 μm to 100nm [113]. Also surface roughness causes crack initiation under tensile load. This can be another reason for the lower mechanical properties of nanofibers produced at higher humidity condition.

Table 2.3 Tensile properties of as-spun, stabilized and carbonized respected to RH.

RH	As-Spun		Stabilized		Carbonized	
	Tensile strength (MPa)	Tensile modulus (GPa)	Tensile strength (MPa)	Tensile modulus (GPa)	Tensile strength (MPa)	Tensile modulus (GPa)
22%	131	5.1	164	13.7	459	39.3
40%	98	4.7	68	6.9	262	22.6
60%	71	4.4	34	5.3	157	13.5

2.6 Chapter Conclusion

In this chapter, collector types and electorspinning parameters are reviewed. A new high rpm rotary adjustable drum type versatile collector design is introduced for fabrication of aligned nanofibers. Additionally, RH effects on electrospun, stabilized, and carbonized nanofibers fabricated from PAN 10 wt.% in DMF were studied.

Manufacturing of aligned electrospun fibers is possible by manipulating electric field or employing a rotary collector. Although rearranging electric field improves fiber alignment, it is limited in terms of the fabrication scale. However, rotary disc type of collector results continuous, aligned nanofibers. A new hybrid (drum/disc) type of collector design withstanding high rpm is introduced. The system is able to successfully control environmental conditions (temperature and RH) and provides aligned fibers, even at low rpms.

RH has an important role on fiber diameter, surface roughness, and tensile properties of stabilized and carbonized nanofibers. The average diameter of the fiber increases from 365 nm at 22% RH to 602 nm at 60% RH. Additionally, higher RH shows wider fiber diameter distribution. Surface morphology is also affected by the humidity condition. A significantly porous structure is obtained at relative a humidity higher than 22%. Moreover, RH influences mechanical properties of as-spun, stabilized and canonized nanofiber yarns. Higher fiber diameter and surface roughness are believed to be possible reasons for lower mechanical properties. Highest tensile strength (about 459 MPa) is observed for carbon nanofiber produced at 22% RH, compared to about 157 MPa at 60% RH.

Chapter 3 : INVESTIGATION OF COLLECTOR DESIGN AND SPEED EFFECTS ON FIBER PROPERTIES

3.1 Introduction

Fiber alignment is critically important for certain applications of nanofibers, such as fuel cells [114], regulation of cell migration [55], and proliferation and differentiation [115]. Fiber alignment can be obtained by manipulating the electric field. However, it requires complicated devices and is limited in terms of fiber quantity and length. Another method is to use a rotary type collector. It has been reported that increasing collector speeds result better alignment. Kiselev et al. [116] found that an increase in the collector wheel speed yielded a reduction in fiber diameter and improved degree of alignment. Also, Haider et al. [117] achieved a reduction in fiber diameter from 163.9 to 137.4 nm by increasing collector surface speed from 2.09 to 21.98 m/s.

In this chapter, the influence of the collector geometry and collector speed effects on electrospun nanofibers produced from 10 wt% polyacrylonitrile (PAN) in N, N-dimethylformamide (DMF) solution is investigated. FEMM 4.2 open source 2D finite element method (FEM) software is employed to analyze the electric field. The alignment of as-spun nanofibers vary by changing the collector geometry (with variants such as copper foil, mesh, wire) and collector speed (from 9.9- 29.8 m/s) while keeping all the other electrospinning parameters constant. The as-spun PAN nanofibers are stabilized at 260°C in air followed by carbonization at 1000°C in nitrogen. The diameter distribution and alignment are investigated by scanning electron microscope (SEM). Mechanical properties are studied by dynamic mechanical analyzer (DMA).

3.2 Electric Field Analysis with Finite Element Method (FEA)

Electric field distribution and electric field strength are significantly important to manipulate fiber orientation and fiber quality. FEA analysis is frequently utilized to investigate electric fields [118 ,119]. FEMM 4.2 is a multi-purpose open source software, and is used to simulate the electric field for different collector geometries. Boundary conditions are applied from the experimental setup. The electrospinning setup box is assumed fully insulated. The distance between collector and needle is 18 cm. The needle is charged with 15 kV positive current and the collector is simulated as the ground (0 V). Relative electric permeability of air, needle tip, and collectors are taken to be 1. Relative humidity of air is ignored due to minor effects on the permeability of air [120]. Electric field and voltage distribution are investigated as 2D for all collector types.

3.3 Experimental

3.3.1 Electrospinning Process

The solution was electrospun inside an electrically isolated closed chamber. The spinning solution is held in a vertical syringe with a stainless-steel needle which is connected to a DC power supply. Figure 3.1 shows the three different types of collectors. Copper is used as the collector material due to its high conductivity and convenience of soldering the wire connection to the ground. The collectors are 0.1mm thick and 12 mm wide for the foil, 0.3 mm and pores of 2 mm for the copper mesh, and a diameter of 0.3mm for the individual wires in the wire collector. Collectors are placed using double sided tape on a 20 cm plastic disc and soldered to ground. The needle is located 18 cm above the surface of the disk and is held constant. The solution's flow rate is kept constant using a positive displacement syringe pump (KDS 200) purchased from KD Scientific Inc. The needle

is electrically connected to a positive high voltage DC power supply purchased from Spellman High Voltage Electronics Corporation. Barau and Saha [48] reported that the optimum flow rate and applied voltage is 15 $\mu\text{l}/\text{min}$ and 15 kV, respectively, for continuous and stable flow jet. The same parameters are used to achieve a stable jet during the electrospinning process, leading to improved mechanical properties of as-spun fiber yarns. The relative humidity is kept at a constant 22% by controlling the moist to dry air into chamber. Electrospinning is performed at different collector surface speeds 9.9, 14.8 and 29.8 m/s. The temperature is maintained at 20°C. Collectors are removed from the disc after depositing 50 μl of the solution.

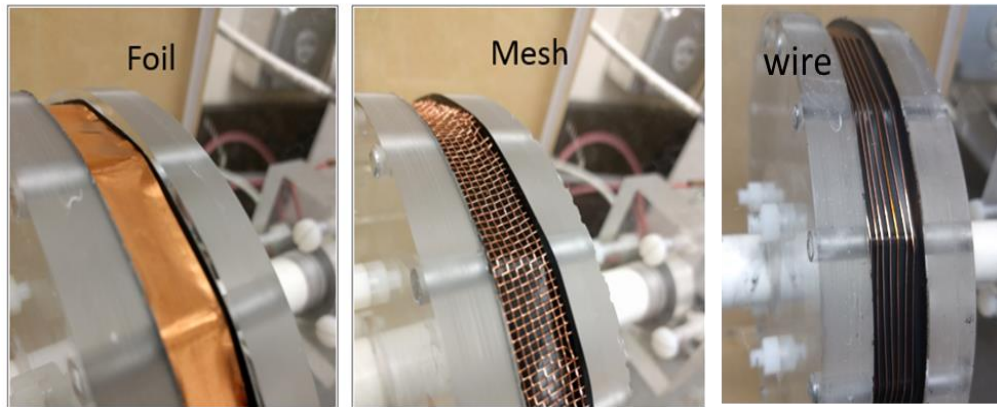


Figure 3.1 Collector types copper foil thickness 0.1 mm and 12 mm wide, mesh wire diameter 0.3 mm opening size 2 mm, wire diameter 0.3 mm.

3.3.2 Stabilization and Carbonization

After the drying process, the electrospun collectors are cut into 10 cm long pieces, and both ends are fixed by gluing with ceramic glue on a plate. A programmable air convection oven (Model 825, Cole-Parmer) is used for stabilization. The plate is heated in

the oven with a 5 °C/min ramp from room temperature to 260°C for 180 min. Barua and Saha reported that the optimum stabilization time at 260 °C is 180 min [112].

Finally, stabilized nanofiber films are carbonized at 1000 °C for 60 min in N₂ by employing a tube furnace (OFX-1200X, MTI). The temperature rate is 5°C/min, continuous N₂ flow is provided during the carbonization process. An inner graphite tube with samples inside is located in the quartz tube in order to reduce residual oxygen effects in the tube. Both ends of the films are left free during carbonization. N₂ purging is continued during cooling until the temperature drops to 200 °C.

3.3.3 Fiber Angle and Diameter Distribution Characterization

Fiber orientation and diameter distribution are investigated via SEM images. Deposited nanofibers are mounted on the SEM sample holder with collectors. The samples are sputter coated with iridium and examined under a Tescan VegaII SEM. ImageJ, an open source image analyzing software, is utilized to determine the diameter of the fibers. 100 measurements are performed for each set of fibers to obtain the mean and standard deviation values of the diameters.

3.3.4 Fiber Mat Porosity Characterization

Mat porosity is calculated with two different method methods. SEM images are used to determine porosity of mat by image analysis [121]. For all control groups, three SEM images are analyzed via ImageJ. Images are converted to binary, as shown in Figure 3.2. The total area of dark spots is taken as total pore area. The porosity is derived by proportion to the total area of the SEM images. The second method is to calculate the porosity by apparent density of the fiber mat. 200 µl of a solution is deposited at different

rpms and mat thickness is measured with high a accuracy micrometer. The apparent density and porosity are derived from Equation 3.1 and 3.2:

$$\rho_a = \frac{W_m}{d_m A_m} \quad (3.1)$$

$$Porosity = \left(1 - \frac{\rho_a}{\rho_b}\right) \times 100 \quad (3.2)$$

where ρ_a is apparent density, W_m is the mat mass, d_m is the average thickness of the mat, A_m is the total mat area, ρ_b is the bulk density of PAN [122].

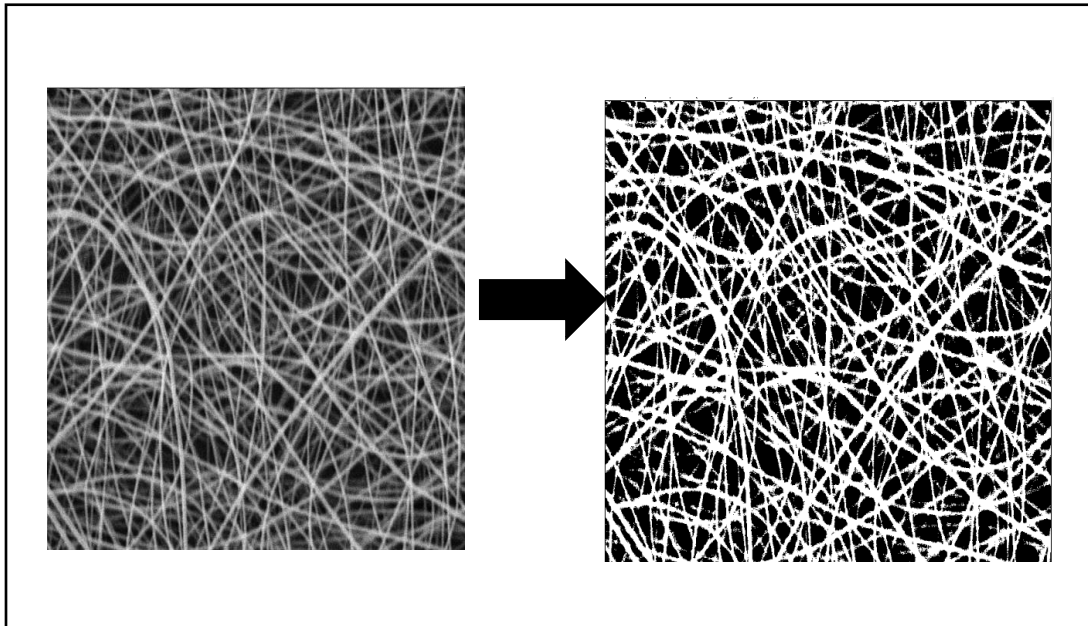


Figure 3.2 Image analysis method that followed for porosity calculation by converting the SEM images to binary.

3.3.5 Mechanical Test Sample Preparation

A method is developed to measure tensile properties with high accuracy without altering fiber orientation or damaging fibers. Figure 3.3 shows the method of preparing

mechanical test samples schematically. A stainless-steel punch system is designed to cut all carton window frames identically and allows mounting fibers on the carton window frame (a) along deposition direction. Two pieces of double-sided tape are placed on both ends of the frame (b). Fibers are stuck on the tape by gently pressing the foil (c). Extra yarn from top and bottom sides outside the window frame is trimmed (d). The piece of the collector is removed. Other sides of the double-sided tape are closed with carton slides so that it will not stick to the test fixture (e).

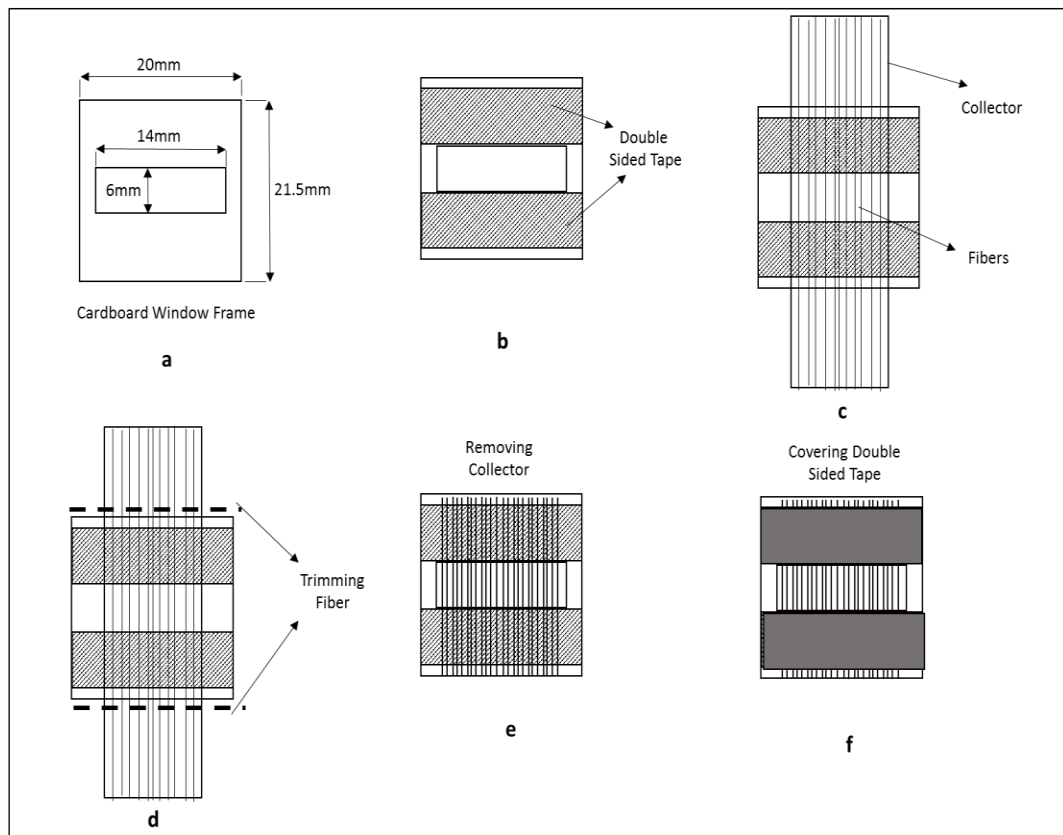


Figure 3.3 (a) Cutting carton board window frame via the mold (b) placing double-sided tape on both ends of the frame (c) sticking fibers on tape by gently pressing foil (d) Trimming yarn from top and bottom sides of the window frame (e) removing collector (f) closing other side of the double-sided tape with carton slides so that it will not stick test fixture.

3.3.6 Tensile Properties Measurement

A DMA Q800 from TA Instruments is employed for mechanical testing. The gauge length is 6 mm and the strain rate is 0.001 s^{-1} for e-spun fibers. Carbonized and stabilized samples are tested at force control mode, with a force ramp of 0.5 N/min. The cross-sectional area of the as-spun nanofiber yarn sample is calculated by dividing the mass of the yarn by the length of the sample and the density of PAN polymer. The density of the PAN is taken to be 1.18 g/cc [123]. The cross-sectional area was calculated from volume. The total number of fibers in the as-spun yarn was found from the mean diameter, obtained with the SEM fiber diameter analysis as below:

$$A_a = N \frac{\pi d_{am}^2}{4} \quad (3.3)$$

$$A_s = N \frac{\pi d_{sm}^2}{4}, \quad A_c = N \frac{\pi d_{cm}^2}{4} \quad (3.4)$$

where N is number of fibers in the yarn, d_{am} is the mean diameter of as-spun nanofibers, A_a is total cross section area of as-spun yarn. The cross-sectional areas of the stabilized and carbonized samples are calculated by the equation from the fiber diameter distribution. The number of fibers is assumed to be constant along the yarn. Once obtaining N from Equation 3.3, the cross sectional areas of stabilized and carbonized yarn are calculated using the Equation 3.4. d_{sm} , d_{cm} are the mean diameter of stabilized and carbonized nanofibers, A_s , A_c are total cross section area of stabilized and carbonized nanofibers.

3.4 Results and Discussion

3.4.1 Effect of Collector Design on Electric Field

3.4.1.1 Wire Opening Effect on Electric Field

Figure 3.4 shows 2D FEM simulation results of electric field distribution for three different wire opening: 1 mm, 2 mm, 3 mm. Only half of the simulation is represented due to symmetry on the y axis. Electric field distribution is shown as color scales for different electric field levels of the collectors. Electric field distribution is slightly altered by manipulating wire opening distance. While decreasing the opening distance, the electric field distribution becomes more homogenous, and weaker electric field density is obtained for the wires that are close to the center compared to those on the sides. Decreasing the opening distance may result in random fiber deposition between wires due to relatively higher electric field density between wires. On the other hand, increasing the distance will cause inhomogeneous deposition in terms of the number of fibers along the x axis. The 2 mm opening size is considered to be optimal for the current electrospinning setup, and will be the used design for further investigations.

3.4.1.2 Collector Geometry Effect on Electric Field

Figure 3.5 shows the 2D FEM simulation results of electric field distribution for foil, mesh, and wire collectors. According to the simulation results, collector geometry effects electric field distribution significantly. The highest electric field value on the collector surface is obtained for wire collector. Wire and mesh collectors also show more uniform electric field distribution compared to the foil type. Electric field accumulates on corners of the foil collector. Figure 3.6 shows the electric field distribution along the collector surface. The data is taken from 2D FEM analysis of the collector along the collector surface. Highest

values are obtained on the side of the collectors. However, wire and mesh collectors have much more intense electric fields compared to foil collector.

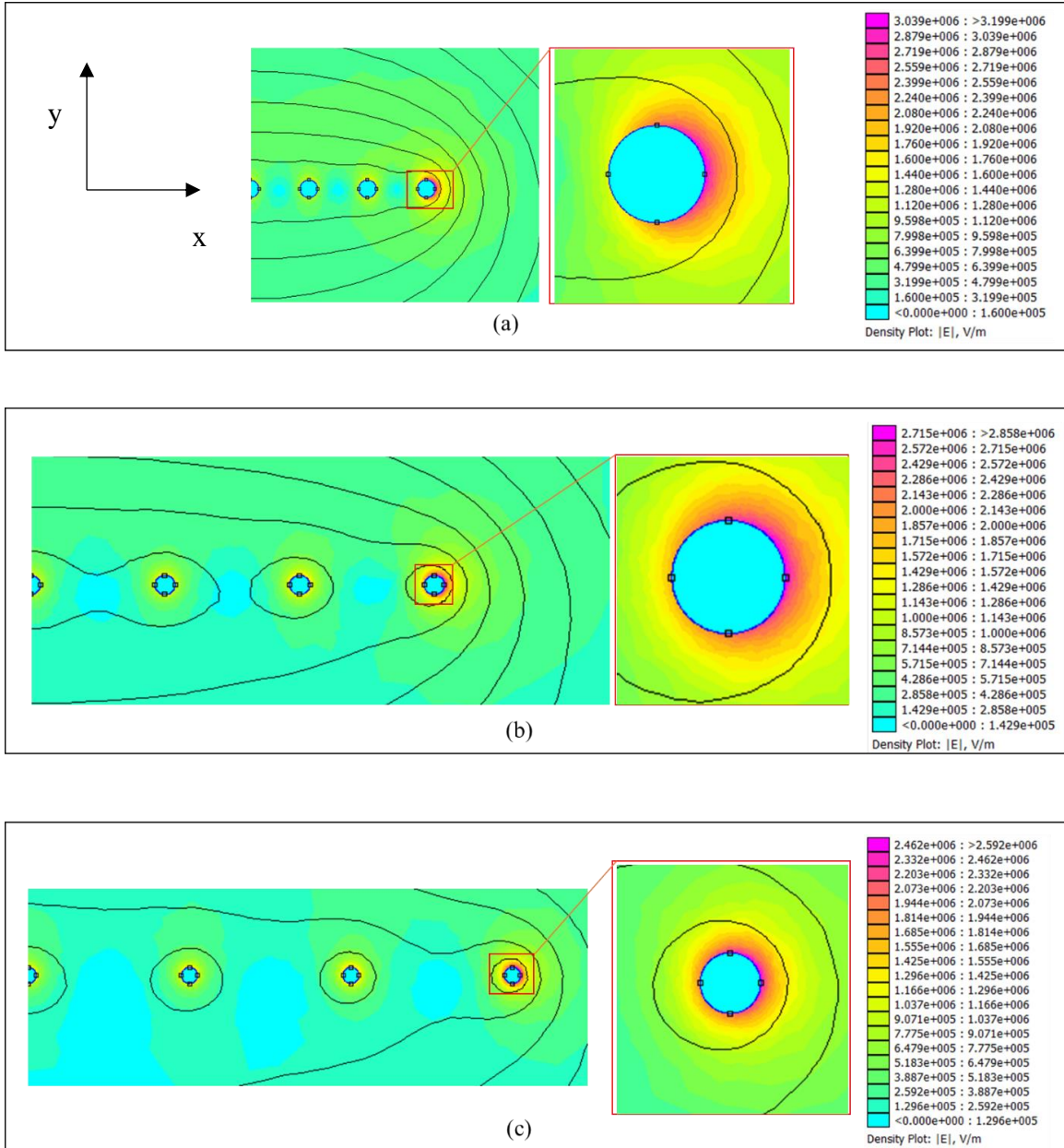


Figure 3.4 FEA simulation results of electric field distribution for wire type of collector wire diameter is 0.3 mm opening size (a) 1 mm (b) 2 mm (c) 3 mm.

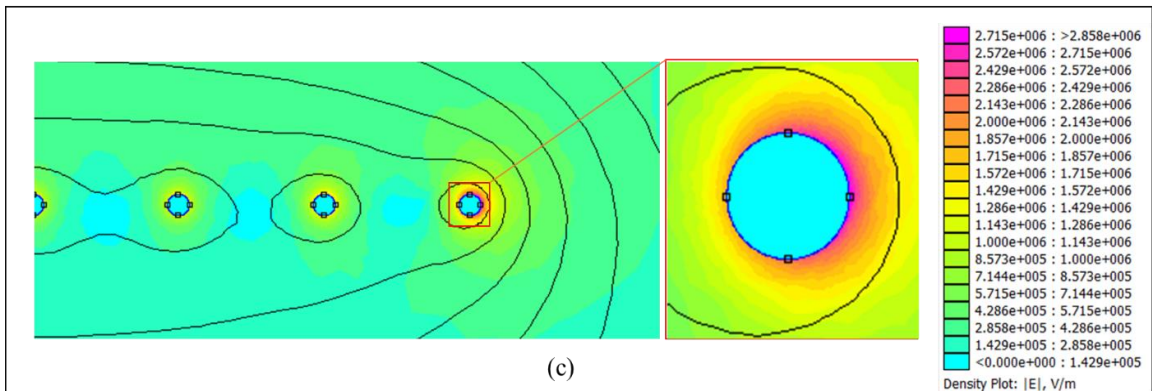
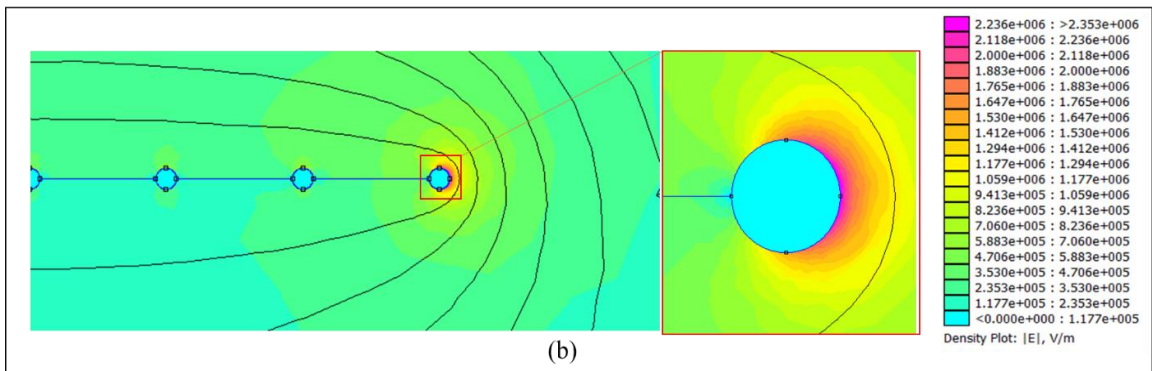
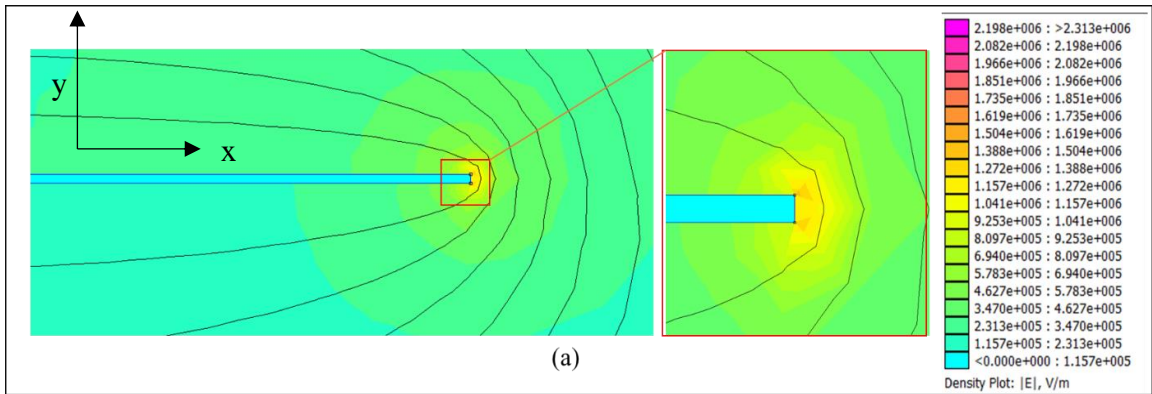


Figure 3.5 Electric field density distribution of foil (a), mesh (b) and wire (c) type of collector.

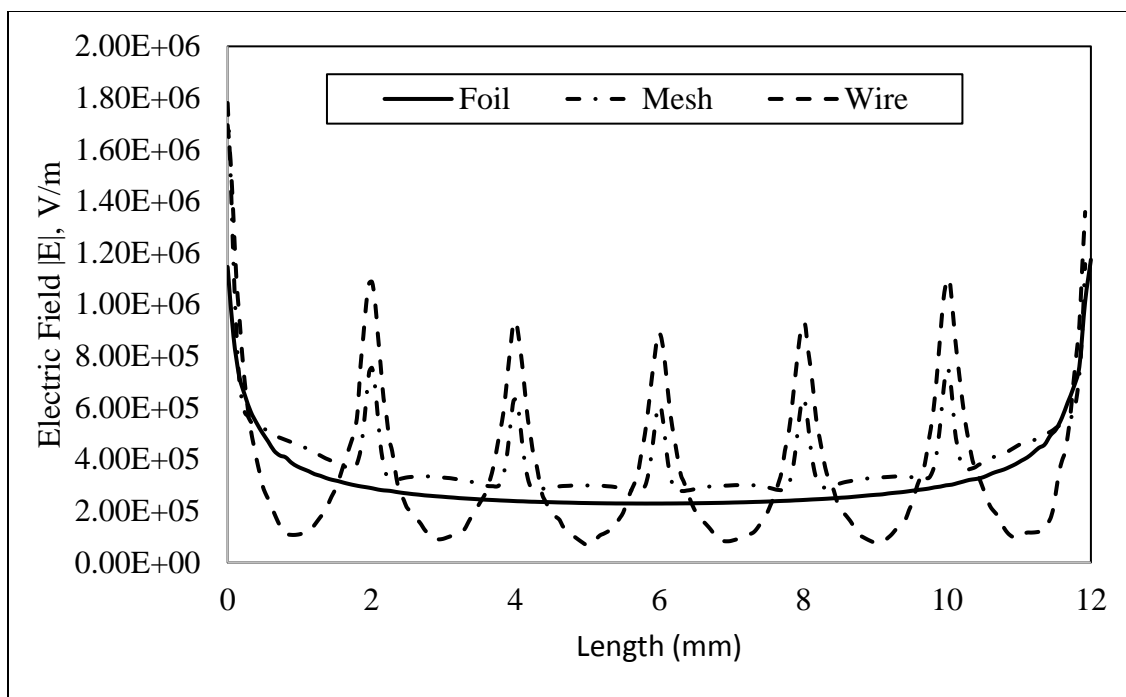


Figure 3.6 Electric field change along the collector surface for foil, mech and wire type of collector

3.4.2 Collector Speed Effects on Fiber Mat Porosity

Table 3.1 shows porosity for samples collected using foil, mesh, and wire collectors as a function of the collector speed. According to the image analysis results, collector speed influences electrospun nanofiber mat porosity. The highest porosity obtained is 55.7 % for nanofiber mats that are fabricated with the foil collector at 500 rpm. Increasing collector speed results in reduction on mat porosity. Aligned nanofiber film shows less porosity due to packing affect. Nanofiber mat thicknesses is measured from 100 rpm to 1500 rpm. Figure 3.7 shows porosity calculation results using the apparent density method as a function of collector speed. Collector speed also effects the porosity of nanofiber films at lower rpms. Up to 70% porosity is obtained at lower speed.

Table 3.1 Porosity of carbon nanofibers films for different collector geometries, derived by employing image method.

Collector	500 rpm	1000 rpm	1500 rpm
Foil	55.7% (± 5.7)	52.5% (± 5.2)	48.7% (± 4.6)
Mesh	47.4% (± 4.6)	43.8% (± 5.8)	37.4% (± 3.2)
Wire	46.3% (± 6.2)	44.1% (± 5.3)	35.3% (± 5.6)

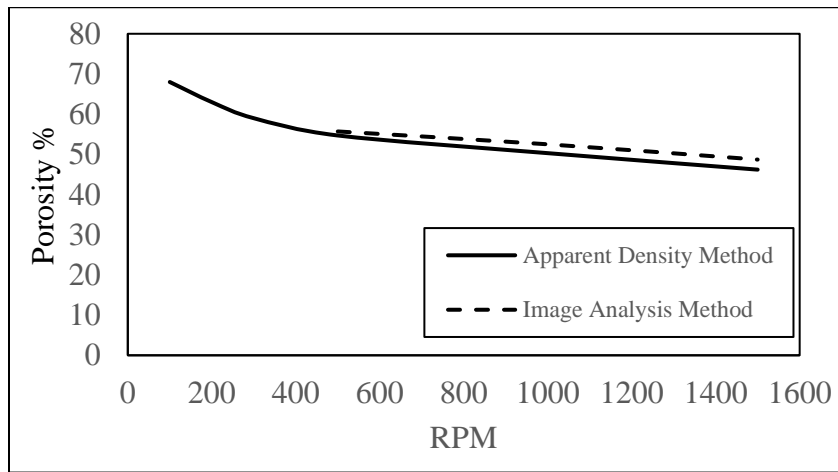


Figure 3.7 Porosity of nanofiber film as a function of collector speed for foil type of collector calculated by using apparent density method.

3.4.3 Collector Speed and Geometry Effects on Diameter Distribution and Fiber Alignment of Electrospun, Stabilized and Carbonized Fiber

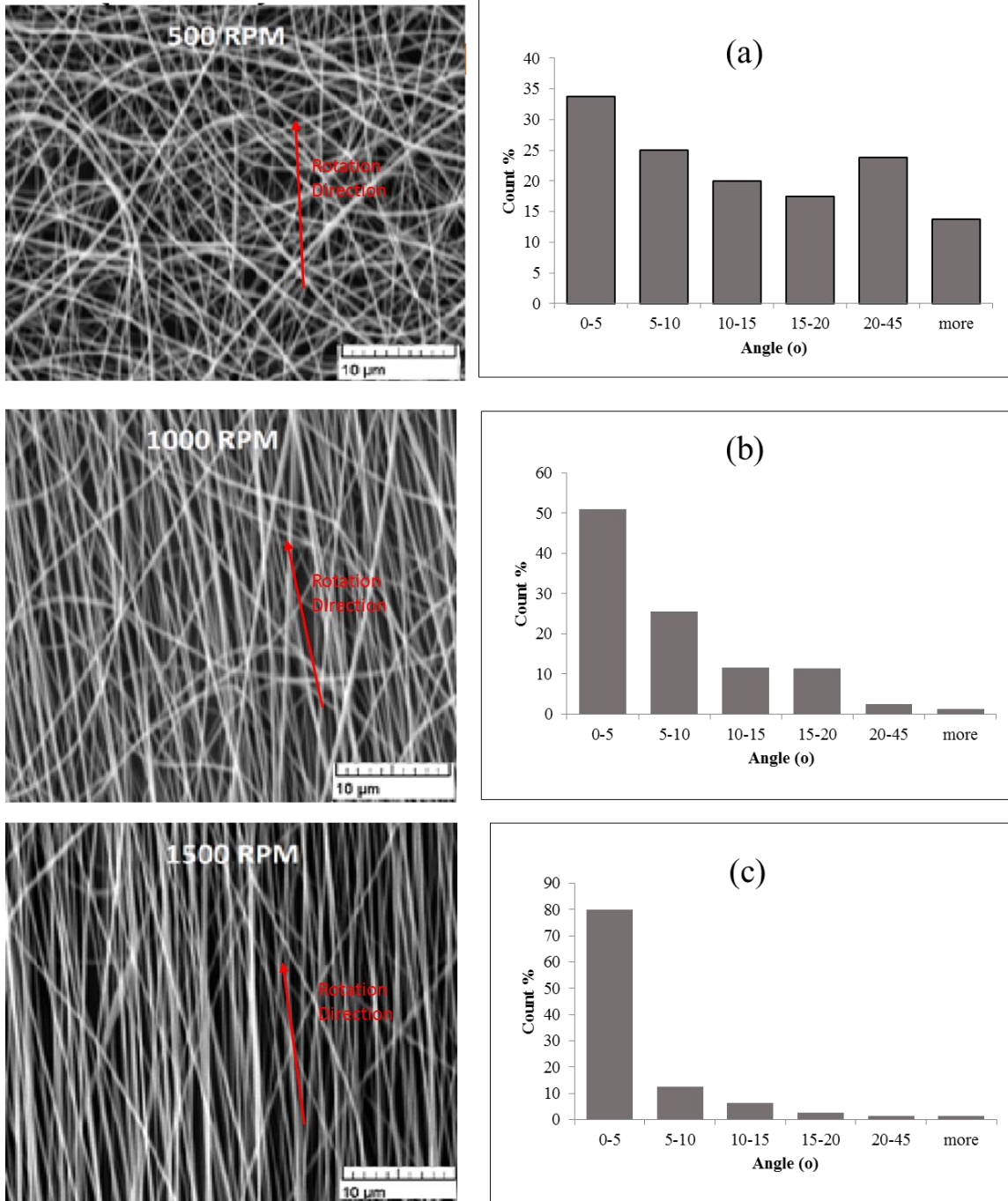
Figure 3.8 shows a few SEM images of as-spun nanofibers produced at different rpm and collector geometry. SEM results show that nanofibers at this low magnification seem uniform and defect free. At least 100 measurements of different fiber diameters were taken from the SEM images collected from different locations of the nanofiber tows. The angle distribution seems more widespread at 9.9 m/s compared to 29.8 m/s. At low rpm,

less ordered fibers are obtained for foil collector. Significant improvement was obtained by increasing collector speed. Figure 3.8 (a-c) indicates fibers became more ordered by increasing collector. 78% of fibers were within $0-5^\circ$ at 1500 rpm while only 34% fibers within $0-5^\circ$ whereas the collector speed is 500 rpm. For mesh and wire collectors, more ordered fibers are obtained, more than 90% of fibers are within $0-5^\circ$. Standard deviation of angle distributions is plotted as a function of rpm (Figure 3.9). Standard deviation reduces sharply between 500 and 1500 rpm for the foil type of collector. Standard deviation slightly decreases for wire and mesh collectors by increasing collector speed. The best alignment is obtained at 1500 rpm for the wire type of collector.

Table 3.2 shows average fiber diameter and standard deviation of all as-spun, stabilized, and carbonized nanofibers at different RPM. The average fiber diameter is reduced noticeably by increasing collector speed. Wire and mesh type collectors show minor improvement over 1000 rpm. All nanofibers experience shrinkage in their diameter during the heat treatment cycles. Additionally, average fiber diameter is reduced while collector disc speed increases. This reduction can be related to incoming fibers in the air experiencing additional mechanical stretching by connecting to the initially deposited fibers. Additionally, this phenomenon causes higher degree of alignment.

FEA simulations support the diameter and angle analysis based on SEM images. Electric field distribution has a significant effect on fiber orientation. A relatively intense electric field is observed on individual wires when compared foil collector. Fiber filaments tend to accumulate where the electrical force is stronger. Wire and mesh collector's geometry result in better fiber alignment due to relatively intensive electric fields on individual wire surfaces. Even though the mesh collector has the same wire opening and

wire diameter, the connection between wires weakens electric field. Maximum electric field intensity is obtained at 2.715×10^6 V/m for wire collectors, while mesh collectors produce 2.236×10^6 V/m.



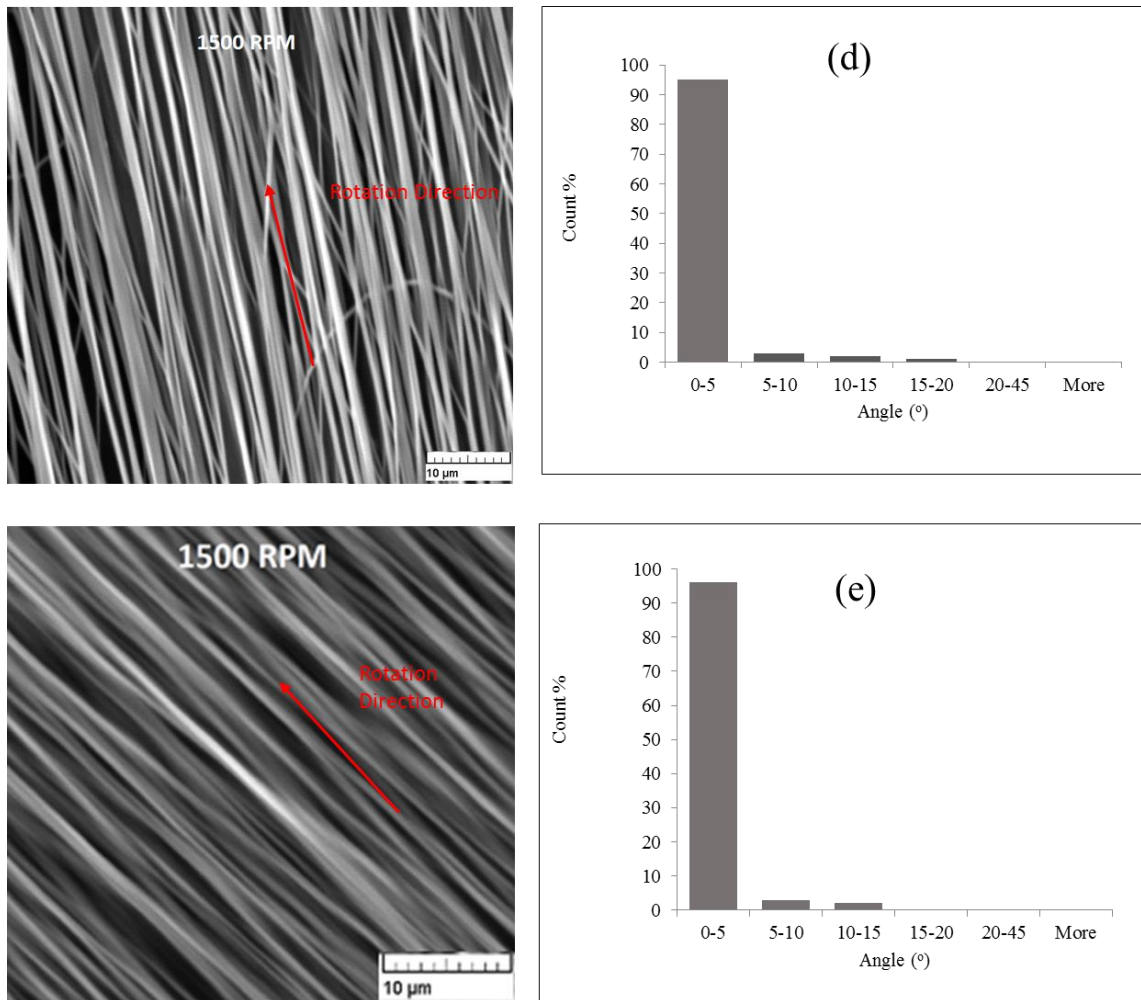


Figure 3.8 Histograms of PAN nanofibers angle distributions relative to mean orientation, a-c copper foil collector, d-) metal mesh and e-) wire collector. Red arrows indicate the rotation direction of the disc.

Additionally, mechanical stretching by rotating disc influences fiber diameter and alignment, while decreasing diameter is observed with an increase collector speed; standard deviation decreases as well. More uniform fibers are fabricated at higher speed. However, high collector speed, around 40 m/s, causes fiber breakage and lower crystallinity due to fast solvent evaporation [62].

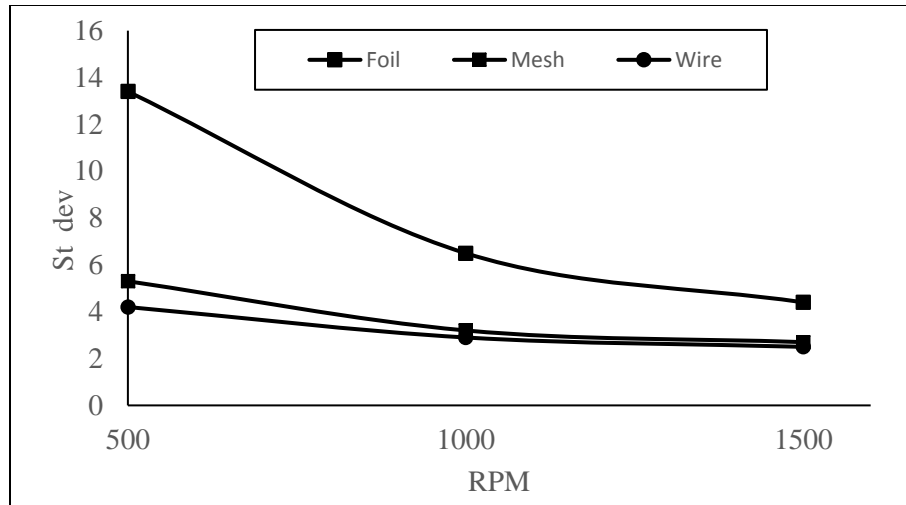


Figure 3.9 Standard deviation of electrospun PAN angle distributions as the function of collector plate speed.

Table 3.2 Summary of diameter distribution of as-spun, stabilized, and carbonized nanofibers at different rpm.

Collector	RPM	As-Spun		Stabilized		Carbonized	
		Mean	St.	Mean	St.	Mean	St.
		(nm)	Dev.(nm)	(nm)	Dev.(nm)	(nm)	Dev.(nm)
Foil	500	272	55	256	41	193	37
	1000	257	54	235	48	216	36
	1500	245	51	230	51	194	42
Mesh	500	291	55	269	47	204	39
	1000	267	47	247	39	198	38
	1500	259	58	239	40	197	36
Wire	500	290	62	256	42	212	40
	1000	262	48	250	39	208	36
	1500	258	51	244	47	204	41

3.4.4 Mechanical Properties of Electrospun, Stabilized and Carbonized Nanofibers

Figure 3.10 shows stress-strain behavior of as-spun fibers for foil, mesh and wire collectors. The highest ultimate strength is obtained for wire collectors. Stiffness is also improved for wire and mesh collectors. Carbonized nanofiber mechanical properties are also investigated. Figure 3.11 plots tensile test results of carbonized electrospun fibers. The highest strength and elastic modulus are obtained for carbonized fibers fabricated by employing the wire collector.

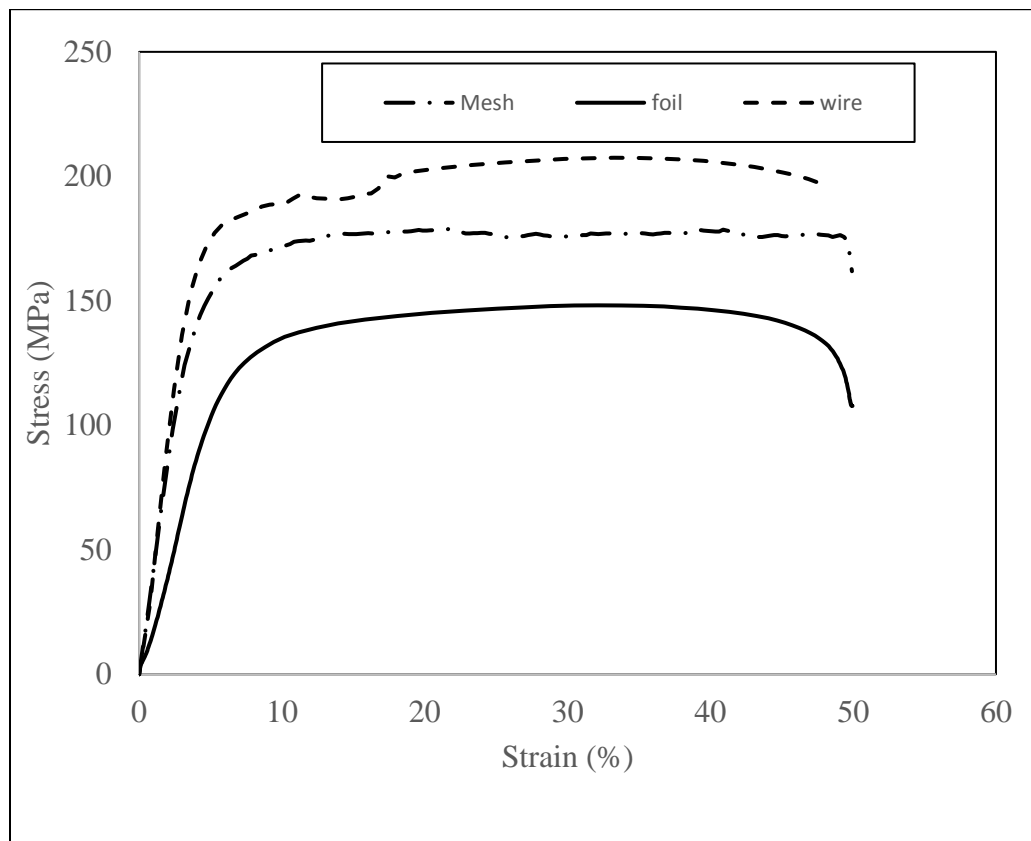


Figure 3.10 Stress-strain curve of as-spun fibers fabricated at 1500 rpm.

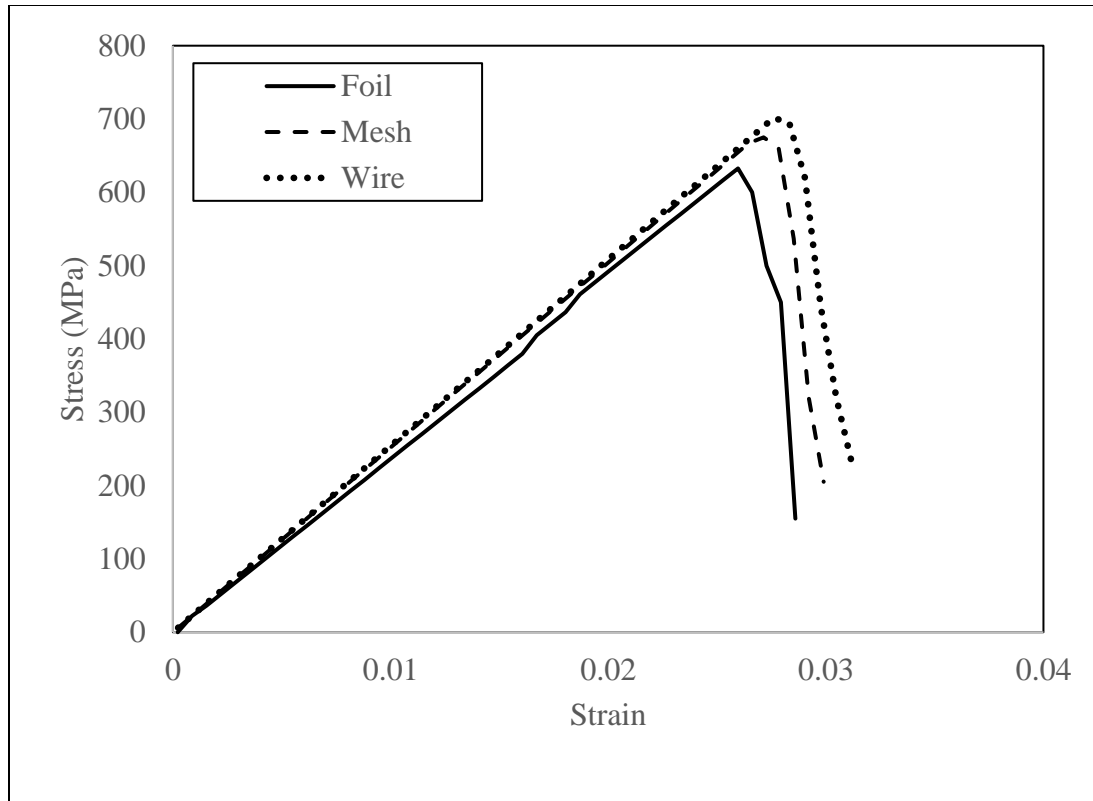


Figure 3.11 Stress strain curve carbonized nanofiber for three different collector geometry where rpm is 1500.

Table 3.3 summarizes the tensile properties of as-spun, stabilized, and carbonized nanofiber yarns at different RPM and collectors. As shown, all nanofiber yarns produced at 1500 RPM exhibit the highest tensile properties. Although the foil collector improves mechanical properties by increasing RPM, the wire collector produces fibers with the best mechanical properties. Degree of alignment might be related to tensile properties. Additionally, Ravandi et al. [124] reported that an increase in collector surface speed causes improvement in molecular level alignment. As a result, an improvement in mechanical properties is obtained by higher RPM conditions. Wire and mesh type collectors improve the degree of alignment compared to foil collectors.

Table 3.3 Tensile Properties of As-Spun, Stabilized and Carbonized Respected to rpm.

Collector	RPM/Surface Speed (m/s)	As-Spun		Stabilized		Carbonized	
		Tensile strength (MPa)	Tensile modulus (GPa)	Tensile strength (MPa)	Tensile modulus (GPa)	Tensile strength (MPa)	Tensile modulus (GPa)
Foil	500/9.9	128	5.1	168	13.8	512	40.1
	1000/14.8	142	6.2	187	14.1	598	51
	1500/29.8	161	6.4	226	14.9	657	57
Mesh	1500/29.8	179	6.6	233	15.3	675	58
Wire	1500/29.8	186	7.1	250.8	16.5	701	61

3.5 Chapter Conclusions

Collector geometry effects electric field distribution. Wire and mesh collectors have more intense and uniform electric distribution on the surface. This explains the reduction of fiber diameter and more ordered fibers in nanofiber films. Collector speed has an important role on fiber alignment, tensile properties of as-spun, stabilized and carbonized nanofibers. Lower rpm shows wider fiber angle distribution and higher standard deviation. The wire collector shows better fiber alignment at the same collector speed compared to mesh and foil collectors. Moreover, rpm influences mechanical properties of electrospun, stabilized and carbonized nanofiber yarns. Higher standard deviation of angle distribution is believed to be possible reasons for lower mechanical properties. The highest tensile strength (about 701 MPa) is obtained for carbon nanofiber produced at 1500 RPM with the wire collector, compared to about 512 MPa at 500 RPM. Manipulating collector geometry results in improved electric field intensity to fabricate aligned fiber, leading to improved mechanical properties.

Chapter 4 : INVESTIGATION OF ELECTRODE GEOMETRY

4.1. Introduction

Electrode or needle tip design influences the electric field as well as collector geometry. A needle is commonly used to guide the solvent that transforms into a droplet. There are a few advantages of employing a needle, such as simplicity, ease of maintenance, and unclogged orifices. However, this method requires relatively high voltage. Also, spinneret systems are employed to yield uniform fiber diameter, and relatively low voltage requirement [125]. These spinneret designs are called “needleless” systems. They include various geometries, such as flat spinnerets [126–128], rotating wire spinneret [129], metal roller spinneret [130], and stepped pyramid spinneret [131] (Figure 4.1). Needleless electrodes can be designed with multiple holes that result in high production rates. These systems are usually used for mass production of fiber mats while using relatively larger collectors, such as a cylinder [125]. However, a flat type spinneret electrode results in more uniform electric fields [126, 127].

In this chapter, three different electrode configurations and traditional needle tip are studied. Figure 4.2 shows schematic view and dimensions of the electrodes; (a) stainless needle (ID is 0.41 mm OD is 0.80 mm), (b) flash (OD=12mm, ID=0.8mm, and thickness=6mm) and (c) protruded (OD=12mm, ID=0.8 mm and thickness=5.5mm). Flash needle places the stainless-steel needle inside a copper cylinder. The protruded needle places the stainless-steel needle in a copper cylinder with the needle protruding 0.5 mm past the copper cylinder. FEMM 4.2 open source 2D FEA software is employed to analyze electric field distribution and potential difference effects. Taylor Cone formation and straight jet geometry are investigated by utilizing an optical camera at high-speed camera.

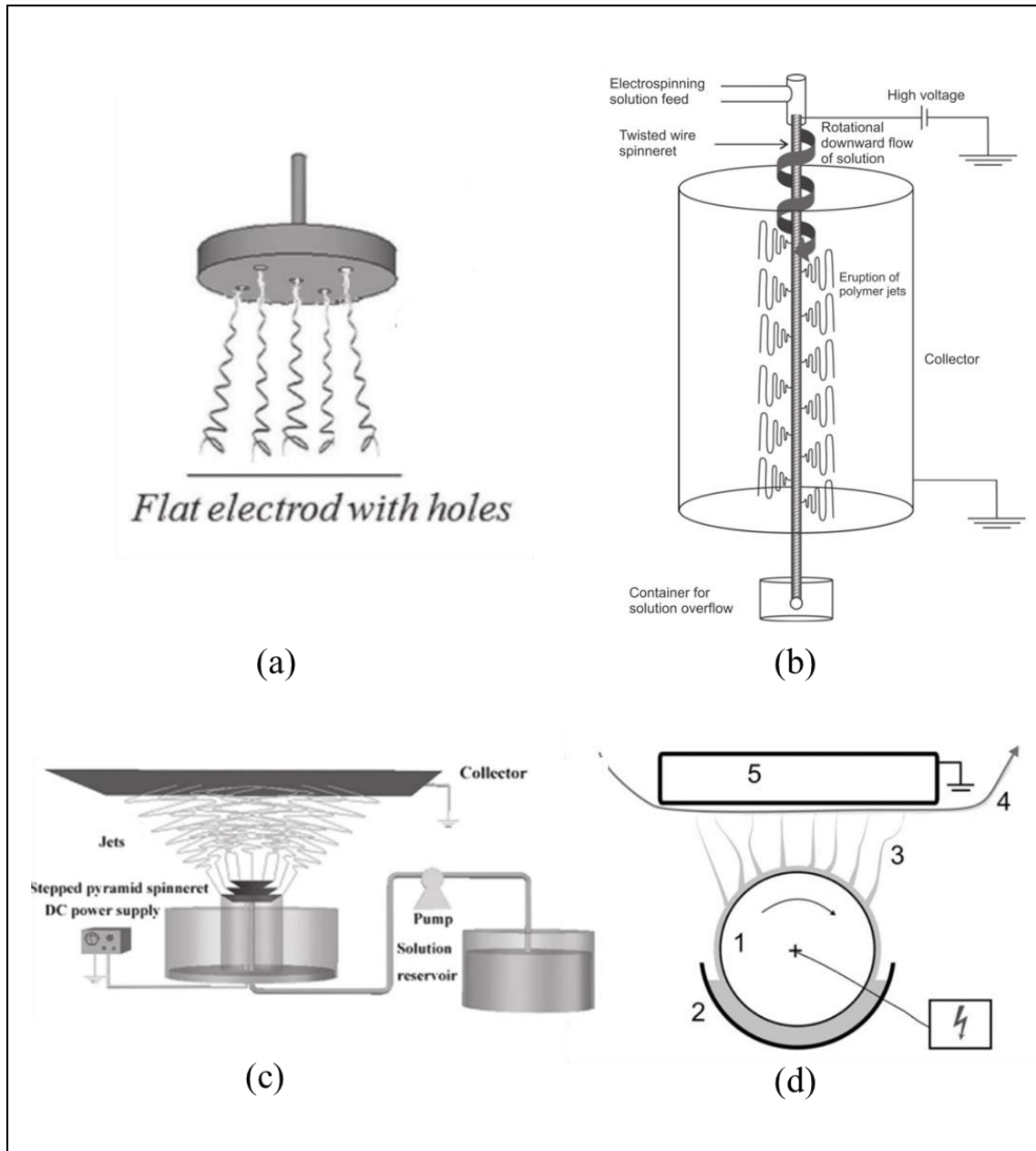


Figure 4.1 Scheme of the different types spinneret; (a) flat; [125](b) twisted wire electrospinning setup, the polymer solution is fed to the top; [129](c) stepped pyramid; [131](d) metal roller type spinneret and system components; (d-1) the roller; (d-2) solution reservoir; (d-3) fiber formation direction; (d-4) deposited fibers; (d-5) collector [130].

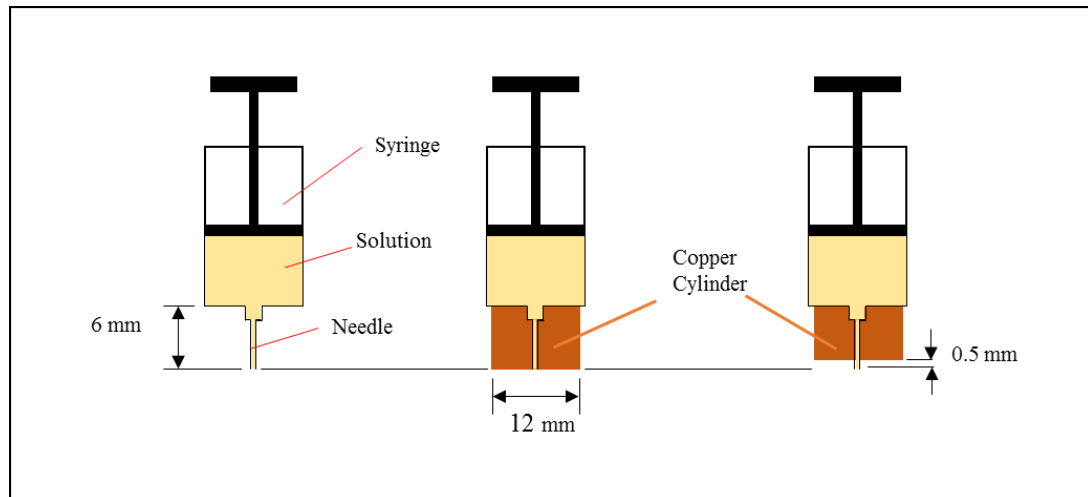


Figure 4.2 Schematic view of different electrode types, a- blind needle, b- flash, c- protruded.

Diameter distribution, morphology, and alignment of electrospun nanofibers produced from a 10% polyacrylonitrile (PAN) in N, N-dimethylformamide (DMF) solution, are analyzed via SEM images. The same solution preparation procedure from section 2.5.1 is followed. Additionally, tensile properties are investigated, and sample preparation steps (section 3.3.5) and mechanical test protocol (section 3.3.6) are followed.

4.2 Finite Element Analysis of Different Electrode Geometry

A procedure similar to that in section 3.2 is followed. However, in this chapter, the collector design is a wire collector and only the electrode geometry is altered. The electrodes are charged with 15 kV positive current and the collector is simulated to be ground (0 V). Additionally, the effects of applied voltage effect is investigated. The flash electrode is charged between 10 to 25 kV.

4.3 Experimental

4.3.1 Optic and High-Speed Camera Analysis

A Nikon D5200 digital optic camera is employed to take images of the Taylor cone. A Redlake Motion Pro X3 high speed camera equipped with 25 mm manual lens is utilized; a 1000 watt halogen light source is used to illuminate the setup. The high speed camera images at 1000 frames per second (fps) with a $100\ \mu\text{s}$ exposure. Figure 4.3 is an image of high speed camera setup.

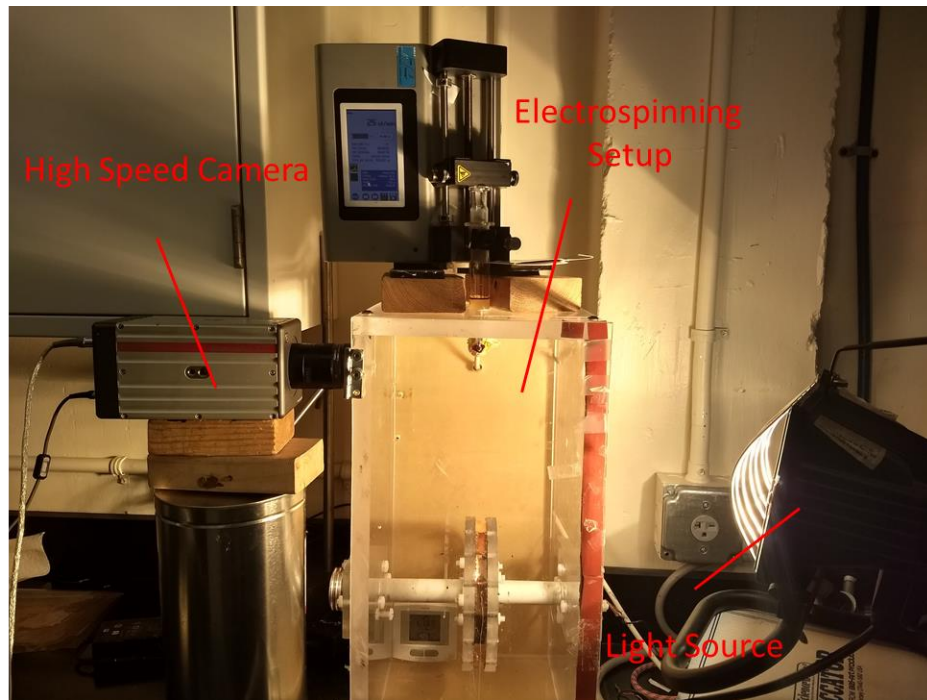


Figure 4.3 High speed camera setup.

4.3.2 Taylor Cone Straight Jet Formation Analysis

Optical camera images are used to analyze Taylor cone angle, Taylor cone area, and jet type. The flow is observed for approximately 5 minutes and intermittent images are taken. ImageJ is employed to derive angle and Taylor cone area. 100 images are taken, for

each control group, with the high speed camera. Straight jet length, diameter and angle are derived with ImageJ.

4.3.3 Fiber Angle and Diameter Analysis

Two different fiber diameter analyses are performed: different individual fibers diameter from relatively low magnified images, and along on one single fiber from high magnified images. The same procedure as section 3.3.3 is followed for angle analysis.

4.4 Results and Discussion

4.4.1 Electrode Geometry Effects on Electric Field Distribution

The effect of the electrode diameter on electric field distribution is investigated via FEA. Figure 4.4 shows the electric intensity between the electrode and collector from the surface of the electrode needle vs. flash needle with varying OD (2 mm for electrode, and 12 mm for flash). When the electrode diameter increases, a more uniform electric field distribution is observed. The needle shows an immediate drop, while the flash type electrode results in a more gradually reduction.

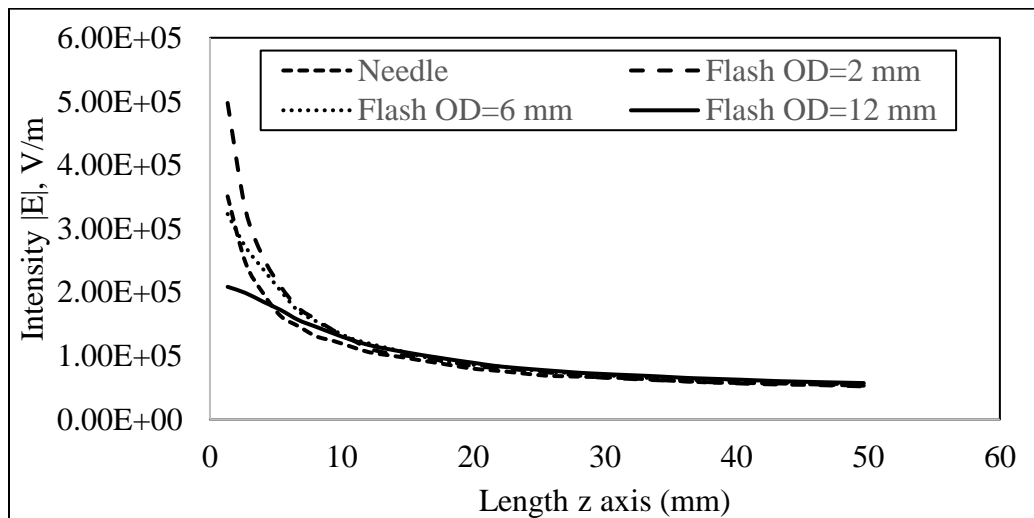


Figure 4.4 FEA result of electric field intensity from electrode through the collector, potential difference is 15kv for needle, flash type OD= 2, 6, and 12 mm.

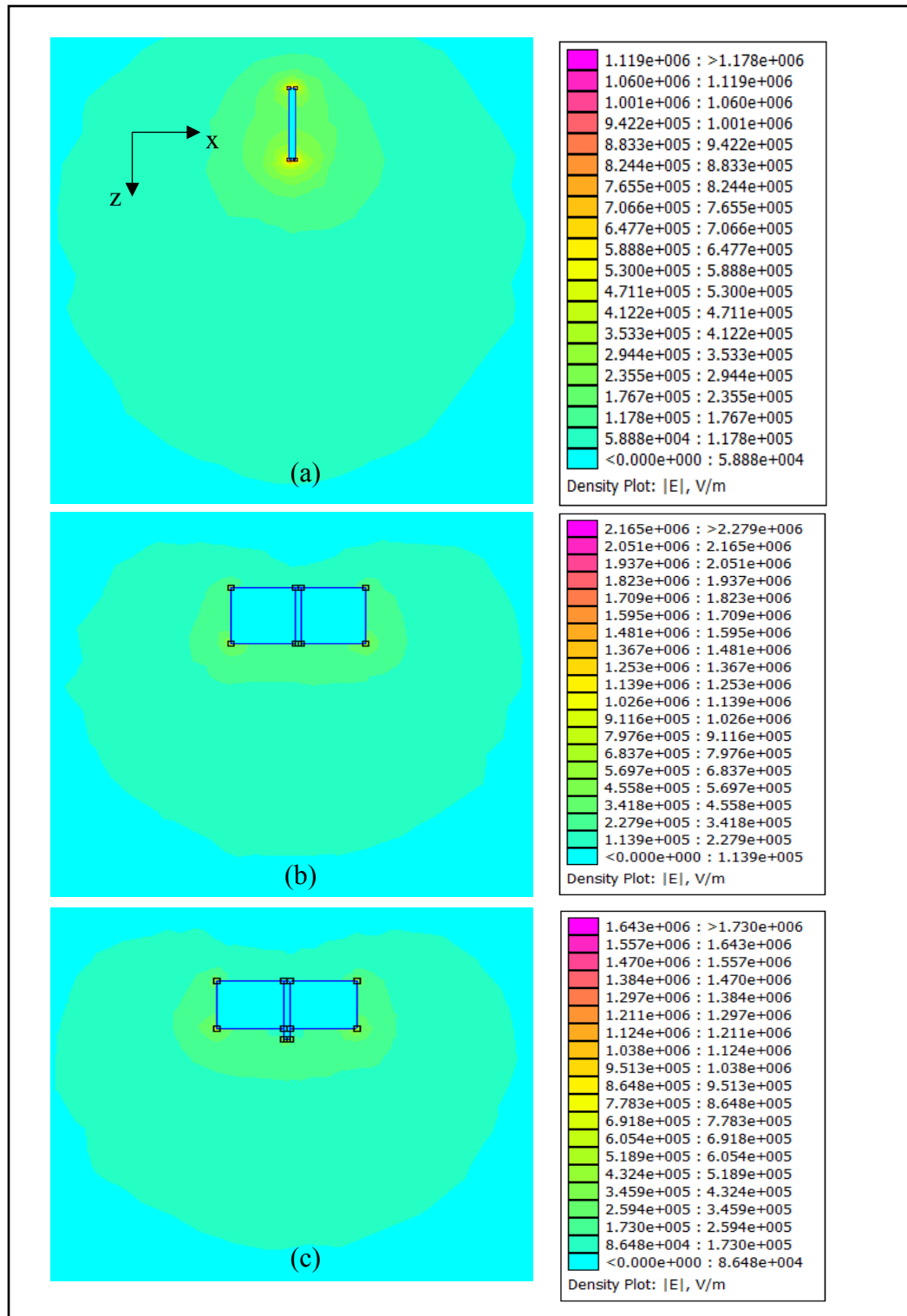


Figure 4.5 FEA plots of electric field intensity around needle tip where the potential difference is 15kv for (a) needle, (b) flash, and (b) protruded type of electrode.

Figure 4.5 shows colored electric field distribution results for needle, flash, and protruded electrode geometry. Flash and protruded types result in similar electric field intensity behavior. A 0.5 mm sputtered needle, compared to flash flat surface, does not alter the electric field significantly. On the other hand, the electrode needle shows a very intense electric field on the surface of the needle. Figure 4.6 is plotted to compare electric field intensity numerically between electrode surface and collector (on the z axis) for all three types of electrodes. The intensity varies from 50×10^3 to 20×10^4 V/m along the z axis. Flash and protruded electrodes tend to preserve intensity more compared to needle electrodes.

Applied voltage effects on the electric field are investigated by FEA simulations. Figure 4.7 plots the effects of applied voltage on electric field intensity along the z axis. The flash electrode is analyzed for different applied voltages, between 10 and 25 kV. Low applied voltages reveal that electric intensity changes rapidly through z axis compared to relatively high voltages, such as 20 kV and 25 kV.

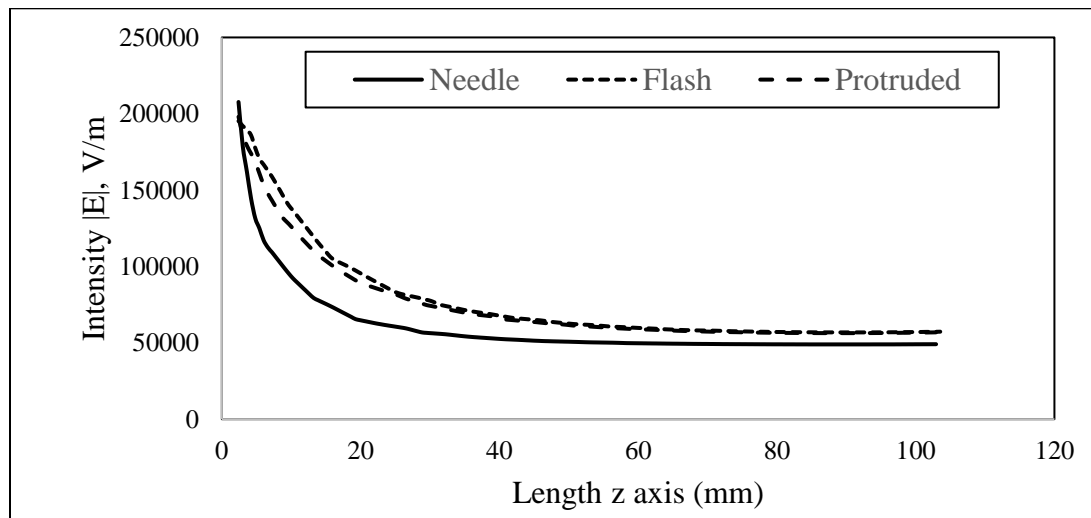


Figure 4.6 Electric field intensity from electrode through the collector where potential difference is 15kv for needle, flash, and protruded type of electrode.

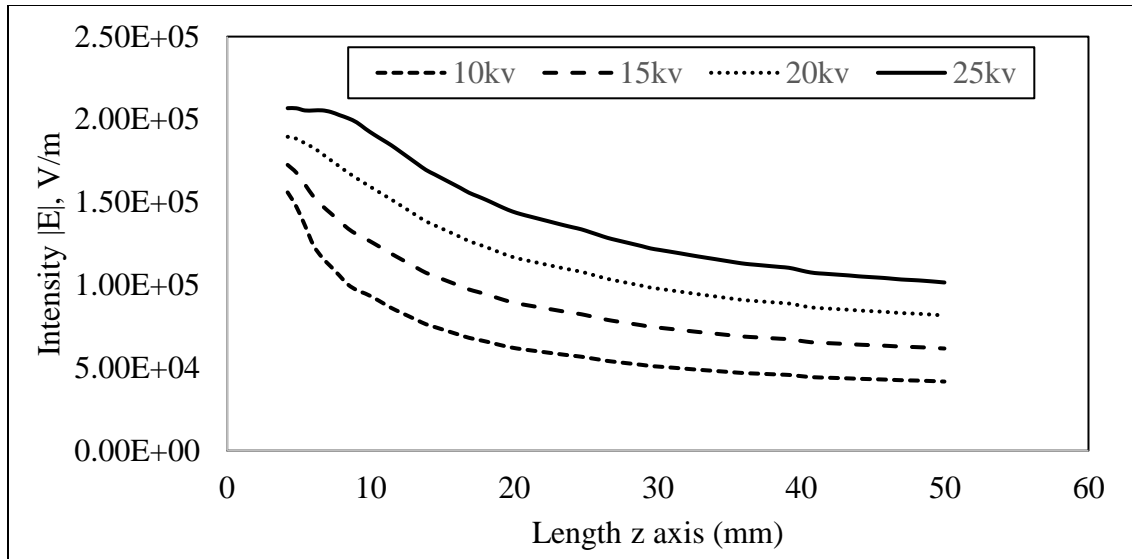


Figure 4.7 FEA result of electric field intensity as a function of applied voltage from electrode through the collector.

4.4.2 Electrode Geometry Effect on Taylor Cone and Jet Formation

Taylor cone shape varies depending on processing conditions, and electrode geometry. In this study, an optic camera is employed to study the Taylor cone at different flow rates. Figure 4.8 shows various Taylor cone morphologies observed for different electrode geometries (needle, flash, and protruded) at a flow rates of 13 $\mu\text{l}/\text{min}$ and 15kV. Taylor cone angle, Taylor cone area, and jet types are monitored at different flow rates. The flash electrode results in relatively larger Taylor cone and wider angles due to droplet development on the larger surface compared to needle tip. Straight jet formation is observed as soon as applied voltage is applied to the needle tip, but a certain amount of solution accumulation (between 30 to 40 μL) is required to develop the straight jet for flash electrodes. Table 1 summarizes Taylor cone angle, area, and jet type at different flow rates. At high flow rates, intermittent droplets are observed due to insufficient charge density resulting in an inability to remove fluid. Decreasing the flow rate below a critical value

causes a narrow intermittent continuous jet regime. The half angle (α) (Figure 4.9) rises with an increase in flow rate. α between 31.2° and 36.4° yields a continuous flow jet for the needle when the corresponding flow rate is $10 \mu\text{l}/\text{min}$ and $13 \mu\text{l}/\text{min}$. However, a continuous jet flow range is found between $12 \mu\text{l}/\text{min}$ to $20 \mu\text{l}/\text{min}$, with corresponding α angles of 31.2° and 40.7° , respectively. The half angle for continuous jet flow is reported to be between 32 to 46° [132]. Experimental results are close to the literature values. Jet flow without intermittent drops or intermittent flow is obtained at $10\text{-}15 \mu\text{l}/\text{min}$ for protruded electrodes, and $12\text{-}20 \mu\text{l}/\text{min}$ for flash electrodes. A wider flow rate range for stable flow jet is found compared to needle electrodes.

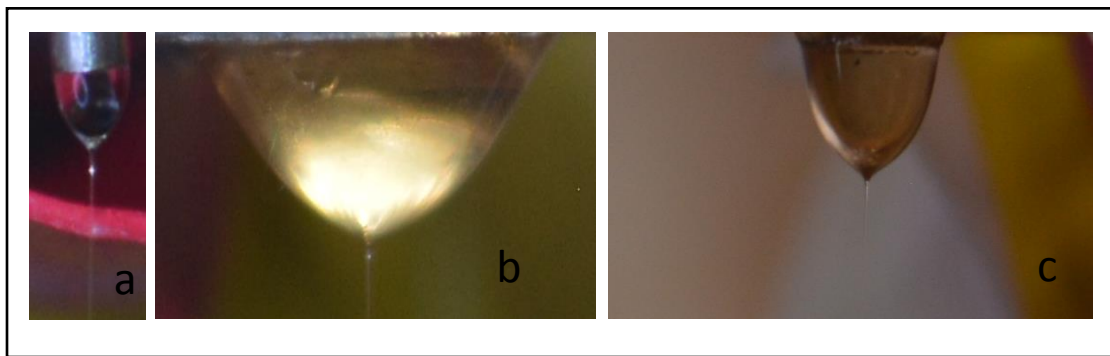


Figure 4.8 Taylor cone shape at $13 \mu\text{l}/\text{min}$ flow rate and 15kV for (a) needle tip, (b) flash (c) protruded.

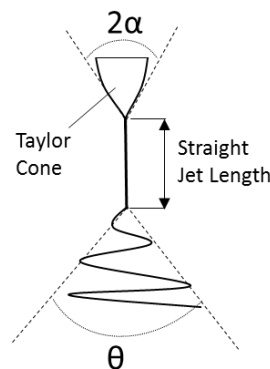


Figure 4.9 Demonstration of Taylor cone half angle α , straight jet length, and θ cone angle.

Table 4.1 Summary of optic camera analysis of Taylor cone angle, area and jet type at different flow rates.

Needle				
Flow Rate ($\mu\text{l}/\text{min}$)	Angle ($^{\circ}$)		Taylor's Cone Area (mm^2)	Jet Type
8	50.9		0.106	Narrow Intermittent Continuous
10	62.5		0.197	Continuous
12	64.7		0.432	Continuous
13	72.9		0.613	Continuous
15	94.8		0.637	Continuous with intermittent drops
Flash				
8	63.1		4.236	Narrow Intermittent Continuous
10	67.4		6.256	Narrow Intermittent Continuous
12	76.4		8.157	Continuous
13	77.9		9.006	Continuous
15	76.6		8.971	Continuous
20	81.4		9.964	Continuous
25	105.5		12.55	Continuous with intermittent drops
Protruded				
8	55.1		2.979	Narrow Intermittent Continuous
10	55.8		3.221	Continuous
12	63.2		5.021	Continuous
13	66.2		6.441	Continuous
15	67.3		6.599	Continuous
20	98.1		8.231	Continuous with intermittent drops

The straight jet experiences a series of bending loops and whipping instability after jet formation. In order to study the bending mechanisms at the tip of the straight jet, a more robust characterization technique is needed. A high speed camera is employed to investigate straight jet length, diameter, and cone angle (Figure 4.9). Electrode geometry influences characteristic of bending loops and whipping instability significantly. Additionally, applied voltage influences straight jet and whipping characteristics. Flash and protruded electrodes result in longer straight jets, compared to needle, when applied voltage is 15 kV (as seen at Figure 4.10). Additionally, thinner straight jet formation is found for flash and protruded electrode compared to needle electrodes.

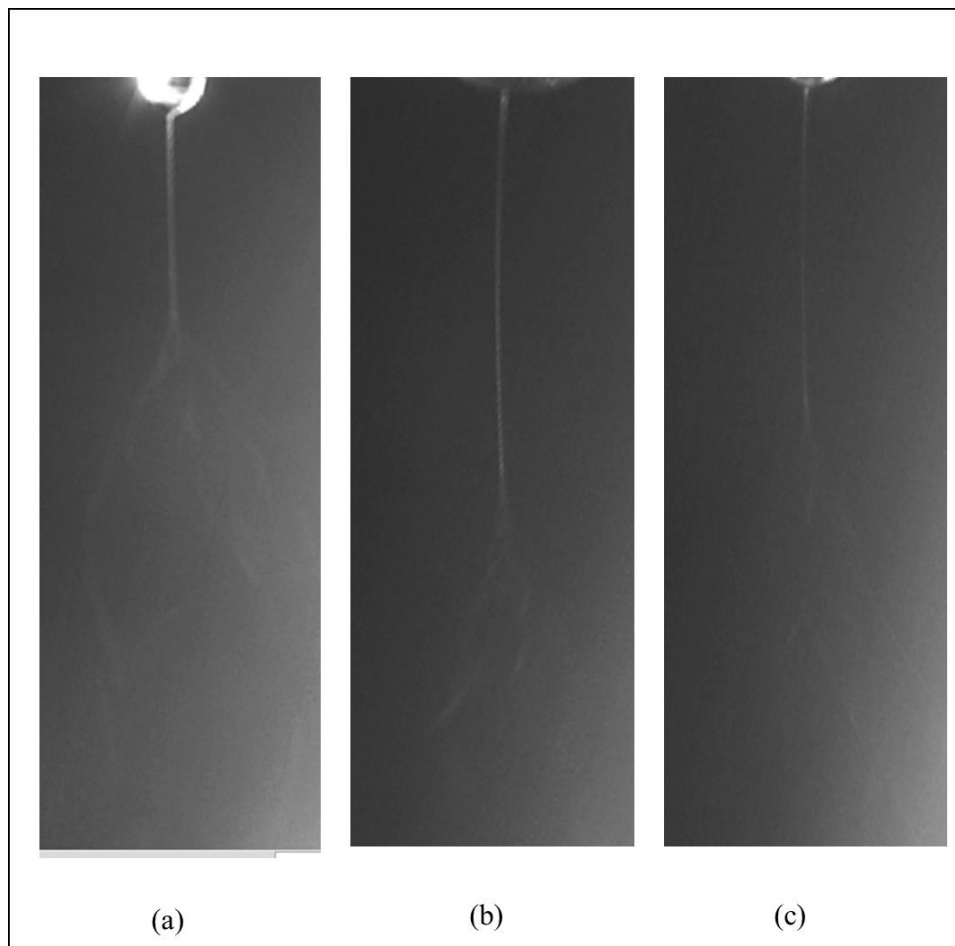


Figure 4.10 High speed camera image of (a) needle, (b) flash, and (c) protruded type of electrode (15 kV, 13 $\mu\text{l}/\text{min}$ flow rate, 1000 fps, and 100 μs exposure).

Applied voltage alters straight jet formation. Figure 4.11 shows straight jet formation for needle, flash, and protruded electrodes, with an applied voltage of 19 kV. Similarly, straight jet formation varies depending on electrode type at higher voltages as well. However, when the applied voltage increases straight jet length rises. Table 4. 2 summarizes the high speed camera image analysis. Multiple images are taken for all electrode types, and applied voltage is varied between 15 kV to 19 kV. A trend is found as a function of the applied voltage. Straight jet diameter and length increases by increasing positive discharge on the electrode. Additionally, the angle where whipping motion begins to form is influenced by electrode type and applied voltage.

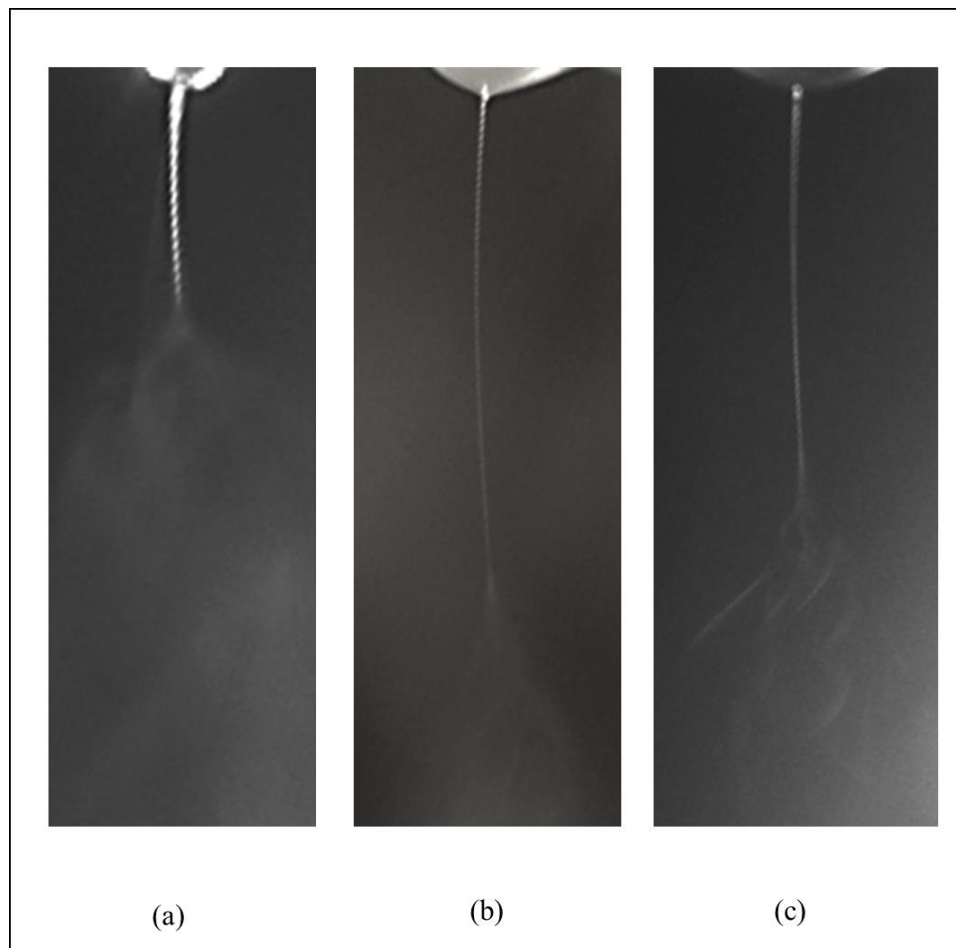


Figure 4.11 High speed camera image of needle, flash, and protruded type of electrode (19 kV, 13 $\mu\text{l}/\text{min}$ flow rate, 1000 fps, and 100 μs exposure).

Table 4.2 Summary of high speed camera image analysis of jet.

Type	kV	Angle (°)	Straight Jet Length (mm)	Diameter of Jet (mm)
Needle	15	67.9	2.82	0.153
	16	62.8	3.01	0.175
	17	50.6	3.41	0.180
	18	47.2	3.77	0.186
	19	43.8	3.95	0.197
Flash	15	56.7	5.80	0.101
	16	50.4	5.99	0.106
	17	49.3	6.04	0.112
	18	45.9	6.47	0.114
	19	39.6	6.83	0.127
Protruded	15	61.3	4.95	0.112
	16	53.1	5.30	0.119
	17	49.7	5.39	0.120
	18	46.7	5.49	0.123
	19	40.1	5.75	0.125

According to the FEA simulations, electric field distribution can be manipulated by altering electrode geometry and varying applied voltage. More uniform electric field distribution is obtained along the z axis for flash and protruded electrodes. Increasing applied voltage results in more uniform electric field distribution. Longer and thicker

straight jet formation is observed when the electric field is relatively uniform. Similarly, the envelope angle is affected by the electric field. Uniform electric field results in narrow whipping motion.

4.4.3 Electrode Geometry Effect on Morphology, Diameter, and Alignment

Electrode geometry has a significant role on fiber diameter, morphology, and alignment. 50 μl of the solution is deposited, and optic and SEM images are taken. Figure 4.12 shows fiber mat deposited on 12 mm wide copper foil with (a) needle tip, (b) flash and (c) protruded electrodes. A relatively narrow fiber mat is found for nanofiber yarn deposited with flash and sputtered electrodes. Narrow whipping motion might be the origin of narrow nanofiber mats that are generated with flash and sputtered electrode.

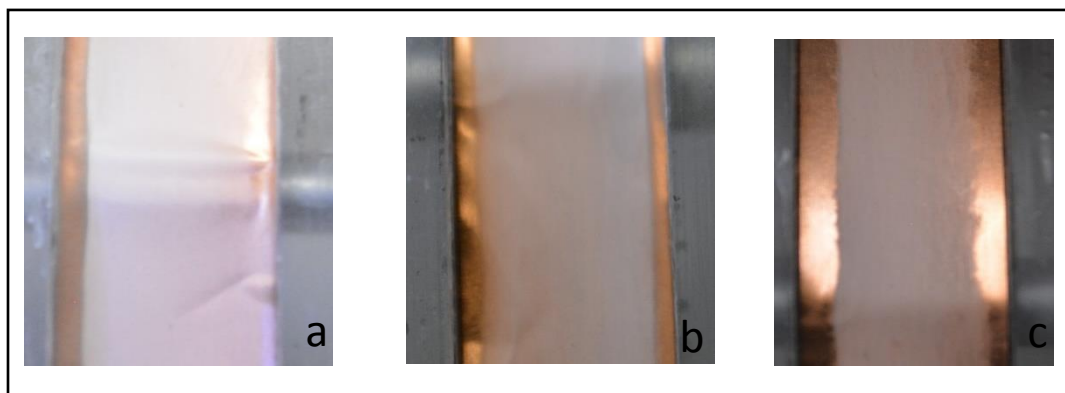


Figure 4.12 Fiber mat images deposited with (a) needle tip, (b) flash and (c) sputtered electrode (13 $\mu\text{l}/\text{min}$ flow rate, 15 kV, and 600 rpm)

Figure 4.13 shows SEM images of nanofibers fabricated with needle, flash, and protruded types of electrode. Nanofibers at this low magnification seem uniform and defect free. SEM images show that the electrode type influences fiber alignment remarkably. Average fiber diameter was determined by making 100 measurements of individual fiber diameters from the SEM images taken at different locations of the

nanofiber tows. Figure 4.14 is a relatively high magnification SEM image of nanofibers generated with (a) needle, (b) flash, and (c) protruded type of electrode. Flash and protruded electrodes causes slightly more uniform and thinner fibers compared to needle electrodes. Table 4.3 summarizes average fiber diameter and standard deviation of electrospun PAN nanofibers for different electrode types. Nanofibers experience a reduction in diameter depending on the electrode type. The protruded electrode shows the lowest average diameter and standard deviation.

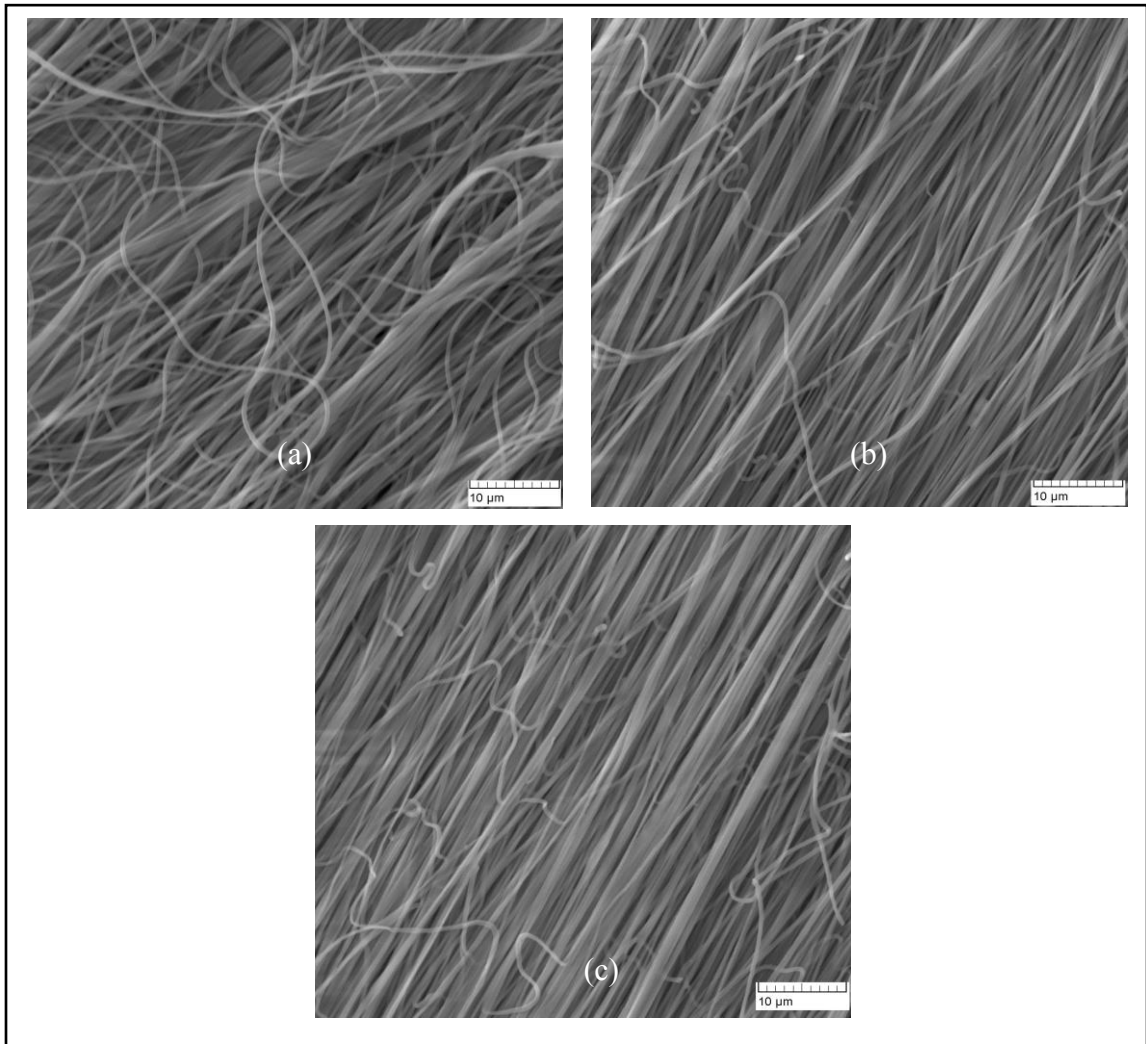


Figure 4.13 SEM images of PAN yarn fabricated with (a) needle, (b) flash, and (c) protruded type of electrode.

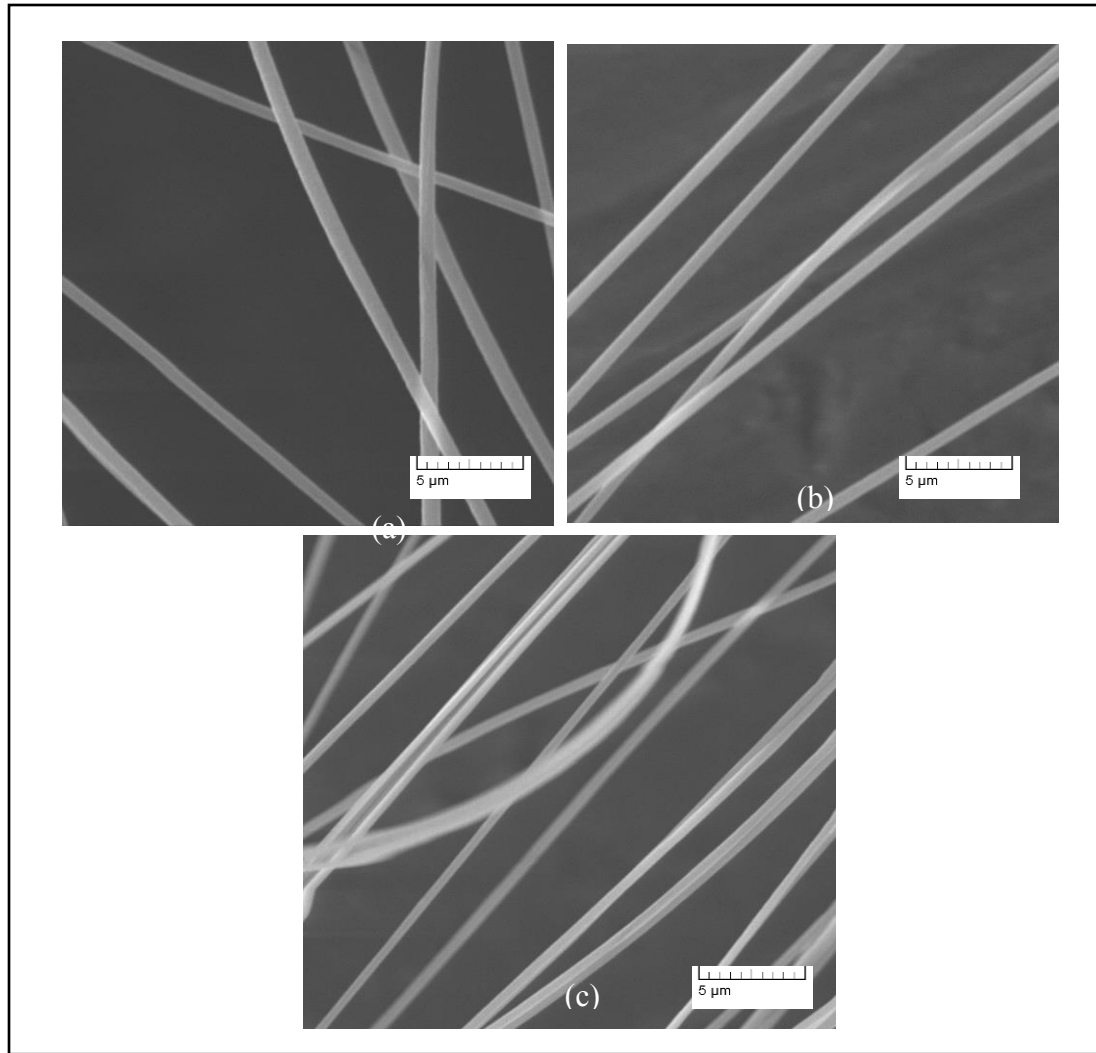


Figure 4.14 Morphology SEM images of PAN yarn fabricated with (a) needle, (b) flash, and (c) protruded type of electrode.

Table 4.3 also shows single fiber diameter and standard deviation. Fibers fabricated with flash and protruded electrodes show higher uniformity and smaller diameter. This can be explained with the FEA results. Fibers are exposed more uniform electric field through the z direction with flash and protruded electrodes. Fibers fabricated with the protruded electrode show slightly smaller diameter and more uniformity compared to flash electrodes. Taylor cone formation is also influenced by electrode shape. The high flat

surface on the flash electrode results in a wider Taylor cone. This affects fiber formation during electrospinning as well. Electrode type can manipulate fiber alignment. Flash and protruded electrodes result in better fiber alignment compared to the needle electrode due to exposure to less uniform electric field.

Table 4.3 Summary of average diameter for different needle tip and fiber alignment.

Geometry	Blind Needle	Flash	Protruded
Average Fiber Diameter on mat (nm)	422 ±48.1	401 ±38.5	389 ±35.9
Average Fiber Diameter along one single fiber (nm)	402 ±42.1	371 ±36.5	363 ±33.9
Average Fiber Angle (°)	14.3 ±12.3	8.9 ±5.6	7.6 ±4.9

4.4.4 Mechanical Properties

Mechanical properties of electrospun PAN nanofiber mats fabricated with needle, flash, and protruded electrodes are tested with the same method mentioned in sections 3.3.5 and 3.3.6. The electrospinning parameters include 600 rpm collector speed, 15 kV applied voltage, and 13 µl/min flow rate. Mechanical test results indicate that the electrode type influences mechanical properties. Figure 4.15 shows the stress-strain curve for nanofiber mats fabricated with needle, flash, and protruded electrodes. Tensile strength of PAN electrospun nanofiber mat is improved from 128 MPa to 148 MPa by employing the

protruded electrode compared to a traditional needle. Additionally, Young's modulus is slightly increased from 5.1 MPa to 5.8 MPa. Although tensile strength is high for the flash electrode compared to the needle electrode, they show the same Young's modulus of 5.1 MPa.

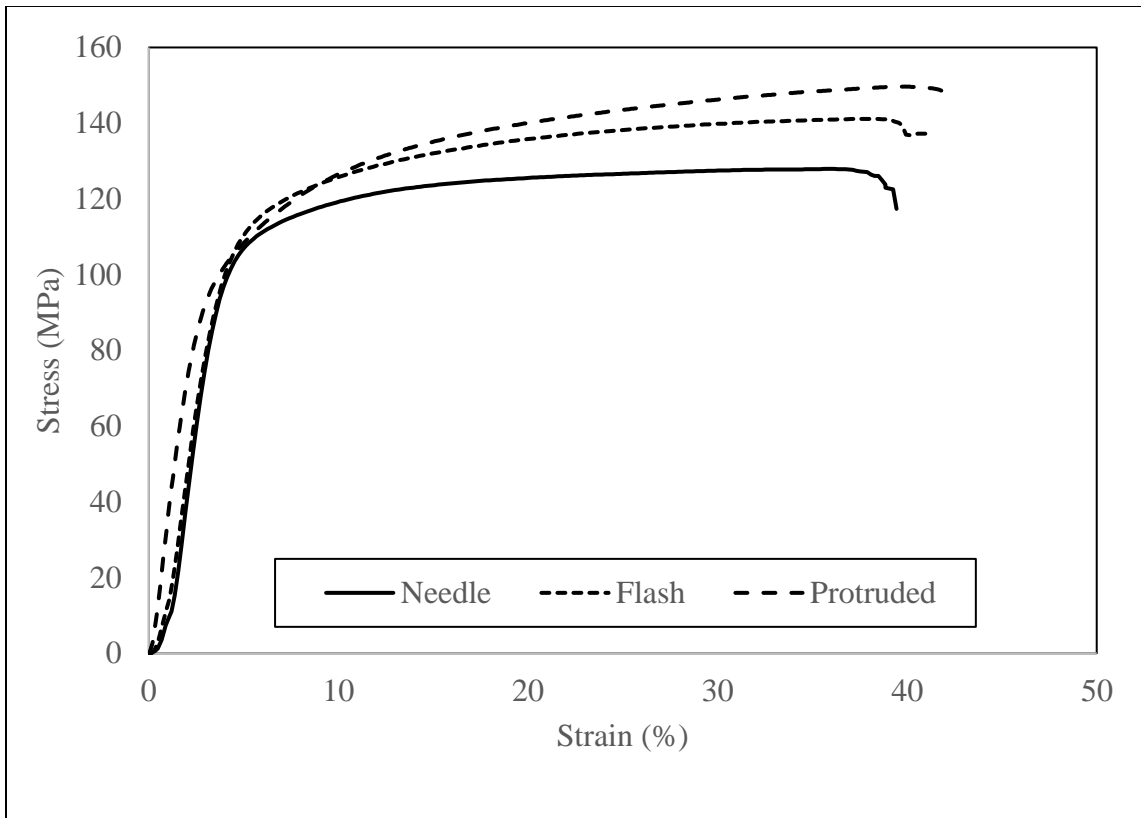


Figure 4.15 Stress-strain curve of electrospun PAN yarn fabricated with needle, flash, and protruded type of electrode (600 rpm collector speed, 15 kV applied voltage, 13 $\mu\text{l}/\text{min}$ flow rate).

4.5 Chapter Conclusions

Electrode type influences diameter, fiber alignment, and mechanical properties of PAN electrospun nanofibers. SEM and FEA results show that electrode type can influence

fiber diameter and alignment. FEA simulations indicate that electrode geometry alters electric field distribution. Flash and protruded electrodes result in a more uniform electric field distribution, while the needle electrode shows a sharp electric field change along the z direction. Flash and protruded electrodes cause more uniform electric fields, resulting in uniform fibers, smaller fiber diameters and better fiber alignment. The average fiber diameter is calculated to be 422 nm for needle electrodes, compared to 389 nm for protruded electrodes. Fiber alignment is improved with needle electrodes, resulting in a standard deviation of angle distribution of 16.1° , compared to 8.1° for the protruded electrode. In chapter 5, better fiber alignment and reduction of fiber diameter result in improved mechanical properties. Similarly, flash and protruded electrodes yield more uniform, aligned, and thinner diameter which result of enhanced mechanical properties.

Chapter 5 : STRETCHING AND PRE-STRESS CONDITION EFFECTS ON ELECTROSPUN POLYACRYLONITRILE AND STABILIZED NANOFIBERS

5.1 Introduction

Fabrication of CNT from electrospun PAN nanofibers requires a series of heat treatments such as stabilization and carbonization. Mechanical properties of ECNFs may vary depending on many factors, such as precursor properties, electrospinning process parameters, heat treatment conditions during stabilization and carbonization [133, 134], and applied tension. PAN is stabilized by controlled, relatively low temperature heating (200–300°C) in air to alter the precursor to a form that can be carbonized at high temperature without the melting or fusion of fibers [1]. During stabilization, the thermoplastic PAN is converted into a non-plastic cyclic compound that can endure high temperatures throughout the carbonization process [135]. Stabilization is a highly complicated process that consists of complex physical and chemical reaction mechanisms, like cyclization, oxidation, dehydrogenation, and cross-linking reactions [135–139].

Cyclization is an important reaction that converts nitrile groups into carbon-nitrogen double bonds of stabilized, nitrile groups [140]. The cyclization reaction is shown in Figure 5.1. The formation of a ladder structure results in a stable structure at high temperatures, and improves carbon yield during carbonization. Color changes have been observed from white to yellow, brown, dark brown and finally to black [141].

When the stabilization of PAN fibers is done in an oxidative atmosphere, oxidation occurs; this is an exothermic reaction. Thermally, more stable structures are obtained by oxidation. Dehydrogenation causes the formation of carbon-carbon double bonds (-C=C-) and

conjugated structures in PAN molecules (Figure 5.1). The thermal stability is improved by the formation of C=C double bonds.

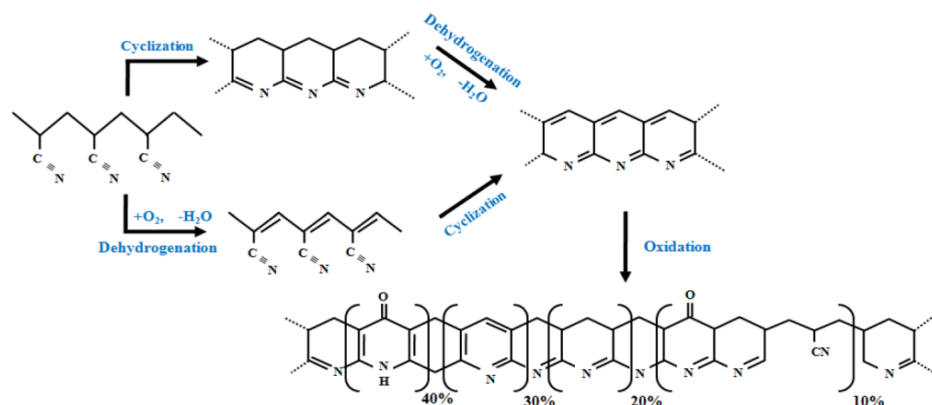


Figure 5.1 Schematic explanation of the chemical reaction during stabilization of PAN fiber [142].

In chapters 3 and 4, process parameters such as collector speed, collector geometry, and electrode type were shown to decrease fiber diameter and increase alignment. The results show that better fiber alignment yields higher mechanical properties. Even though fiber alignment can be improved by electrospinning itself, the PAN contains highly polar nitrile groups that leads to misalignment of macromolecular chains [143]. However, after spinning, stretching helps to enhance molecular level alignment and tensile properties. Chen and Harrison [144] reported a 53% improvement on tensile strength by stretching. Song et al. [145] reported enhanced mechanical properties and crystallinity by hot-stretching. Stretching influences the stabilization process; relaxation during stabilization is remarkably reduced [146]. Constant load during stabilization influences mechanical properties. Yun et al. [135] applied a constant load to macro PAN fibers during stabilization. 15 mg/filament yielded maximum tensile strength. In this chapter, stretching effects on mechanical properties of PAN electrospun nanofibers and crystallinity are

investigated. Furthermore, the effects of pre-loading in the range of 0-5 MPa on stabilization kinetics are studied by employing in-situ characterization approaches.

5.2 Experimental

5.2.1 Hot Stretching

The solution is prepared by following the procedures at section 2.5.1 and electrospinning is performed using the same procedure found in section 3.3.1 using a foil type collector at 1500 rpm. After drying on a drying rack at 60°C for 5 hours in a vacuum oven, the yarns are stretched at a 5 mm/min strain rate in an environmental chamber equipped Instron 5969 Column Testing Machine. PAN is a polymer that tends to decompose before melting. The stretching temperature must be below PAN's decomposing temperature, but high enough to soften the material. It has been reported that 135°C is a favorable temperature for stretching [145, 147], thus this is the selected stretching temperature. Nanofiber yarns are mounted with a high temperature resistant Teflon type on an aluminum plate 1 " wide and 2 " long. This allows enough grip to prevent sliding during the stretching process (Figure 5.2).



Figure 5.2 Fiber stretching process (5 mm/min strain rate and in 135°C Instron 5969 environmental chamber).

Stretching is measured with a DMA Q800. The samples are mounted on the tensile fixture and the same stretching procedure is followed. Figure 5.3 shows the stress-strain curve, with drawn stretch ratios of $\lambda=1$, 2, and 3. All yarns survived throughout stretching process.

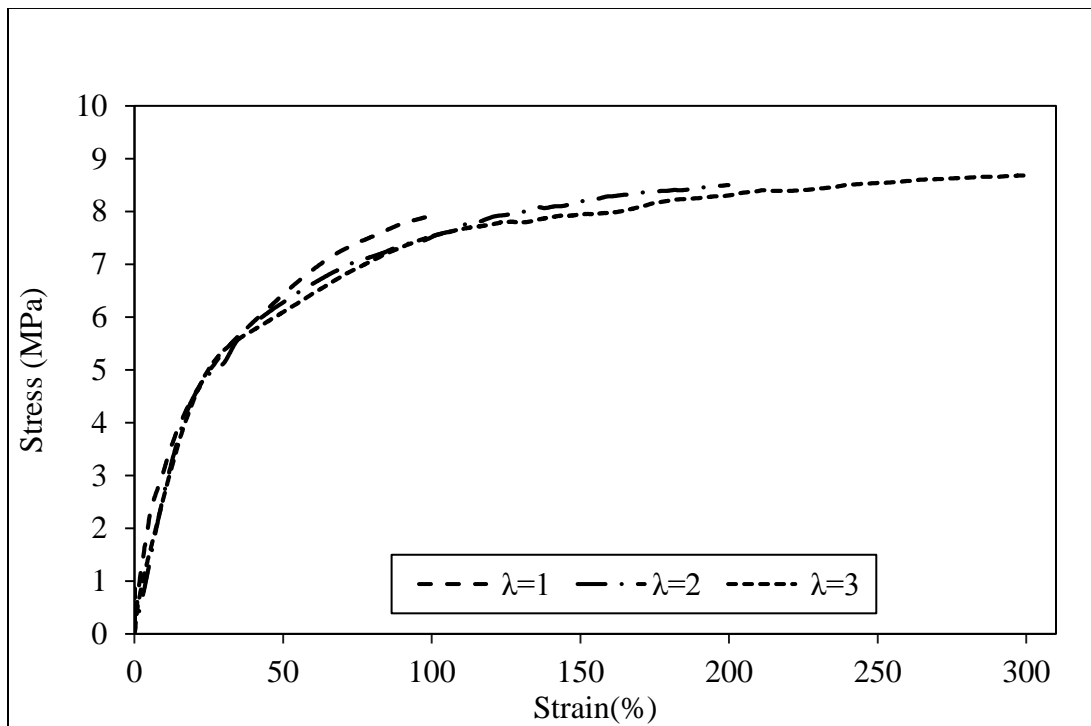


Figure 5.3 Stress-Strain curve of PAN electrospun fiber during stretching at 135°C.

5.2.2 Stabilization by Applying Pre-Stress

A programmable air convection oven (Model 825, Cole-Parmer) is employed for stabilization. A calculated weight corresponding to the stress is attached to one end of the fiber, and the other end is fixed with high temperature resistant Teflon tape so that the

fibers are hanging (Figure 5.4). The yarns were heated in the oven with a 5 °C/min ramp from room temperature to 260°C for 180 min.

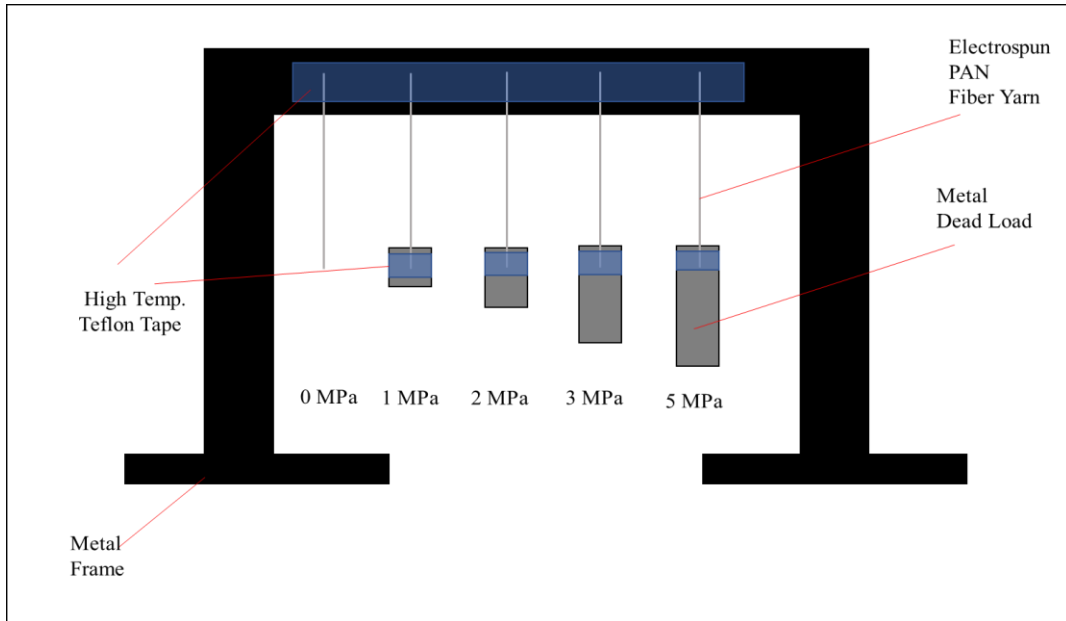


Figure 5.4 Illustration of stabilization under pre-stresses conditions. Dead loads are hanged on fiber depending on corresponding stresses.

5.2.3 In situ Characterization

A differential scanning calorimetry (DSC Q-50, TA Instruments) is employed to measure heat flow as function of temperature. Weight loss during stabilization is measured with a thermo-gravimetric analyzer (TGA Q-500, TA Instruments). Both DSC Q-50 and TGA Q-500 can operate with inert gases, such as N₂. In-situ stabilization shrinkage and dynamic mechanical properties were monitored by a dynamic mechanical analyzer (DMA Q-800, TA Instruments). A small amount of load 0.5 MPa was applied during shrinkage.

5.2.4 Powder X-ray Diffraction (XRD) Characterization

Powder X-ray diffraction (XRD) analysis is performed in the School of Geology and Geophysics at the University of Oklahoma using a Rigaku Ultima IV diffractometer. Cu-K-alpha radiation (40 kV, 44 mA) is used with a D/teX silicon strip detector. All samples are initially mounted on glass sample holders. The sample itself is held on the sample holder using Vaseline. The scans are performed at $2\theta=2-50^\circ$. XRD crystallinity is obtained by dividing the area under the crystalline peaks by the total area under the curve [142]:

$$\%crystallinity = \frac{A_{c1}}{A_{c1} + A_a} \quad (5.1)$$

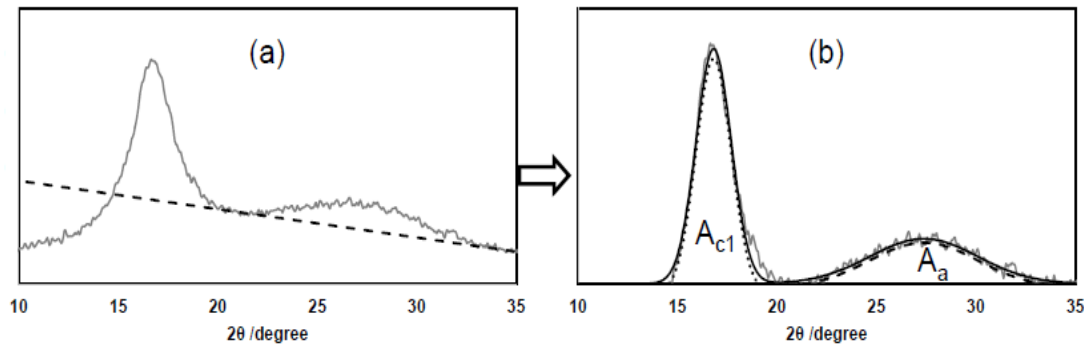


Figure 5.5 Calculation method of the crystallinity from XRD data (a) baseline to determine pikes (b) pike area [142].

5.3 Results and Discussion

5.3.1 Hot Stretching Effects on Fiber Diameter of Electrospun PAN Nanofibers

Figure 5.6 shows SEM images of electrospun PAN nanofibers stretched at different ratios ($\lambda=1$ to 3). Nanofibers at this low magnification seem uniform and defect free. SEM images show that stretching increases fiber alignment remarkably. The average fiber

diameter is determined by making 100 measurements of individual fiber diameters from the SEM images taken at different locations of the nanofiber tows. Table 5.1 summarizes average fiber diameter and standard deviation of electrospun nanofibers and stabilized nanofibers for different stretch ratios. As-spun nanofibers experience a reduction in diameter during the heat treatment, experiencing an average diameter decrease of more than twice that of the unstretched sample. The effects of pre-loading during stabilization on fiber diameter is not significant for stretched fibers. However, unstretched as-spun fibers experienced shrinkage during stabilization under a constant load. This reduction may be related to relaxation effects during stabilization [146].

Stretching also enhances uniformity of the nanofiber. Standard deviation of fiber diameter is derived to be 54 nm for unstretched nanofibers. However, it is reduced to 34 nm for $\lambda=3$ compared to the unstretched fiber diameter.

Table 5.1 Average diameter in nanometers of electrospun, stabilized nanofibers respect to stretching ratio.

Stretching Ratio	PAN Nanofibers (nm)	Stabilized Under Constant Load (nm)				
		0 MPa	1 MPa	2 MPa	3 MPa	5 MPa
$\lambda=0$	272±54	260±55	256±51	245±49	248±47	239±40
$\lambda=1$	188±48	180±40	176±42	167±48	160±43	163±40
$\lambda=2$	158±38	145±37	141±34	138±38	133±37	139±39
$\lambda=3$	135±34	132±39	128±34	130±36	126±30	125±38

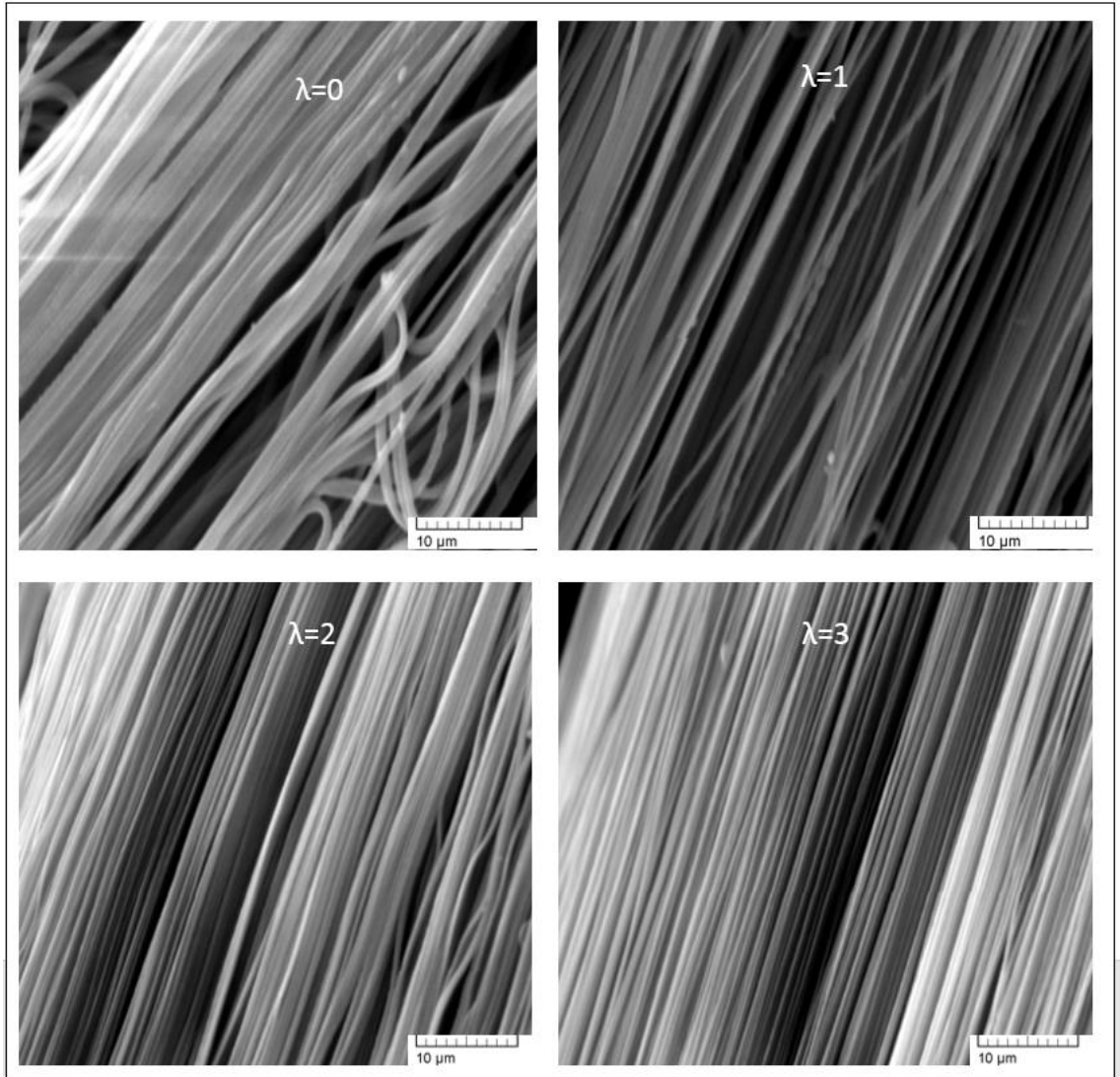


Figure 5.6 SEM images of electrospun PAN nanofibers with stretching ratios, $\lambda=0$, 1, 2, and 3.

5.3.2 Tensile Properties of Stretched PAN Nanofibers

Figure 5.7 shows tensile test results of electrospun unstretched PAN nanofiber yarn and stretched yarn ($\lambda=1$ to 3). Stretching enhances mechanical properties of PAN electrospun nanofibers significantly. Among, the fibers stretched, those stretched to $\lambda=2$ exhibit the best tensile properties. Unstretched nanofiber yarn showed a tensile strengths

162 MPa, while fibers stretched 2 times their length exhibit a tensile strength of 276 MPa. Additionally, Young's modulus increases from 5.1 MPa to 6.2 MPa by stretching to $\lambda=2$. Stretching induces improvement in mechanical properties by increasing macromolecular orientation [144]. When the stretching ratio is $\lambda=3$, mechanical properties tend to reduce compared to $\lambda=2$. This phenomenon could be related to the exceed molecular level orientation and could be introducing more defects in the fibers.

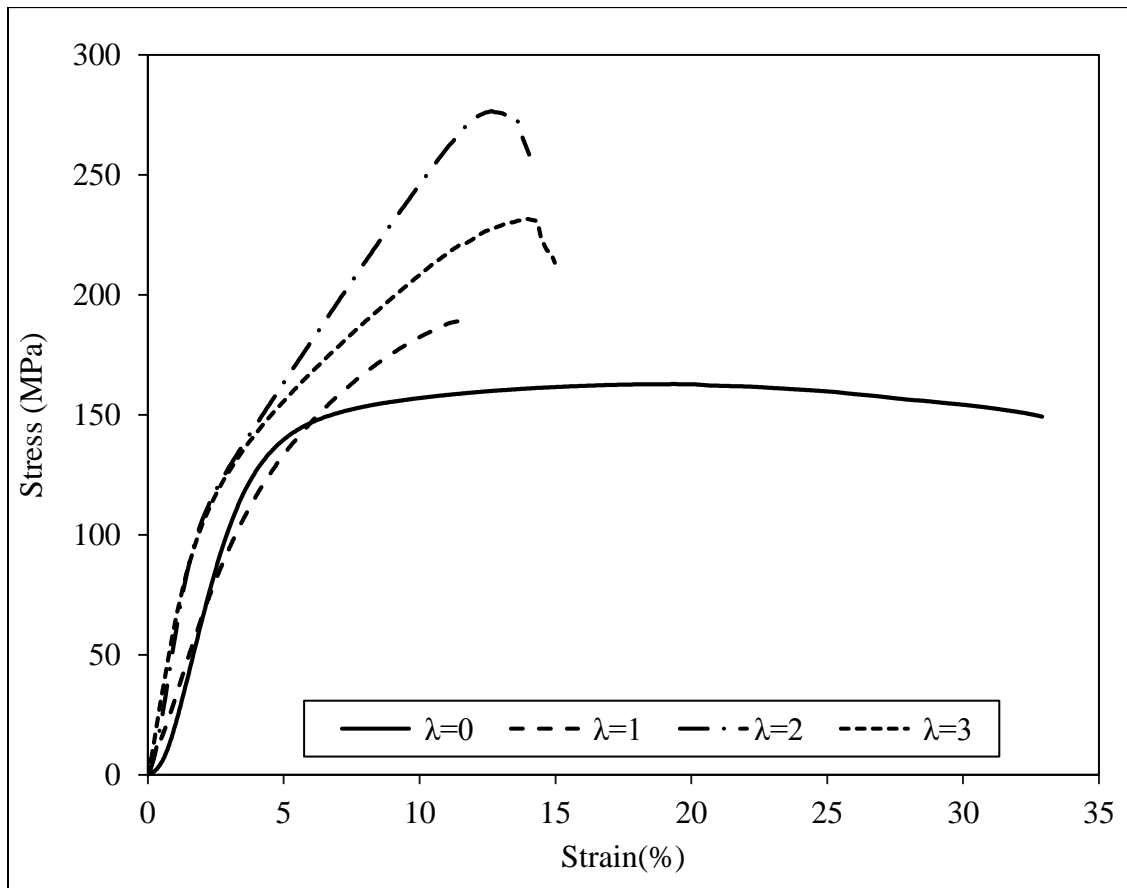


Figure 5.7 Tensile test results of PAN nanofiber at different stretching ratios.

5.3.3 Crystallinity Analysis

Powder X-ray diffraction (XRD) analysis is performed to investigate the crystallinity of the PAN nanofibers. The X-ray diffraction patterns, along with calculated fractional crystallinity, are shown in Table 5.2. Stretching PAN nanofibers at 135 °C increases crystallinity significantly. The highest improvement is obtained when the stretch ratio is 2. However, no improvement is obtained for a stretch ratio greater than 2. Higher stretch ratios exceed stretchable limits. Some polymer chains might experience breakage due to exceeded stretching. Thus, mechanical properties are low for $\lambda=3$ when comparing to $\lambda=2$. Ravandi et. al [148] investigated hot stretching effects on PAN electrospun nanofibers. They observed improvement of mechanical properties by increasing hot drawing ratio. However, no improvement on mechanical properties is obtained when the ratio is 3 or greater. Figure 5.8 shows XRD pattern of unstretched and stretched PAN electrospun nanofibers. The intensity peak is found at $2\theta=17.8^\circ$ and the peak becomes sharper by increasing the stretch ratio.

Table 5.2 Crystallinity calculation results based on powder XRD of PAN nanofibers at different stretched ratio and unstretched.

Stretch Ration (λ)	Crystallinity
0	%52.54
1	%63.22
2	%70.29
3	%60.34

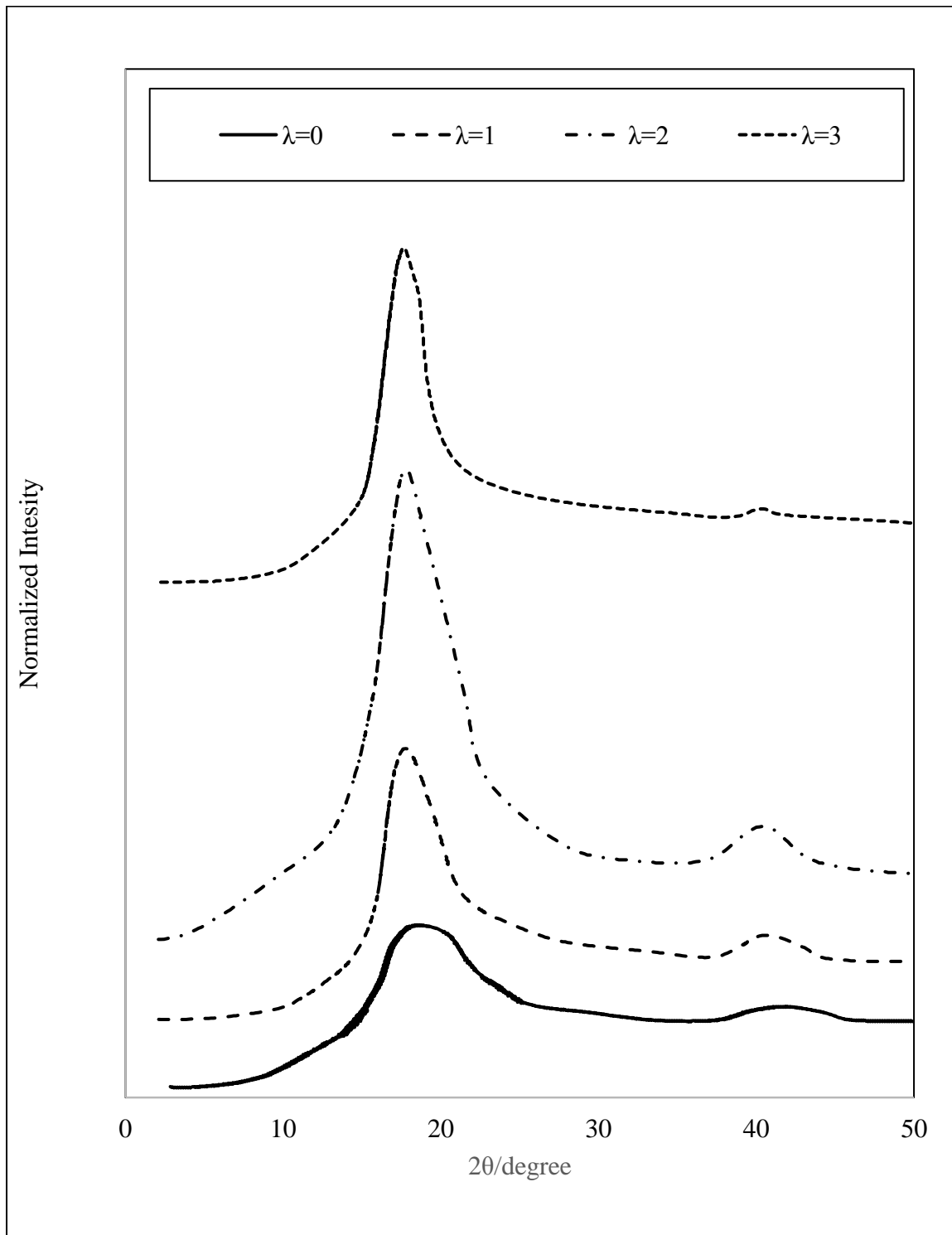


Figure 5.8 XRD pattern of PAN nanofiber yarn at different stretching ratio.

5.3.4 Investigation of Stretching Effect on Stabilization Reaction

The DSC is a beneficial instrument that provides useful information about chemical reactions, such as dehydration and intra- and intermolecular cyclizations. Figure 5.9 shows the thermal behavior of the unstretched and stretched PAN electrospun fibers in a nitrogen atmosphere. Figure 5.10 is the plot of same experiment in air. Two distinct exothermic peaks are observed at 245 °C and 370 °C in the air atmosphere. However, only a single exothermic peak is obtained at 260 °C in the nitrogen atmosphere. Yun et al. [135] reported that Peak I occurs because of the intramolecular cyclization/thermal stabilization reactions, and Peak II appears due to dehydration, which requires oxygen molecules in the atmosphere. Dehydration also leads to intermolecular cross-linking [149].

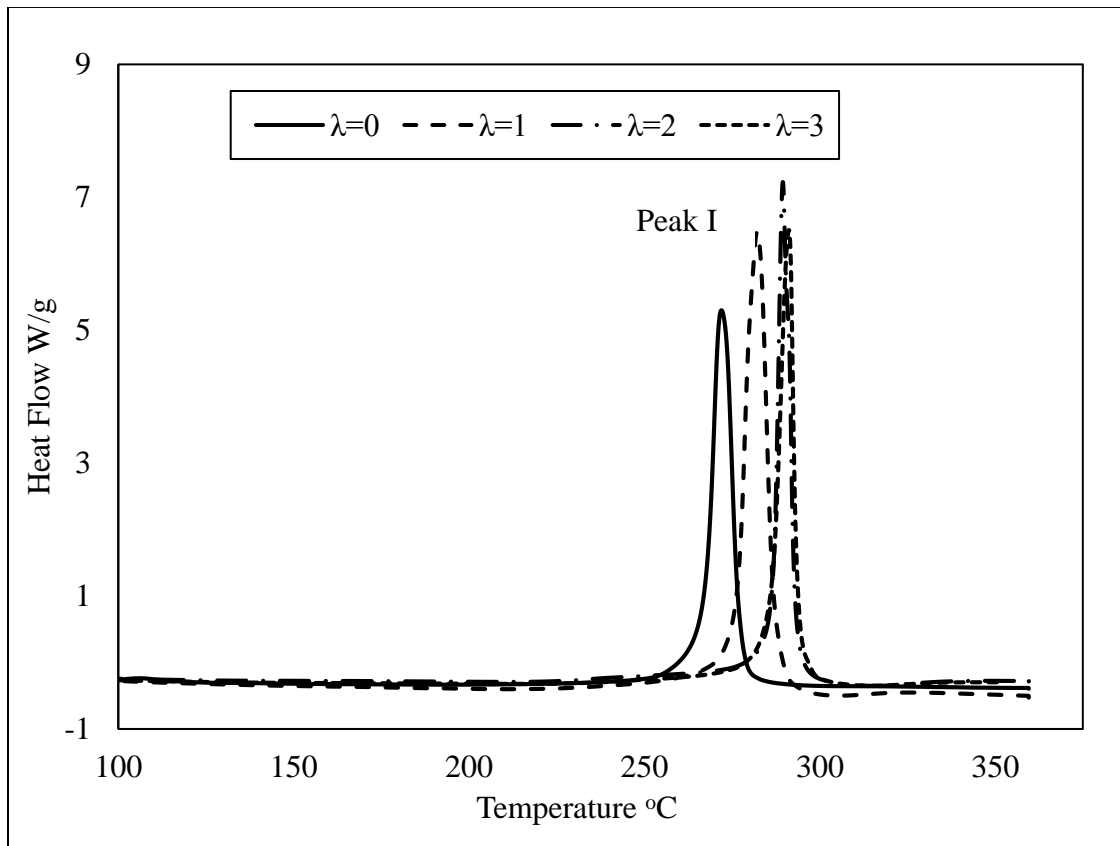


Figure 5.9 DSC plots of PAN electrospun nanofiber in nitrogen heating at 5 °C/min.

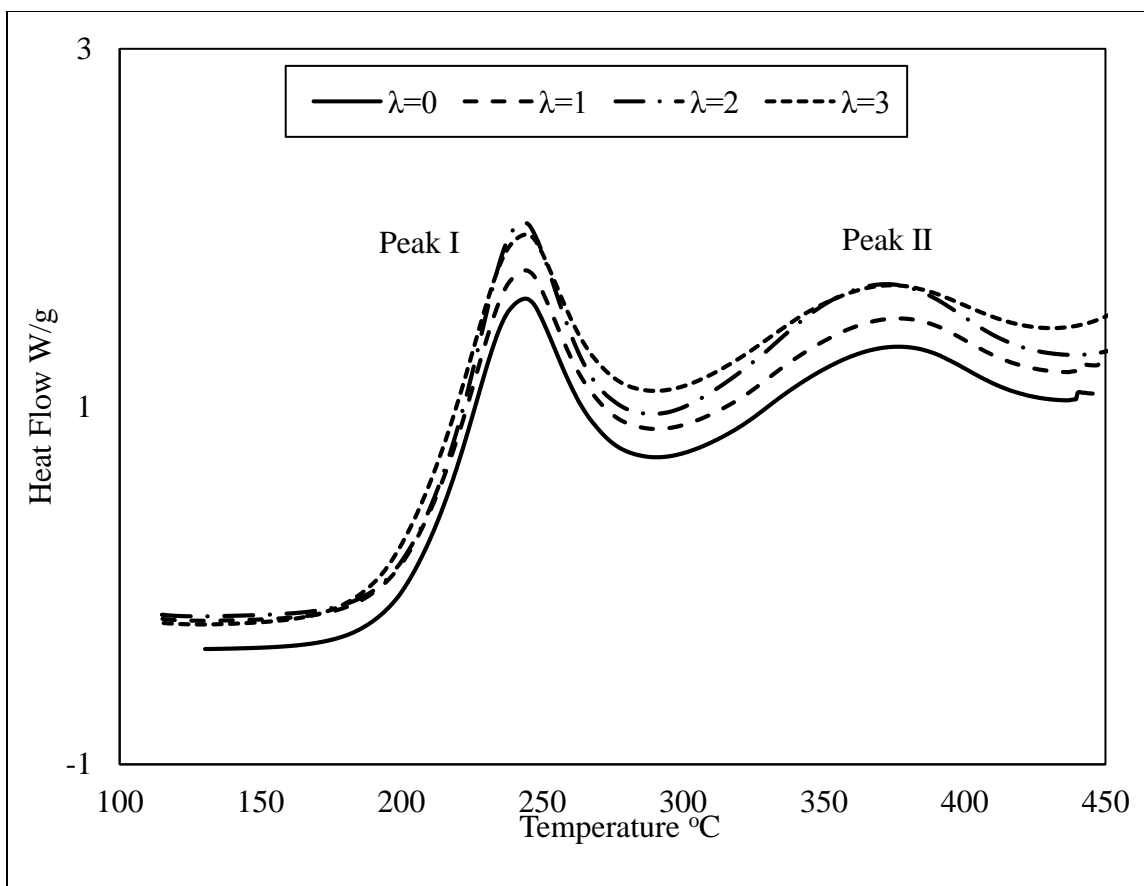


Figure 5.10 DSC plots of PAN electrospun nanofiber in air heating at 5 °C/min.

Thermal behavior of electrospun PAN nanofibers vary depending on stretch ratio. Peak I in the nitrogen atmosphere is shifted slightly and becomes sharper by increasing the stretch ratio. Table 5.3 shows the amount of energy released during exothermic intramolecular cyclization as a function of stretch ratios. The highest cyclization heat is obtained for a stretch ratio 2. According to the XRD results, crystallinity increases up until $\lambda=2$. In the Peak I temperature region, rigid crystalline structures are destroyed because the cyclization reaction extends into the crystalline regions in nitrogen. At lower temperatures, cyclization starts at the amorphous region [150]. This phenomenon explains the peak shift and increase in cyclization heat due to an increase on crystallinity.

Table 5.3 Cyclization peak temperature and cyclization heat derived by calculating the area under the curve from DSC result in nitrogen for PAN electrospun nanofiber stretched and unstretched.

Stretch Ration (λ)	Cyclization Temperatures ($^{\circ}\text{C}$)	Heats of Cyclization (J/g)
0	272.00	429.067
1	282.19	509.086
2	289.20	522.684
3	292.46	513.85

TGA analysis is performed to measure the thermal stability of unstretched and stretched PAN electrospun nanofibers. Figure 5. 11 shows the derivative of weight loss in percentage as a function of temperature. This plot helps show the temperature range weight loss. According to the TGA analysis, the peak is obtained at higher temperatures for high stretching temperature.

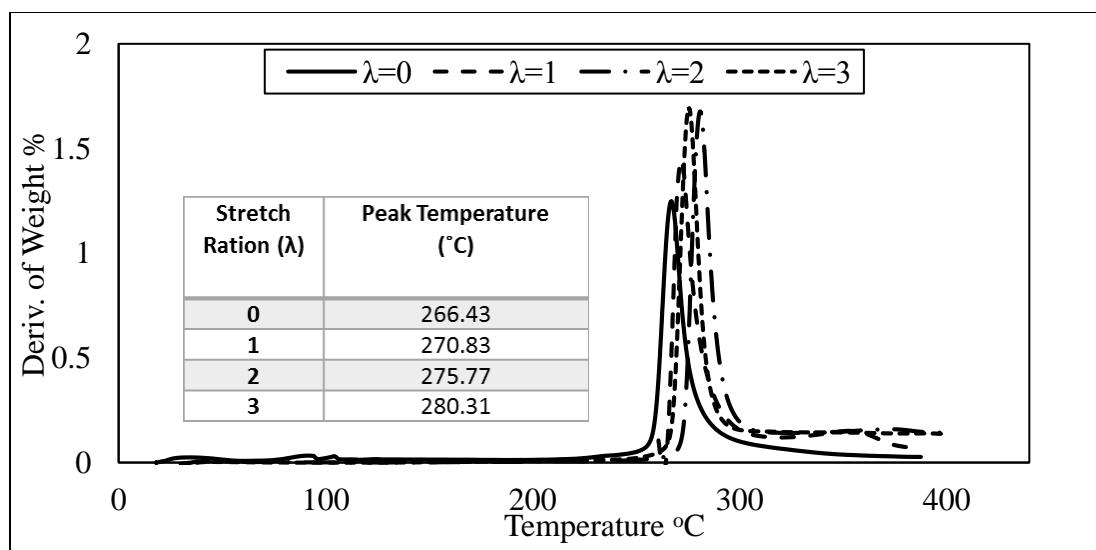


Figure 5.11 Derivative of TGA plot in nitrogen for electrospun PAN stretched and unstretched nanofibers.

Warner et al. [151] observed that during stabilization, initial tension developed due to the entropic recovery and a relaxation down to initial stress. Then, a slow stress increase occurred. Controlling tension during stabilization is important to prevent fiber expansion or possible breaking if the tension is too high. Barua and Saha [112] optimized stabilization conditions for electrospun PAN nanofibers. The optimum conditions specify heating at 5 °C/min ramp until a temperature of 260 °C, and 180 min isothermal at 260 °C. In this study, these conditions are applied to investigate constant loading effects during stabilization.

DMA is employed to investigate shrinkage behavior under tension during stabilization. Unstretched PAN electrospun nanofibers are affected by tension. Figure 5.12 shows low tension nanofibers experienced high stress relaxation at low temperature. The relaxation, which yields poor molecular orientation during the stabilization steps can be reduced by applying tension. Additionally, two different shrinkage mechanisms are observed; physical shrinkage (recovery of the drawn and quenched material), and chemical shrinkage (nitrile cyclization reactions resulting in formation of ladder polymer) [135]. Figure 5.13 indicates the different behavior of unstretched and stretched fibers under tension during stabilization. It is difficult to distinguish physical shrinkage for unstretched samples due to stress relaxation. Stretched PAN nanofibers with $\lambda=3$ experience the least physical shrinkage. However, stretched PAN nanofibers do not experience stress relaxation during stabilization. Chemical shrinkage initiates at 168 °C and is independent of constant loading during stabilization. The amount of chemical shrinkage varies from a minimum 10% to a maximum of 30%, depending on the ratio of intermolecular to intramolecular cyclization reactions [152]. Shrinkage decreases molecular alignment in the fibers and weakens the mechanical properties of the carbon fibers. Hence, the shrinkage must be

minimized in developing highly ordered and flawless carbonized fibers [135, 153]. However, high tensions during stabilization may cause breakage of fibers. Unstretched PAN nanofibers show 29% shrinkage without tension during stabilization, with total shrinkage reducing to 23% when a 5 MPa tension load is applied during stabilization (Figure 5.14). However, stretched nanofibers show significantly less shrinkage compared to unstretched fibers. Total shrinkage is reduced to 17% by increasing tension. Additionally, Figure 5.15 plots the temperature range at which cyclization reaction starts. Cyclization starts at 170 °C for unstretched PAN nanofibers, with a shifting peak shifts at increased stretch ratio. The DSC plot (Figure 5.10) in air indicates that intramolecular cyclization occurs more for stretched PAN nanofibers compared to unstretched fibers. Stretched nanofibers experience less shrinkage due to a high intramolecular cyclization ratio. Shrinkage can be reduced via two mechanisms to increase molecular orientation: pre-stretching before stabilization and increasing tension.

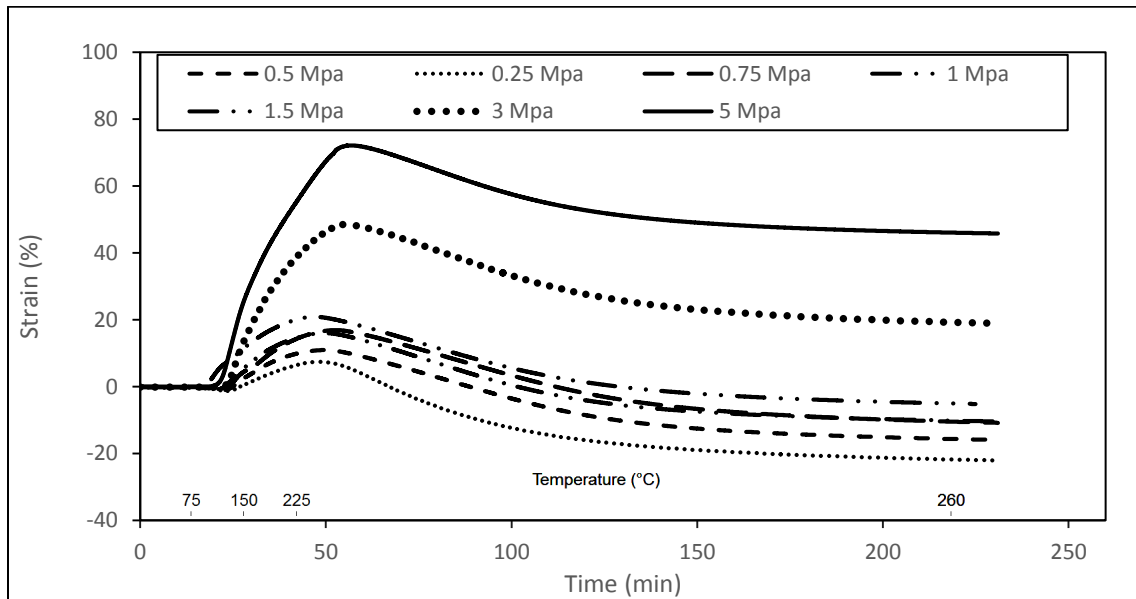


Figure 5.12 PAN unstretched electrospun nanofiber shrinkage behavior during stabilization at different constant loads (5 °C/min ramp, 180 min isothermal at 260 °C).

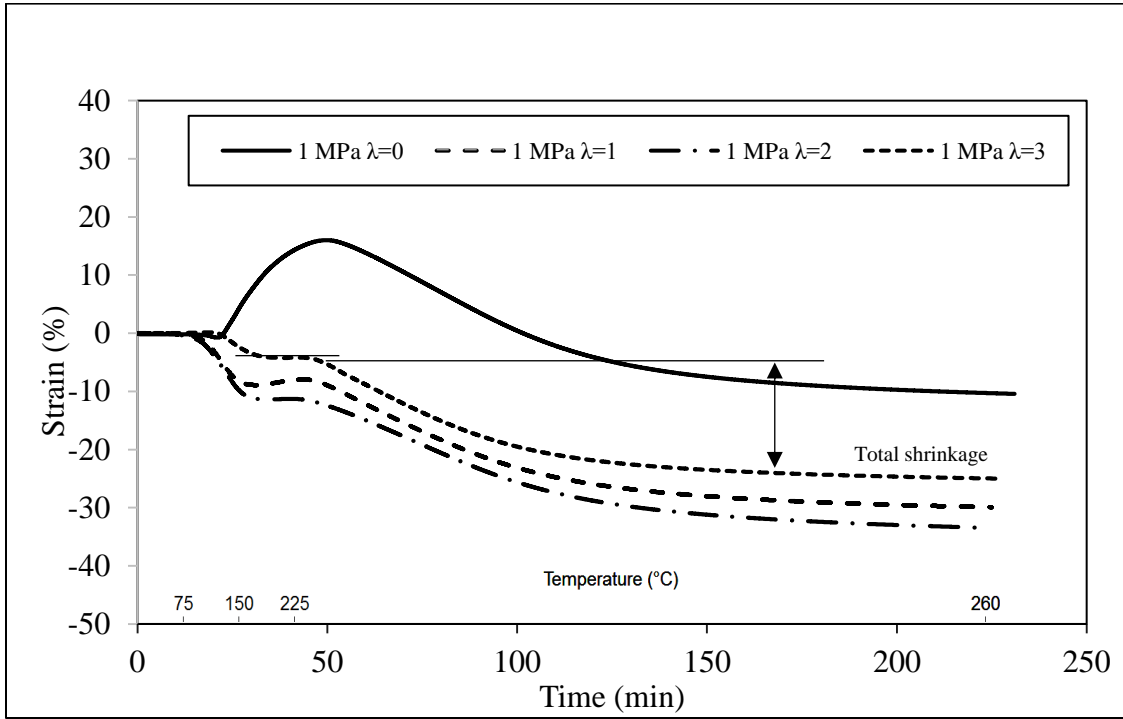


Figure 5.13 PAN unstretched and stretched electrospun nanofiber shrinkage behavior during stabilization under 1 MPa tension (5 °C/min ramp, 180 min isothermal at 260 °C).

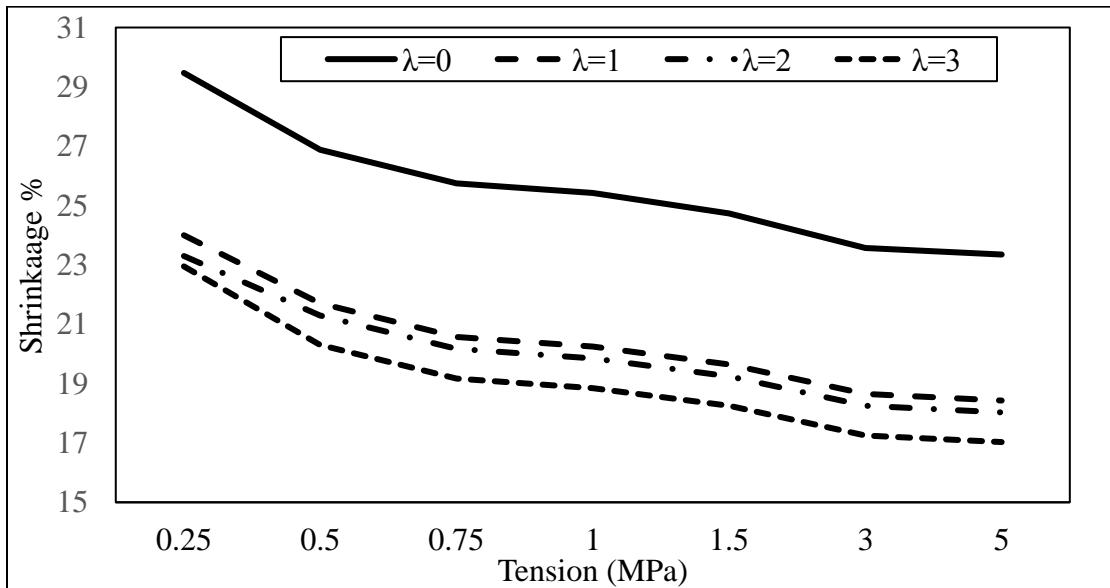


Figure 5.14 Amount of shrinkage as a function of tension during stabilization for unstretched and stretched PAN electrospun nanofibers.

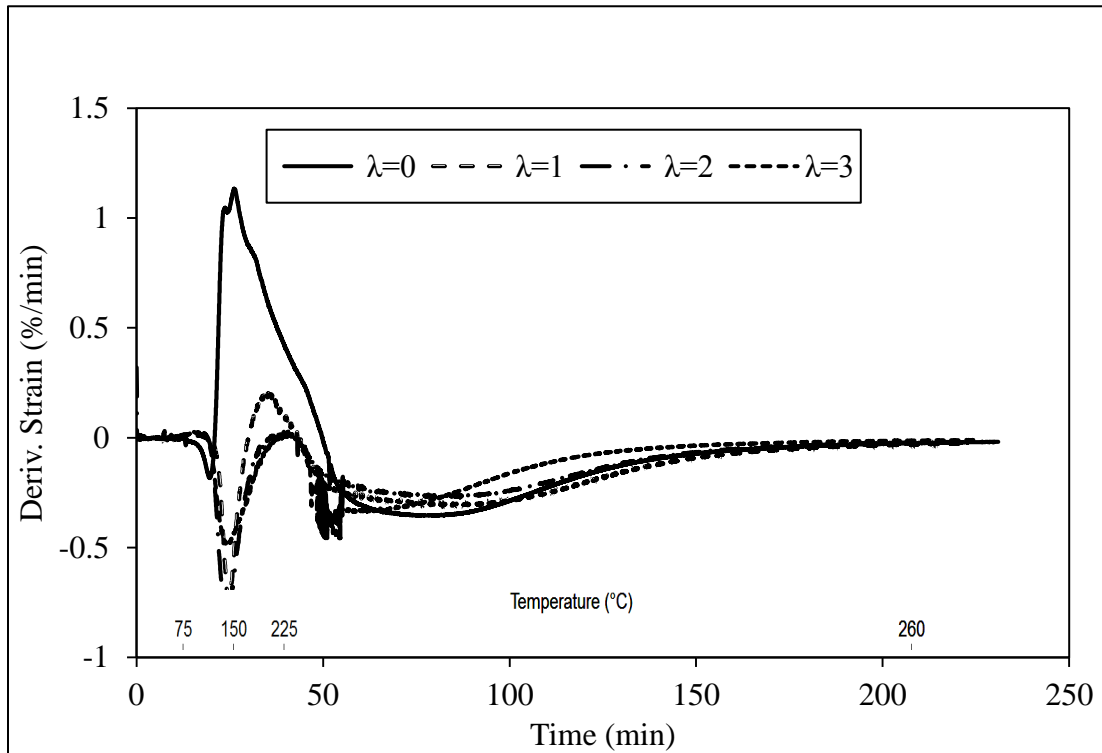


Figure 5.15 DMA in situ stabilization strain derivative of time constant load 1 MPa

5.3.5 Pre-Loading Effects on Mechanical Properties

Table 5.4 summarizes the tensile properties of stabilized nanofiber yarns at different stretching ratios and constant loads during stabilization. All nanofiber yarns stretched to $\lambda=2$ exhibit the highest tensile properties for the corresponding stabilization load. Constant load during stabilization improves tensile properties significantly. Stretching at 1 MPa shows the maximum mechanical properties if all stretch ratios. Yun et al reported that after a certain point of loading, defects in fibers increase [135]. Stabilized fibers stretched to $\lambda=3$ show lower tensile strength and modulus compared to those stretched to $\lambda=2$. Defects introduced while overstretching might be the reason for the reduction in tensile properties.

Table 5.4 Summary of tensile test results of stabilized nanofibers.

Stretching Ratio	Stab. Constant Load (MPa)	Tensile strength (MPa)	Tensile modulus (GPa)	Failure Strain (%)
$\lambda=0$	0	56	3.5	7.58
	1	191	10.9	3.45
	2	186	9.5	3.35
	3	176	9.7	2.90
	5	149	7.8	2.50
$\lambda=1$	0	175	9.6	3.70
	1	279	16.8	2.74
	3	245	14.2	2.55
	5	201	10.9	2.10
$\lambda=2$	0	212	15.3	3.62
	1	401	26.7	2.77
	2	375	22.4	2.44
	3	353	19.3	2.33
	5	225	17.0	1.78
$\lambda=3$	0	201	14.8	3.44
	1	384	23.9	2.69
	2	365	19.3	2.22
	3	301	17.6	1.77
	5	198	14.5	1.53

5.4 Chapter Conclusions

Stretching and tension during stabilization play an important role on fiber diameter and tensile properties of electrospun PAN and stabilized nanofibers. Stretching reduced average fiber diameter and increased crystallinity significantly. Average as-spun fiber diameter is found to be 272 nm, while those stretched to $\lambda=3$ showed an average diameter of about 135 nm. While stretching decreases electrospun PAN nanofiber diameter, pre-

loading during stabilization does not affect fiber diameter noticeably. Moreover, stretching influences mechanical properties of as-spun and stabilized nanofiber yarns. Unstretched fibers show lower mechanical properties. Lower macromolecular orientation is believed to be a possible reason for the lower mechanical properties of unstretched nanofiber yarns. The highest tensile strength was observed by fibers stretched to $\lambda=2$ produced at with stabilization pre-stress of 1 MPa, with a value of 401 MPa, while unstretched fibers showed a tensile strength of 191 MPa .

Chapter 6 : SINGLE FIBER STRENGTH CALCULATION FROM BUNDLE TEST

6.1 Introduction

Failure strength of unidirectional composites is correlated with the mechanical behavior of the fiber. Tensile strength of fibers is usually determined by testing a minimum of 20 single fibers or a bundle of fibers [154]. Researchers developed a procedure in order to determine average strength of fiber from the strength measurement of a group of fibers with the same length. The Weibull parameters are calculated from average strength and gauge length [155].

The tensile strength of fibers has been investigated for a few decades by several study groups. The test method of tensile strength and Young's modulus of single filament fibers is issued by American Society for Testing and Materials (ASTM) in ASTM D 3379 [156]. High modulus single filament fibers (higher than 21 GPa) are covered. Figure 6.1 shows a schematic of alignment of a fiber on cardboard. First, an individual fiber is randomly drawn from the bundle without damaging. Second, the individual fiber is mounted on the carton window on the alignment line. The fiber must be well aligned in order to obtain accurate results. Finally, both ends are glued with a compatible glue. The specimen is ready for the testing. When the carton board is gripped, the carton window sides are cut.

Later, ASTM issued other standards enlarging the coverage of previous standards because of higher variety of fibers. ASTM D3822-07 is the newest standard of tensile test method of single filament tensile test [157].

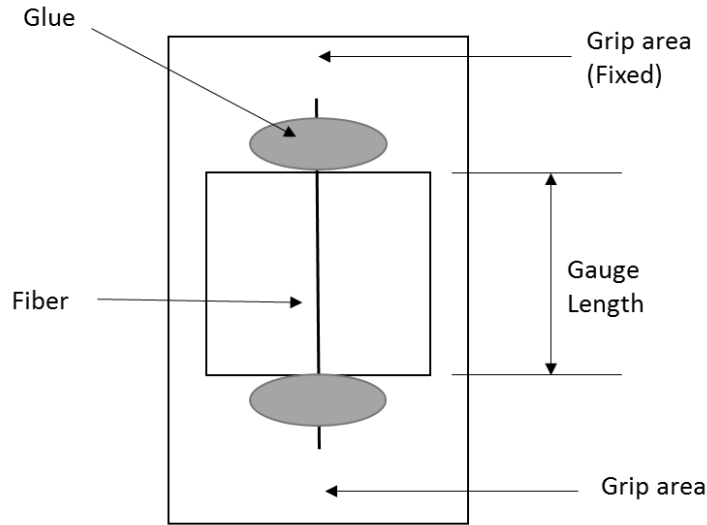


Figure 6.1 Schematic showing of tensile test fixture and mounting of single filament fibers.

ASTM D7846 contains the analysis of uniaxial strength data and probability parameters for advanced graphites. The Weibull probability distribution method is used to analyze tensile strength of advanced graphites. Two parameters of the Weibull model are recommended for advanced graphites in ASTM D7846 [158]. For fiber bundle tests, ASTM has published test standards for cotton fibers or other textile products [157], [159]. Those standards do not cover brittle fibers, such as carbon fibers. Therefore, study groups have been developed a different fixture depending on their test equipment.

Single fiber tests are possible today. Some tensile test instruments equipped with a high resolution load cell are capable of testing micro fibers. However, there are several problems with single fiber test methods. Chi et al. [160] mention some of these. First, drawing a single fiber and mounting it on window frame process is extremely hard and time consuming. Second, the selected fiber are mostly the stronger ones due to the fact that

weaker fibers tend to damage and fracture during the process. Third, determining the exact diameter of the fiber is difficult. Yao and Yu [161] investigated the effects of the pretension and nonaxial stretching on test results. They reported that misalignment causes 2.5% strain error; nonaxial stretching does not cause significant error up to 4%. Figure 6.2 shows the misalignment.

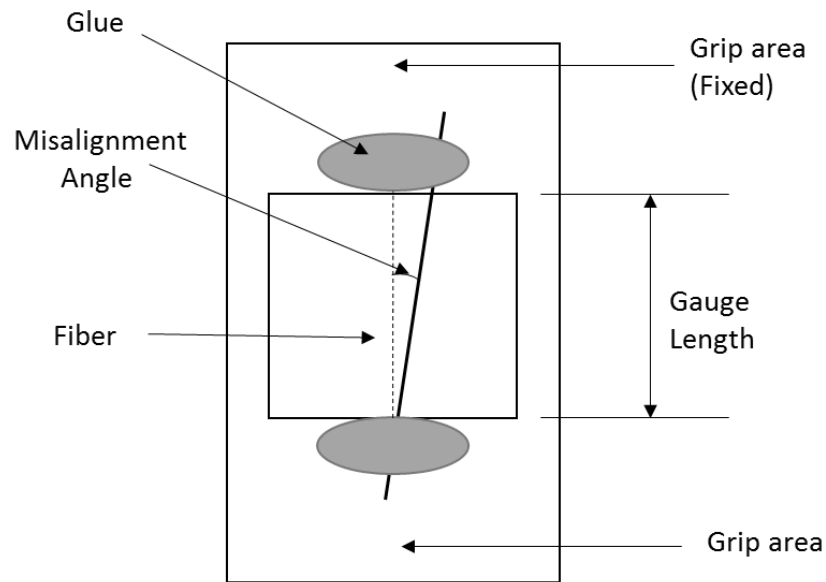


Figure 6.2 Misalignment of single fiber mounting on window frame.

6.2 Statistical Carbon Fiber (CF) Strength Analysis

6.2.1 Weibull Distribution

Cumulative probability distribution functions are generally used to determine the strength of brittle materials. Even though sample geometry and micro structures are similar, different values of strength can be obtained for brittle materials. As a result, statistical methods have been developed to calculate tensile properties. Weibull distribution is the most common cumulative distribution for strength analysis due to its flexibility. The

statistical distribution of fiber strengths is usually obtained by means of the Weibull equation [162, 163].

Weibull distribution is a continuous probability distribution named after Waloddi Weibull, who described it in detail in 1951. Weibull defined the probability distribution function as;

$$F(t) = 1 - e^{-\frac{(t-\tau)^\alpha}{\beta}} \quad (6.1)$$

where the three parameters of the distribution are given by the set $\theta = \{\alpha, \beta, \tau\}$ with $\alpha > 0$, $\beta > 0$ and $\tau \geq 0$; β is a scale parameter, α is the shape parameter that determines the appearance or shape of the distribution and τ is the location parameter [164]. τ is mostly used for distributions which are time dependable. As a result, two parameter Weibull distributions are most commonly used by research groups due to flexibility.

6.2.2 Statistical Strength Analysis of Single CF

Carbon fibers are highly gauge length sensitive. As a result, Equation 6.1 can be written as;

$$F(\sigma_f) = 1 - \exp\left[-\frac{L}{L_0}\left(\frac{\sigma_f}{\sigma_0}\right)^m\right] \quad (6.2)$$

where $F(\sigma_f)$ is the cumulative probability of failure of a carbon fiber of length L , σ_f is the failure strength, m is Weibull shape parameter, σ_0 is scale parameter. L_0 is the scale parameter for gauge length, generally taken to be 1.

Probability can be described from experimental test data as;

$$F(\sigma_f) = \frac{i}{n+1} \quad (6.3)$$

where i is the number of fibers that have broken at or below a stress level and n is the total number of fiber tested [165].

Weibull parameters can be determined from experimental data. One of the most accurate and practical methods is graphical. Equation 6.2 can be written as;

$$\ln\left(\ln\left[\frac{1}{1-F(\sigma_f)}\right]\right) = m \ln(\sigma_f) - m_f \ln\left(\sigma_0 \left(\frac{L_0}{L}\right)^{\frac{1}{m}}\right) \quad (6.4)$$

The purpose of using \ln function is to fit data into linear regression. Hence, the Weibull parameters can be calculated by linear regression from the plot of Equation 6.4.

6.2.2 Statistical Strength Analysis of CF Bundle

Chi et al. [160] modified Weibull distribution equation to derive Weibull parameters for a single fiber from a fiber bundle test. Equation 2 represents one single fiber failure probability. According to the Hooke's Law, stress- strain relationship is in elastic region,

$$\sigma = E_f \varepsilon \quad (6.5)$$

where E_f is the fiber Young's modulus.

Equation 6.2 can be modified in order to investigate load- strain relation by applying the Hooke's law,

$$F(\varepsilon) = 1 - \exp\left[-\frac{L}{L_0} \left(\frac{\varepsilon}{\varepsilon_0}\right)^m\right] \quad (6.6)$$

where $F(\varepsilon)$ is the failure probability of a single fiber and ε_0 is the scale parameter. The number of surviving fibers in a bundle N_0 is

$$N = N_0[1 - F(\varepsilon)] = N_0 \exp[-L(\varepsilon/\varepsilon_0)^m] \quad (6.7)$$

A relation can be written between N and applied tensile load P by

$$P = \sigma AN = \varepsilon AE_f N_0 \exp\left[-\frac{L}{L_0} \left(\frac{\varepsilon}{\varepsilon_0}\right)^m\right]. \quad (6.8)$$

Bundle static force-strain curve can be derived from Equation 6.5 if the Weibull parameters are known. On the other hand, Weibull parameters can be calculated for a single fiber if the force-strain data for bundle is known. There are two main methods to estimate Weibull parameters. The first method is the slope method, and second is the derivation of parameters from a maximum tensile load point.

6.2.2.1 Slope Method

In order to calculate the slope of the $P - \varepsilon$ curve, the derivative of Equation 6.8 is used:

$$\frac{dP}{d\varepsilon} = AE_f N_0 \exp\left[1 - m_f \frac{L}{L_0} \left(\frac{\varepsilon_f}{\varepsilon_0}\right)^m\right] \exp\left[-\frac{L}{L_0} \left(\frac{\varepsilon_f}{\varepsilon_0}\right)^m\right]. \quad (6.9)$$

The slope when $\varepsilon = 0$ is

$$S_0 = AE_f N_0 \quad (6.10)$$

From Equation 6.8 and 6.10, the tangent line of the $P - \varepsilon$ curve at $\varepsilon = 0$ is

$$P^* = AE_f N_0 \varepsilon \quad (6.11)$$

and

$$\frac{P}{P^*} = 1 - F(\varepsilon). \quad (6.12)$$

The procedure of calculation parameters,

- 1- Obtain P and ε values from the bundle test.
- 2- Calculate slope S_0 from Equation 6.10.
- 3- Calculate the fiber survivability from Equation 6.12 corresponding to each strain from experimental $P - \varepsilon$.
- 4- Experimental data points of log-log $1 - F(\varepsilon)$ are plotted for corresponding strain and calculating Weibull parameters. The slope of the straight line will be m . Scale parameter ε_0 can be derived from linear regression.

6.2.2.2 Maximum Point Method

The strain at maximum load on the $P - \varepsilon$ curve can be calculated from Equation 9 where $dP/d\varepsilon = 0$ as

$$\varepsilon_{\max} = \varepsilon_0 \left(\frac{1}{Lm} \right)^{1/m} \quad (6.13)$$

Maximum load is from Equations 6.5, 6.8 and 6.13 is

$$P_{\max} = AN_0 E_f \varepsilon_0 \left(\frac{1}{Lm} \right)^{1/m} \quad (6.14)$$

From Equations 6.10, 6.13 and 6.1, the straight line between origin and the point of P_{\max} is

$$S_A = \frac{P_{\max}}{\varepsilon_{\max}} = S_0 \left(\frac{1}{e} \right)^{1/m} \quad (6.15)$$

or

$$m = 1/\ln \left(\frac{\varepsilon_m S_0}{P_{\max}} \right). \quad (6.16)$$

The procedure of calculation parameters,

- 1- Obtain P_{max} and ε_m values from the experimental bundle test.
- 2- Determine slope S_0 from Equation 6.10.
- 3- Calculate the shape parameters from Equation 6.16.
- 4- Obtain the scale parameter ε_0 from Equation 6.13 [160].

6.2.2.3 Non-linear Elasticity Effect

Moser et al. [166] studied the non-linear elasticity influence on the determination of Weibull parameters for the fiber bundle tensile test. Neglecting non-linear elasticity effects might cause significant error. Non-linear elastic deformation of carbon fibers can be determined by adding a linear strain-dependent term to the initial Young's modulus, E_f^0 .

The strain depended fiber Young's modulus is

$$E_f(\varepsilon) = E_f^0(1 + \alpha\varepsilon) \quad (6.17)$$

where α is the elastic non-linearity that can range from -7 to 30.

In this study, Weibull distribution for fiber bundle tensile behavior is studied for AS4 3k filaments CF to validate the model. Single fiber Weibull parameters are derived from bundle fiber test data. These results are compared with single filament experimental data. The Non-linear- elasticity effect on Weibull parameters is also investigated. The model is extended to study electrospun carbon nanofiber (ECNFs) bundle test. Single ECNF filament tensile properties are estimated from yarn tensile test data.

6.3 Experimental

6.3.1 Sample Preparation

ASTM 1557-14 [167] standard is followed to prepare a single filament CF tensile test sample. A window frame is used to hold the sample. Gauge length is selected as 6 mm to keep gauge length as consistent with the ECNFs samples. Single filaments of CF are selected randomly from a bundle and glued on a window frame with a super glue. The DMA Q800 is employed for tensile test of single filament. 1 N/mm force control mode is used. Once the window frame is placed on the DMA, the window frame is cut the from side without damaging the fiber. The cutting approach is significant in terms of prevent damage to the fibers. Figure 6.3 shows the FEA results for two different cutting methods. Cutting the side from inside reduces stress significantly compared with separating bottom and top of the window by cutting it front face. 40 successful tests have been completed for statistical analysis.

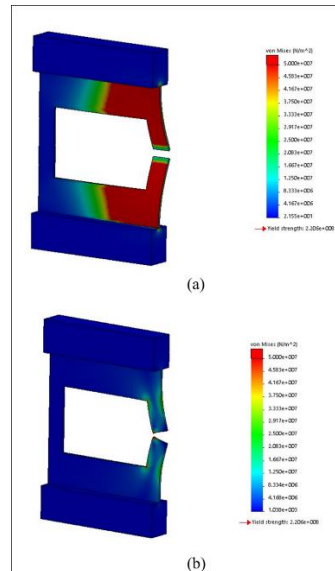


Figure 6.3 Effect of cutting direction on stress distribution for the single filament test window frame. (a) cutting the side from perpendicular to the face (b) cutting the side from inside.

The same window frames are used for ECNFs tensile tests. However, the strain control mode is used to collect more data. 0.1%/min strain rate is applied. AS4 bundle sample preparation protocols are significantly different than ECNFs and single filament CF test. 3k filaments bundles require more force to break all fibers compared to single filament test. Only a few Newtons will be sufficient enough to break all the fibers for an ECNF bundle. In comparison, CF bundle tests require a few hundred Newtons to complete the test. CF bundles are significantly larger compared to nanofibers due to the fiber diameter. Figure 6.4 shows SEM images of ECNF (a) and AS4 CF, magnified 800 times.

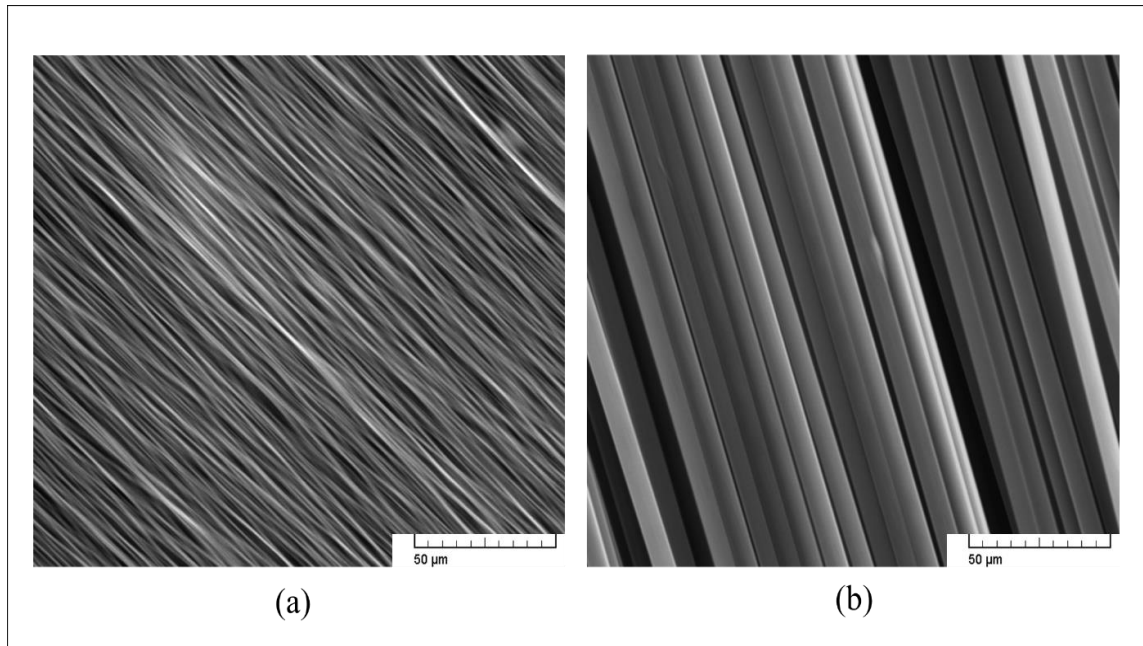


Figure 6.4 800x magnified SEM images of (a) ECNFs (b) AS4 CF.

A CF 3k bundle requires more gripping area compared to ECNF bundles. A new approach is developed to increase gripping area and prevent sliding. This new approach also reduces end effects. Figure 5 (a) shows the aluminum sample holder (2'' by 1'' and 1/8'') used to maximize gripping area for the Instron 3345 tensile test fixture. A cylindrical channel 3 mm in diameter is opened throughout the aluminum plate where the bundles are

located with an epoxy glue (Figure 6.5 (b)). A second aluminum plate is used and the second end of the fibers is glued to it (Figure 6.5. (c)). A clip is placed between the top and bottom plates to prevent gauge length changes during handling the samples. After placing the sample on the fixture, the clip is removed. The Instron 3345 tensile test machine is equipped with a 5000 N load cells; a 0.001/min strain rate is applied. Strain is measured with two different methods (extensometer and crosshead location). A 2 in gauge length extensometer is located on aluminum plates as close to the ends and displacement measured. Strain measurements from crosshead and extensometer match. No slipping is observed.

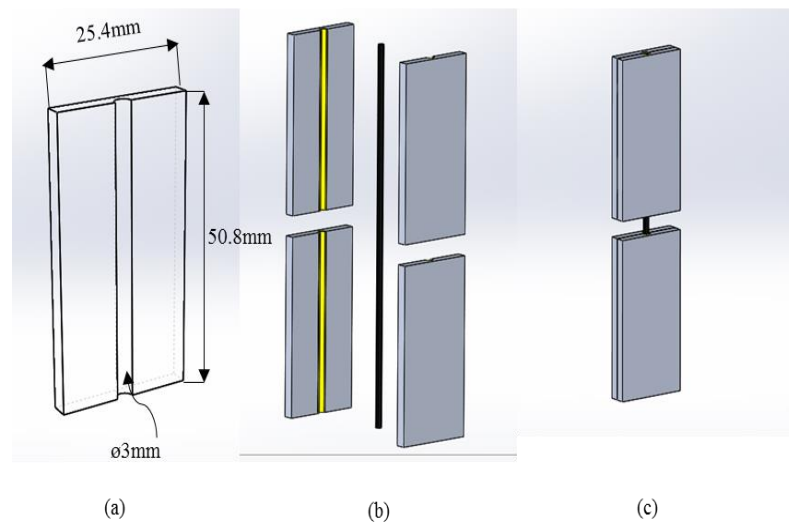


Figure 6.5 AS4 bundle test sample preparation (a) aluminum sample holder 2” by 1” and 1/8” thick (b) gluing the bundle between two aluminum plate inside the cylindrical channel with epoxy (c) bundle test sample with 6 mm gauge length which is adjustable.

6.4 Results and Discussion

6.4.1 Calculation of Single Filament CF Tensile Strength from Bundle Test

The load-strain curve data is derived from the tensile test. 5 different test data is used to calculate strength of a single filament fiber. Single filament diameter is measured

as 7 μm , and all fiber lengths are assumed to be the same. The number of filaments is given to be 3000 from the manufacturer data sheet. Weibull parameters also are calculated with maximum stress point method. Figure 6.6 shows both experimental and theoretical data. The theoretical data compares to the experimental data in the elastic region. Non-linear behavior is observed for the 3k filament AS4 CF bundle. After maximum tensile load level, some fibers show catastrophic breakage immediately. However, there are still some fibers in the bundle that survived and continued transferring the load. This complicated phenomenon can be explained via fiber-fiber interactions, such as friction and stress concentration around neighboring fibers of the broken fiber. In order to eliminate non-linear elastic behavior effect, Equations 6.14 and 6.17 are correlated. $E_f(\epsilon)$ is used for each strain data point and the initial constant E_f is replaced in the function. The theoretical stress-strain curve is replotted for four different α values. According to Figure 6.7, non-elasticity affects Weibull parameters significantly. The best fitment is obtained when $\alpha=1$. If the non-linearity is ignored, Weibull parameters are overestimated. Figure 6.8 shows the log-log plot of single filament test results. Weibull parameters are derived using the graphical method. The slope of the linear regression is calculated to be 5.25, which equals to Weibull modulus.

Weibull parameters, failure strength, and failure strain are calculated for 5 different samples and averaged. Table 6.1 summarizes the analysis results. The results do not vary significantly from sample to sample. Failure strength of a single filament CF is found to be between 3.80 and 4.17 GPa, and failure strain is derived to be between 1.26 to 1.36 %, depending on the non-linear elasticity parameters.

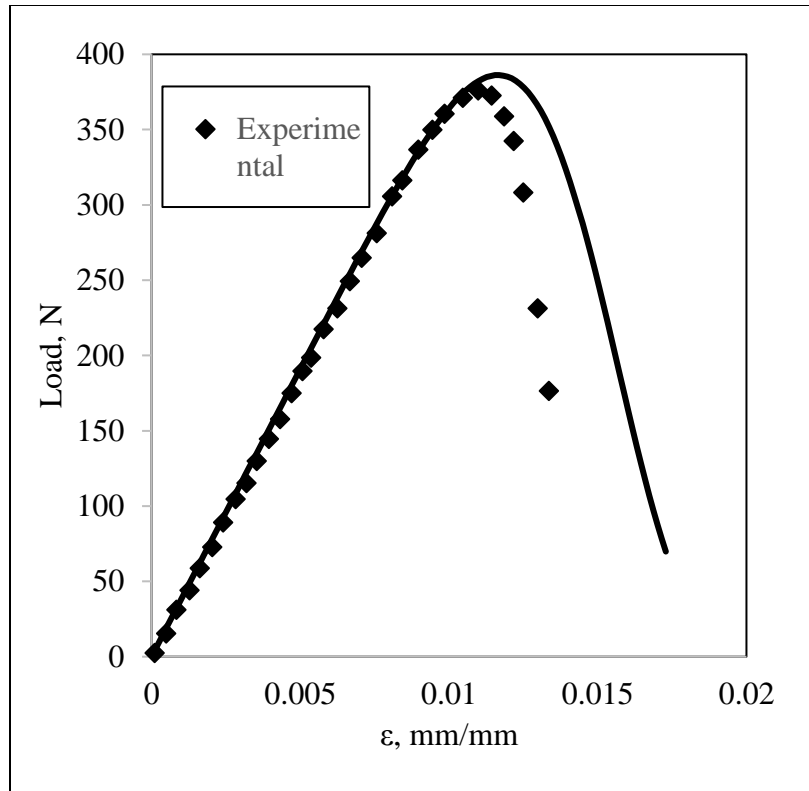


Figure 6.6 Stress-strain curve of 3k filament AS-4 micro carbon fiber.

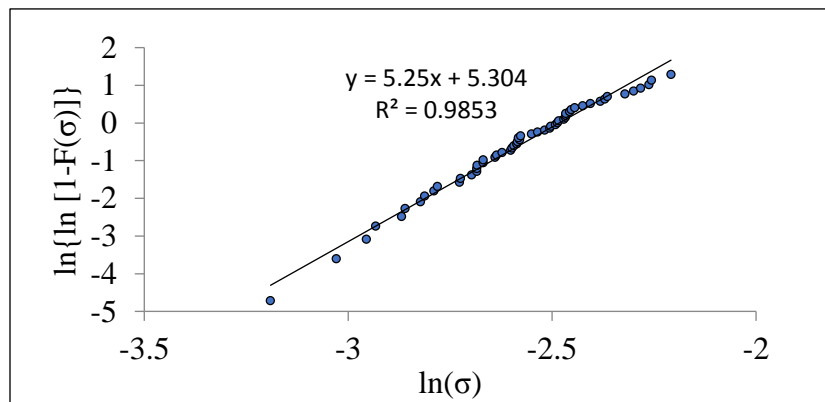


Figure 6.7 Strength distribution of single AS-4 micro carbon fiber.

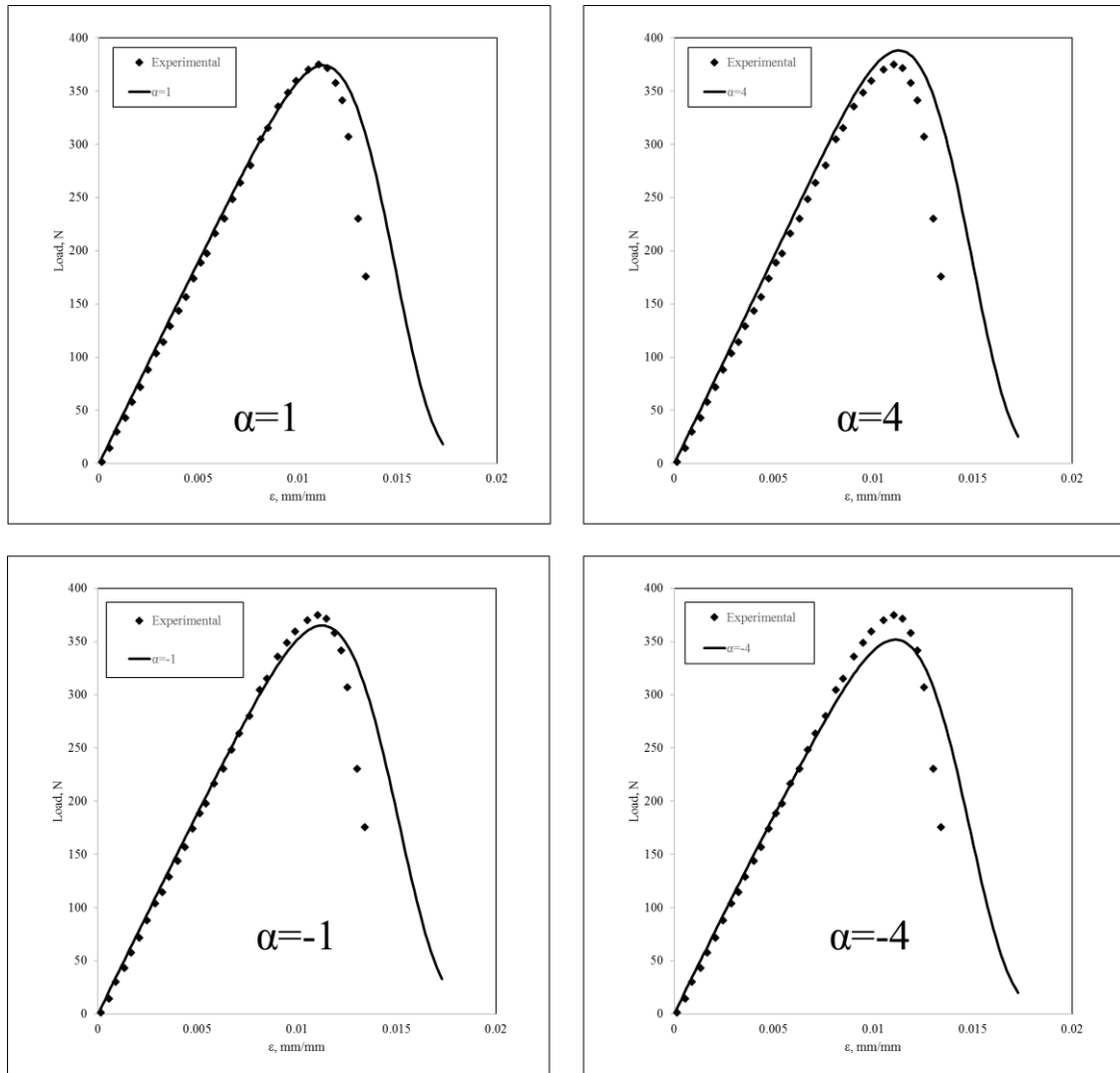


Figure 6.8 Effect of non-linear elasticity on AS4 3k bundle test, α range is -4 to 4.

The tensile strength is derived from Equation 6.6, where $F(\sigma_f) = 0.632$. ASTM C1557 standard states that when 63.2% of the fibers fail, that value is accepted as tensile strength. From the bundle test, the tensile strength is calculated as 4.17 GPa when non-elasticity is ignored. However, the theoretical value fits best when $\alpha=1$ and results in a tensile strength of 4 GPa and a failure strain of 0.0129 mm/mm.

Table 6.1 Summary of Weibull bundle analysis of AS4 CF.

Sample	Method	α	m	ϵ_0	σ_f (GPa)	ϵ_f (mm/mm)
1	Slope	0	4.74	0.0169	3.94	0.0116
	Maximum Point	-4	4.55	0.0166	3.81	0.0112
	Maximum Point	-1	4.60	0.0169	3.89	0.0114
	Maximum Point	0	4.67	0.0183	4.25	0.0125
	Maximum Point	1	4.71	0.0175	4.07	0.0120
	Maximum Point	4	4.74	0.0169	3.93	0.0116
2	Slope	0	4.83	0.0173	4.05	0.0119
	Maximum Point	-4	4.64	0.0170	3.92	0.0115
	Maximum Point	-1	4.69	0.0173	4.00	0.0118
	Maximum Point	0	4.77	0.0188	4.39	0.0129
	Maximum Point	1	4.80	0.0173	4.04	0.0119
	Maximum Point	4	4.84	0.0172	4.04	0.0119
3	Slope	0	4.17	0.0148	3.28	0.0096
	Maximum Point	-4	4.01	0.0145	3.16	0.0093
	Maximum Point	-1	4.05	0.0148	3.23	0.0095
	Maximum Point	0	4.11	0.0161	3.53	0.0104
	Maximum Point	1	4.15	0.0153	3.38	0.0099
	Maximum Point	4	4.17	0.0148	3.27	0.0096
4	Slope	0	4.42	0.0157	3.56	0.0105
	Maximum Point	-4	4.25	0.0154	3.44	0.0101
	Maximum Point	-1	4.29	0.0157	3.51	0.0103
	Maximum Point	0	4.36	0.0170	3.84	0.0113
	Maximum Point	1	4.40	0.0162	3.67	0.0108
	Maximum Point	4	4.42	0.0157	3.55	0.0104
5	Slope	0	4.63	0.0166	4.83	0.0209
	Maximum Point	-4	4.45	0.0163	4.69	0.0203
	Maximum Point	-1	4.50	0.0166	4.79	0.0207
	Maximum Point	0	4.58	0.0180	4.83	0.0209
	Maximum Point	1	4.61	0.0166	4.82	0.0209
	Maximum Point	4	4.65	0.0165	4.81	0.0208
Average	Slope	0	4.56	0.0163	3.93	0.0129
	Maximum Point	-4	4.38	0.0160	3.80	0.0125
	Maximum Point	-1	4.43	0.0162	3.89	0.0128
	Maximum Point	0	4.50	0.0177	4.17	0.0136
	Maximum Point	1	4.54	0.0166	4.00	0.0131
	Maximum Point	4	4.56	0.0162	3.92	0.0129
	Single Filament	-	5.25	0.0178	4.29	0.0126

A single fiber filament tensile test is performed and fiber strength is calculated. 40 individual tensile tests are completed, and Weibull parameters are derived from log-log plot by linear regression. Failure stress is calculated to be 4.29 GPa from the single filament test. The strength value is derived to be 7% more than the result obtained via the bundle test. There are some assumptions that cause errors, such as assuming all fibers are same length and number of fibers is 3000. Additionally, fiber-fiber interaction and stress concentration around broken fibers may affect test results. However, a valid method is developed to estimate a single fiber tensile strength from the bundle test. In literature, R' Mili et al. [154] and Chi et al. [160] reported that a single carbon fiber strength may be derived from the bundle test by employing Weibull distribution, and results are comparable to the single filament tensile test results. Hence, the method is extended to derive single filament ECNFs tensile strength.

6.4.2 Estimation of Single Filament ECNF Tensile Strength from Bundle Test

DMA Q800 is employed to generate data for analyzing of ECNF single filament properties from the bundle test. The number of fibers in the bundle is calculated by the procedure explained in section 3.3.6. The average fiber diameter is derived from SEM images. The number of fiber in a bundle varies between 1300-1600 due to the nature of the electrospinning itself. However, SEM images do not show any sign of discontinuous fibers in the bundle. Thus, fibers are assumed continuous. Additionally, while all individual fibers are aligned perfectly in an AS4 bundle, there are some fibers are not ordered in the ECNF bundle, resulting in 2.7° standard deviation of the angle distribution (Figure 6.4).

Weibull parameters are obtained with the maximum stress point method that produces more accurate results. Figure 6.9 shows both experimental and theoretical data of

ECNF bundle test. Theoretical data fits the experimental data in the elastic region. Non-linear behavior is also observed in the ECNF bundle test results. Non-linear elasticity is also investigated. The theoretical stress-strain curve is rederived for four different α values. According to Figure 6.10, non-elasticity alters the theoretical stress-strain curve significantly. $\alpha=1$ gives the best theoretical estimations for ECNF.

Table 6.2 summaries the analysis results. Weibull parameters, failure strength, failure strain are calculated for 5 different samples and averaged. Failure strength of a single filament ECNF is found to be between 2.10 to 2.52 GPa, and failure strain is derived to be between 1.08 to 1.15 %, depending on the non-linear elasticity coefficient.

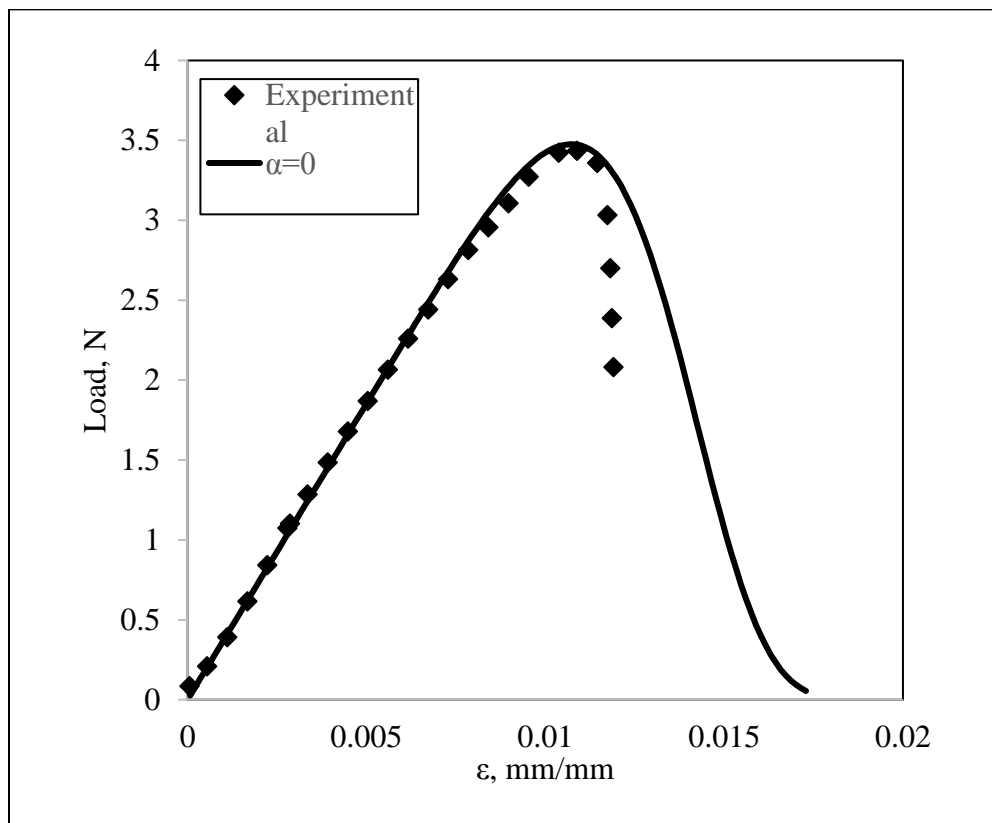


Figure 6.9 Stress-strain curve of 1500 filament ECNFs (average diameter 204 nm, $.2.7^\circ$ standard deviation of the angle distribution, and gauge length 6mm).

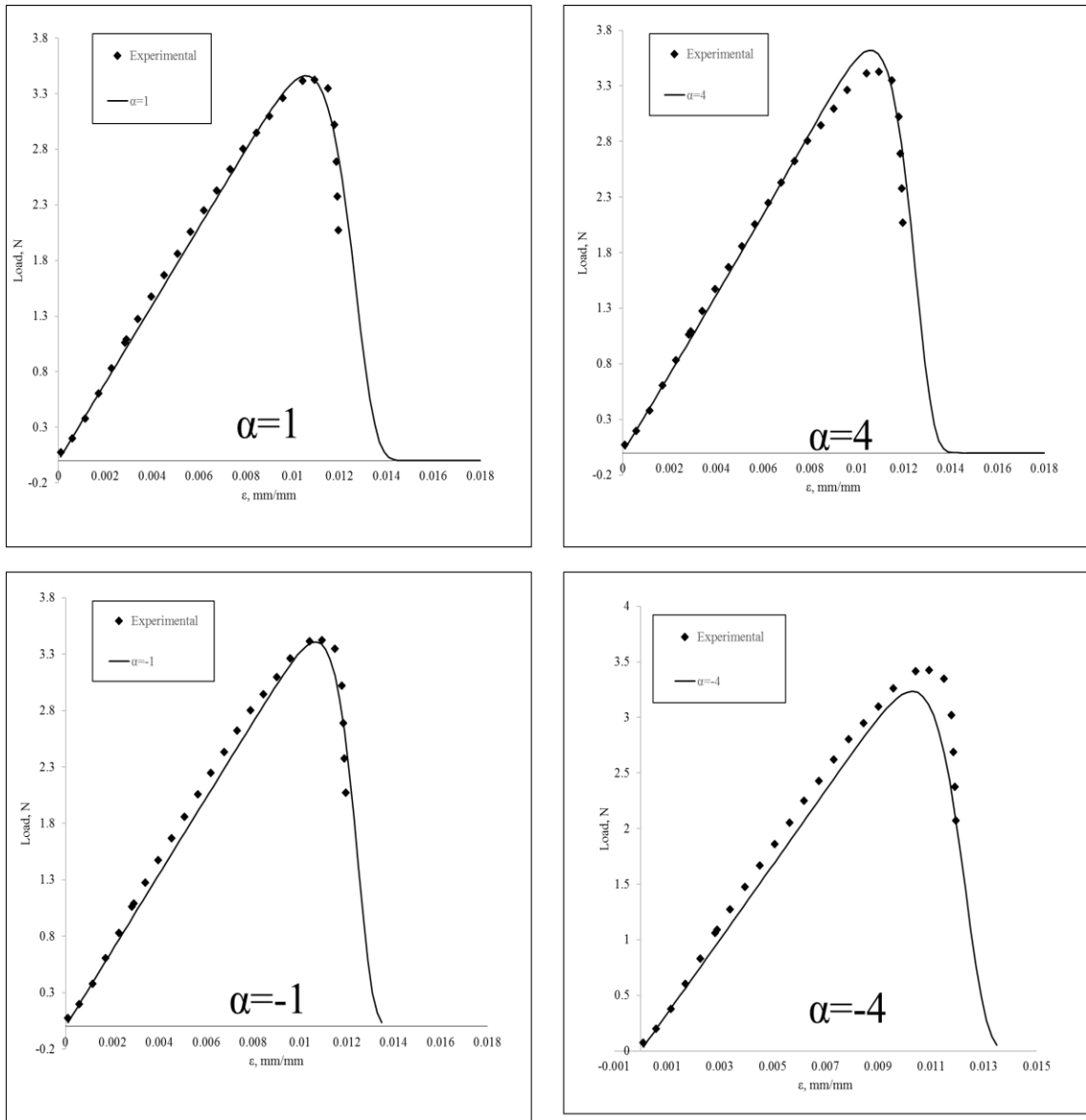


Figure 6.10 Effect of non-linear elasticity on theoretical stress-strain curve of ECNF bundle (average diameter 204 nm, and 6mm gauge length) 1.5k bundle test, α (non-linear elasticity coefficient) range is -4 to 4.

Table 6.2 Summary of Weibull bundle analysis of ECNF.

Sample	Method	α	m	ϵ_0	σ_f (GPa)	ϵ_f (mm/mm)
1	Slope	0	6.35	0.0169	2.81	0.0128
	Maximum Point	-4	6.08	0.0146	2.39	0.0109
	Maximum Point	-1	6.19	0.0155	2.55	0.0116
	Maximum Point	0	6.23	0.0162	2.67	0.0122
	Maximum Point	1	6.31	0.0158	2.62	0.0119
	Maximum Point	4	6.39	0.0148	2.46	0.0112
2	Slope	0	5.39	0.0108	1.70	0.0077
	Maximum Point	-4	5.16	0.0093	1.44	0.0066
	Maximum Point	-1	5.25	0.0099	1.54	0.0070
	Maximum Point	0	5.29	0.0103	1.62	0.0073
	Maximum Point	1	5.36	0.0101	1.58	0.0072
	Maximum Point	4	5.42	0.0094	1.49	0.0068
3	Slope	0	6.67	0.0182	3.06	0.0139
	Maximum Point	-4	6.38	0.0157	2.61	0.0119
	Maximum Point	-1	6.50	0.0167	1.44	0.0127
	Maximum Point	0	6.54	0.0174	2.91	0.0132
	Maximum Point	1	6.63	0.0170	2.85	0.0130
	Maximum Point	4	6.71	0.0159	2.68	0.0122
4	Slope	0	5.62	0.0130	2.07	0.0094
	Maximum Point	-4	5.92	0.0157	2.55	0.0116
	Maximum Point	-1	5.67	0.0136	2.17	0.0099
	Maximum Point	0	5.77	0.0144	2.32	0.0105
	Maximum Point	1	5.81	0.0150	2.43	0.0110
	Maximum Point	4	5.89	0.0147	2.38	0.0108
5	Slope	0	5.96	0.0163	2.66	0.0121
	Maximum Point	-4	6.28	0.0198	3.27	0.0149
	Maximum Point	-1	6.01	0.0171	2.79	0.0127
	Maximum Point	0	6.12	0.0181	2.98	0.0135
	Maximum Point	1	6.16	0.0189	3.12	0.0142
	Maximum Point	4	6.24	0.0185	3.05	0.0139
Average	Slope	0	6.00	0.0150	2.46	0.0112
	Maximum Point	-4	5.97	0.0150	2.45	0.0112
	Maximum Point	-1	5.93	0.0145	2.10	0.0108
	Maximum Point	0	5.99	0.0153	2.50	0.0114
	Maximum Point	1	6.05	0.0154	2.52	0.0115
	Maximum Point	4	6.13	0.0147	2.41	0.0110

A single nanofiber tensile test is possible with recent technological developments by employing microelectromechanical systems (MEMS). Table 6.3 indicates some research about testing single CNF. Single filament tensile strength of ECNF and VGCNF reported in literature are higher than those obtained from bundle test results. The strength of single filament ECNF is found to be 2.52 GPa from the bundle test; in literature the strength is reported to be between 3.34 GPa to 3.8 GPa [168–170]. However, the gauge length is significantly low compared to the bundle test gauge length. The gauge length is reported to be less than 100 μm for MEMS based tensile test setup, while the bundle test gauge length is 6000 μm , 60 times more.

Table 6.3 Single filament CNF test result from literature.

Author	Year	Process Parameters	Test Conditions	Tensile Strength	Elastic Modulus
Chawla et al. [169]	2017	Electrospun Hot-drawn 4x- Carbonized at 1100°C	Single Fiber- Gauge Length ~100 μm	3.8 GPa	209 GPa
Arshad et al. [170]	2010	Electrospun- Hot-drawn 4x-1400°C	Single Fiber- Gauge Length ~50 μm	3.5 GPa	172 GPa
Ozkan et al. [168]	2008	VGCNFs	Single Fiber- Gauge Length ~100 μm	3.34 GPa	245GPa

Pickering and Murray [171] reported that PAN based CF strength varies depending on gauge length. Tensile strength is 4.75 GPa for 1 mm gauge length. However, it reduces to 2.2 GPa when the gauge length is 500 mm. Naito et al. investigated gauge length effects on Weibull parameters. They reported that the Weibull modulus increases with the reduction of gauge length as seen in Figure 6.11 [172].

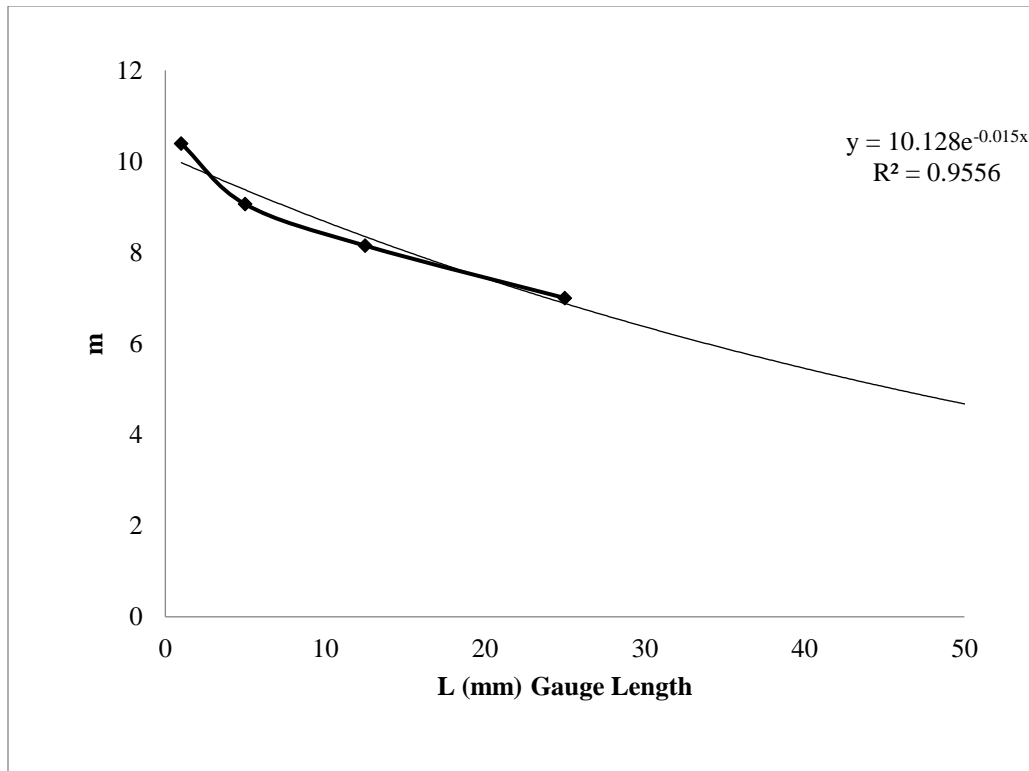


Figure 6.11 Effect of gauge length on Weibull modulus of PAN base CF T1000GB [172].

From Equation 6.6, the failure strength can be calculated for 100 μm gauge length. Figure 12 shows the failure strength of single filament ECNF as a function of gauge length. Higher gauge length results in less failure strength. The failure strength for 100 μm is obtained as 4.42 GPa without modifying Weibull parameters. However, Weibull modulus is also influenced by gauge length. Once Weibull modulus is modified

according to the trend that is shown on Figure 6.11, the failure strength is obtained as 3.93 GPa.

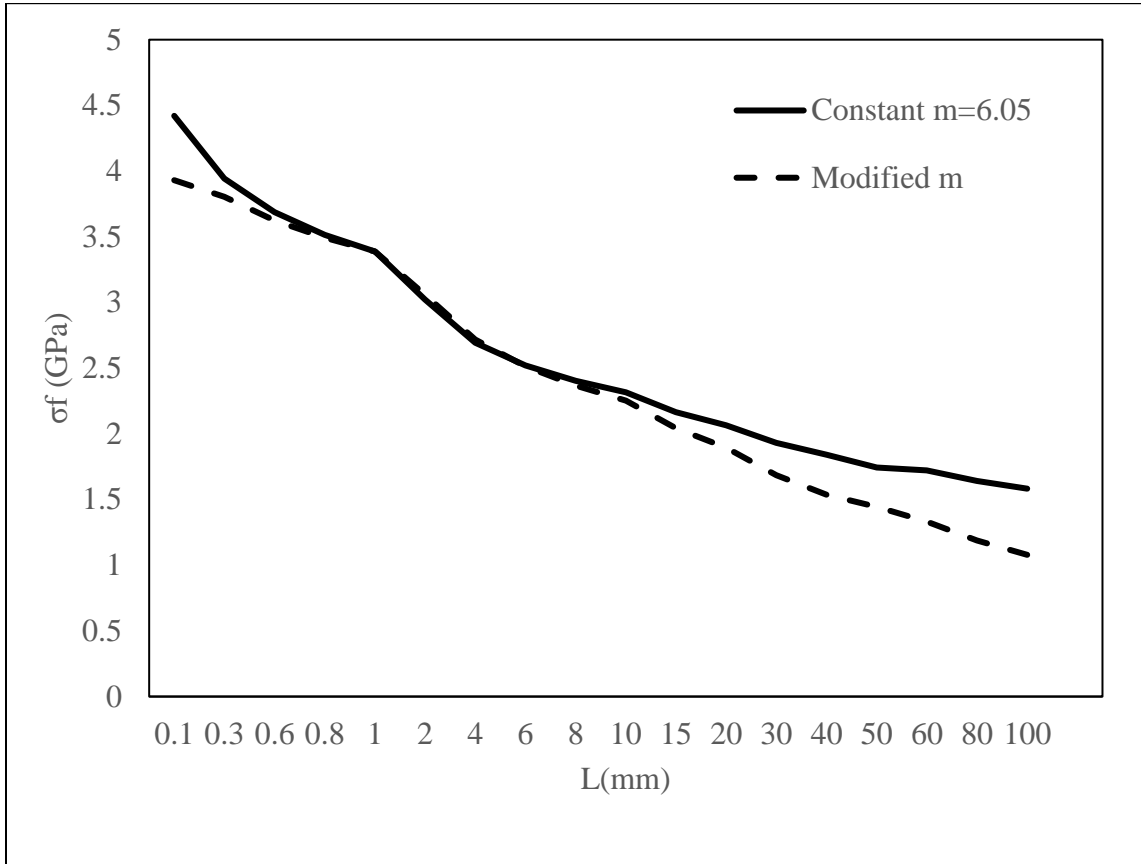


Figure 6.12 Failure strength estimation from bundle test as a function of gauge length for ECNF.

6.4.3 Alignment Effect on Tensile Strength of ECNF

Alignment effects on tensile strength are also investigated. ECNF bundles, with standard deviation of fiber angle distribution varying between 2.7° and 19.6° , are tested. α is taken to be 1 and only one coefficient is studied. Figure 6. 12 shows theoretical stress-strain and experimental results. The stress-strain behavior differs depending on fiber alignment. When the standard deviation increases, the peak becomes relatively wider.

Additionally, the amount of force to break the bundle reduces when the standard deviation increases. Furthermore, tensile testing might start to align the fibers that are not aligned by increasing strain.

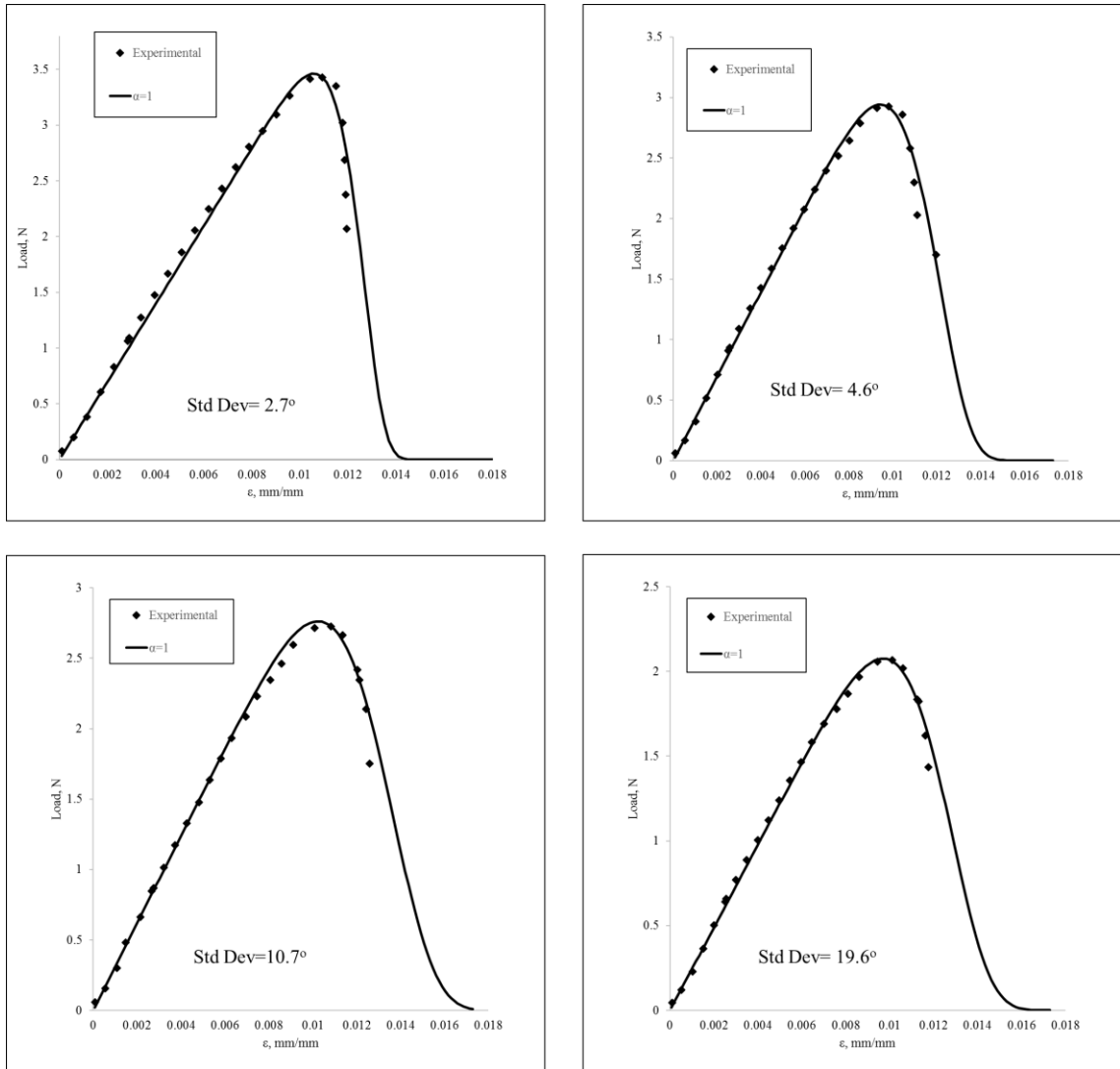


Figure 6.13 Effect of standard deviation of the angle distribution on ECNF theoretical stress-strain curve of ECNF bundle.

Weibull parameters are calculated for each test samples. It is found that the parameters have a trend depending on fiber alignment. The shape parameter follows a linear trend as seen Figure 6. 13. According to the trend line, the shape parameter is

estimated to be 0.0162 for perfectly aligned ECFN. The Weibull modulus can be estimated from the experimental data (Figure 6.14). m is estimated to be 9.399 for a perfectly aligned bundle.

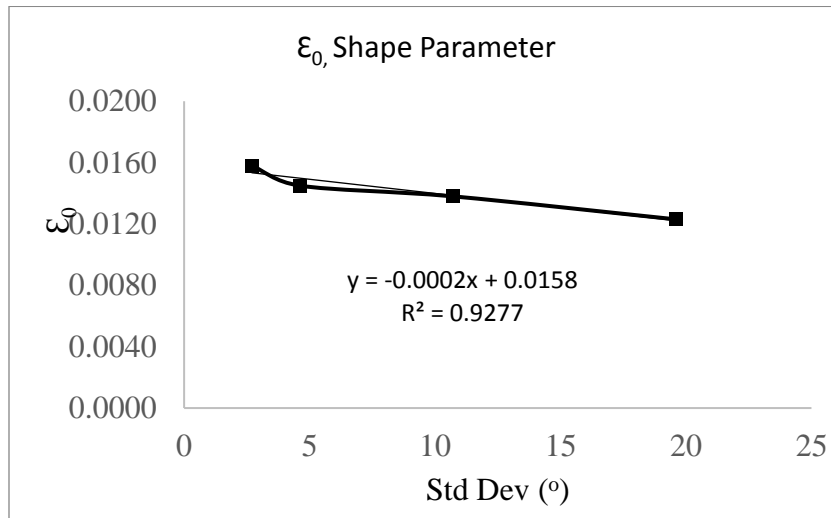


Figure 6.14 Weibull shape parameter of ECFN derived from bundle test as a function average fiber angle.

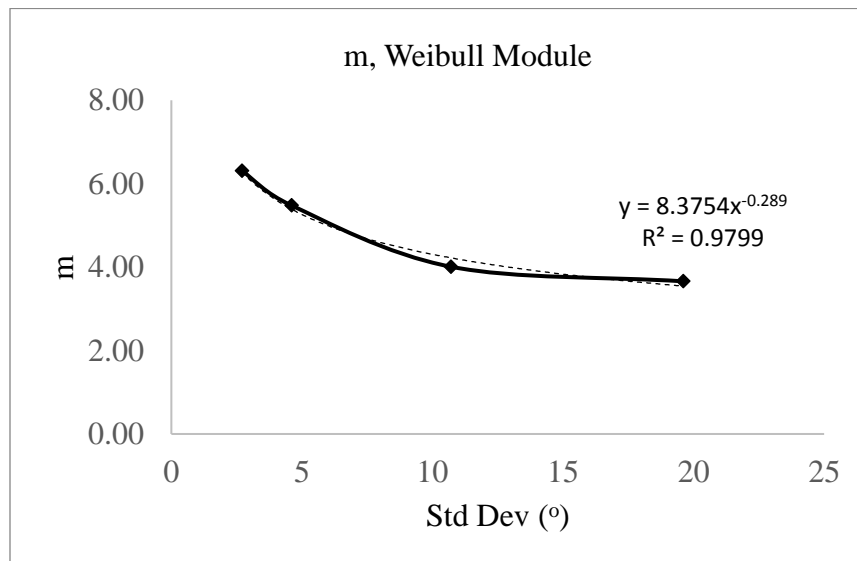


Figure 6.15 Weibull shape modulus of ECFN derived from bundle test as a function standard deviation of the angle distributions.

Table 6.4 shows the Weibull modulus, shape parameters, tensile strength and failure strain as a function of fiber angle. High fiber angles show relatively weak tensile strength and low failure strain compared to low fiber angle. Tensile strength is found to be only 1.66 GPa for a standard deviation of 19.6°, while 2.7° results in a tensile strength of 2.52 GPa. Tensile strength and failure strain of perfectly aligned (0° standard deviation) bundles is calculated from the estimated Weibull parameters. The strength is calculated to be 2.94 GPa, which is a 17% improvement compared to the standard deviation, 2.7°. Furthermore, failure strain is improved significantly from 0.0119 mm/mm to 0.0162 mm/mm. Also, gauge length effect on tensile strength for perfectly aligned ECNF bundle is calculated. For 100 µm gauge length, the failure strength is obtained as 4.25 GPa with modified Weibull modulus.

Table 6.4 Tensile strength of ECNF derived from bundle test as a function of standard deviation of the fiber angle distributions.

Std Dev (°)	m	ϵ_0	L (mm)	σ_f (GPa)	ϵ_f (mm/mm)
19.6	3.66	0.0123	6	1.66	0.0075
10.7	4.01	0.0138	6	1.94	0.0088
4.6	5.48	0.0145	6	2.30	0.0105
2.7	6.31	0.0158	6	2.52	0.0119
0 (predicted)	9.39	0.0162	6	2.94	0.0162
0 (predicted)	9.39	0.0162	0.1	4.55	0.0207
0 (predicted) (modified m)	13.01	0.0162	0.1	4.25	0.0193

6.5 Chapter Conclusions

In this chapter, statistical analysis of tensile strength of CF and ECF bundle are studied. The Weibull distribution method is employed. Weibull parameters for single filament fiber strength are derived from the bundle test. Two different methods are introduced. The slope method is the simpler method. Weibull parameters can be estimated with this method with tolerable error. However, the maximum load point method is more flexible. Non-linear elasticity effects are investigated. AS4 commercial micro carbon fiber bundle with 3000 individual fibers is employed to validate the model. Tensile strength is found to be 4 GPa which is 7% less than single filament test results of AS4. Four different α (non-linear elasticity coefficient) values are performed. The optimum α value is determined for AS4. $\alpha = 1$ results in best fit with experimental data.

Similarly, the model is used to determine tensile strength of single filament electrospun carbon nanofiber from the bundle test. The tensile strength is derived to be 2.52 GPa for a standard deviation of angle distribution 2.7° . Additionally, fiber alignment effects on tensile strength were investigated. Tensile strength is found to be only 1.66 GPa for a 19.6° standard deviation, while a 2.7° standard deviation results in a tensile strength of 2.52 GPa. Once, the failure strength is recalculated for 100 μm gauge length, the failure strength is obtained as 3.93 GPa. A relation between Weibull parameters and fiber alignment is obtained from the experimental results. Tensile strength and failure strain at a fiber angle standard deviation of 0° is calculated from the estimated Weibull parameters. The strength is estimated to be 2.94 GPa, which is 17% improvement compared with the standard deviation of 3.1° standard deviation. For 100 μm gauge length, the failure strength

calculated as 4.25 GPa. A valid method is developed to estimate single filament CF and ECNF tensile strength from the bundle test. This approach gives valuable results with less effort and number of samples compared to the single filament test.

Chapter 7 : CONCLUDING REMARKS

7.1 Conclusions

Fiber alignment, diameter distribution, and mechanical properties of electrospun PAN nanofibers have been studied as a function of collector speed, collector geometry and electrode type. The effects of hot stretching and stabilization under tension on the mechanical properties of fibers were investigated. Finally, a statistical model was developed to determine single filament electrospun carbon fiber tensile strength from the bundle test. The key conclusions of this study are:

- A new electrospinning setup with hybrid (drum/disc) type of collector design is made and bead free electrospun nanofibers are successfully generated. The system can successfully control and maintain environmental conditions (temperature and RH) and provides nanofiber yarns.
- RH affects fiber diameter, surface roughness, and tensile properties of as-spun stabilized and carbonized nanofibers. Significantly porous structures are obtained at relative humidity higher than 22%. Moreover, RH affects mechanical properties of as-spun, stabilized and carbonized nanofiber yarns. Higher fiber diameter and surface roughness are believed to be possible reasons for lower mechanical properties. The highest tensile strength (about 459 MPa) is observed for carbon nanofiber produced at 22% RH compared to about 157 MPa at 60% RH.
- Collector geometry affects electric field distribution. Wire and mesh type of collectors have more intense and uniform electric distribution on the surface compared to foil type. This explains the reduction of fiber diameter and higher degree of alignment.

- Collector speed has an important role on fiber alignment, and tensile strength of nanofibers. Lower rpm results in wider fiber angle distribution. Nanofibers produced with a wire collector show better fiber alignment compared to those produced with a mesh and foil collectors. Lower fiber alignment is believed to be possible reasons for weaker mechanical properties. The highest tensile strength (about 701 MPa) is observed for carbon nanofiber produced at 1500 rpm with wire collector compared to about 512 MPa at 500 rpm.
- SEM and FEA results show that electrode type can alter fiber diameter and alignment by manipulating electrode geometry. Average fiber diameter is reduced from 422 nm to 389 nm by using different electrodes. Additionally, fiber alignment improved by almost 50%.
- Hot stretching of electrospun PAN fibers helps to improve tensile properties and crystallinity. Unstretched nanofiber yarn tensile strength is found to be 162 MPa, while fibers stretched to $\lambda=2$ exhibit a tensile strength of 276 MPa. Moreover, the Young's modulus shows an increase from 5.1 MPa to 6.2 MPa. Crystallinity is calculated to be %70.29 for PAN nanofibers stretched to $\lambda=2$, while unstretched PAN nanofibers show a crystallinity of %50.24.
- Tension during stabilization influences fiber diameter and tensile properties of stabilized nanofibers. The highest tensile strength (about 401 MPa) is observed for fibers stretched to $\lambda=2$ with a pre-stress of 1 MPa pre-stress at stabilization, compared to about 191 MPa for unstretched fibers in the same stabilization condition.

- A valid statistical model is developed to estimate single filament fiber tensile strength from the bundle test. The model is validated with AS4 micro carbon fiber by performing the single filament test. Single filament ECNF tensile strength is derived.

7.2 Recommendations for Future Work

In this research, uniform and bead free PAN nanofibers are produced. Additionally, fiber orientation, crystallinity, and mechanical properties are remarkably improved. However, mechanical properties of ECNFs are still lower than commercial micro CFs. Mechanical properties of ECNFs must be improve; the following study is suggested:

- 2D FEA method was employed for analyzing electric field distribution in this research. However, a 3D FEA will give more detailed information about electric field distribution.
- In this study, PAN nanofibers are stretched to increase macromolecular orientation. The stretch ratio is limited due to starting diameter of the nanofibers. Fibers can be stretched more to increase macromolecular orientation. Electrospinning is a versatile method; fiber diameter can be increasing by manipulating the parameters. Higher stretch ratios can be achieved by increasing fiber diameter. Thus, nanofiber yarns can be stretched more to improve macromolecular level orientation.
- Applying tension during stabilization improves mechanical properties of stabilized nanofibers. Controlling the amount of tension during carbonization may result in better macromolecular orientation, leading to better tensile properties. Thus, an

arrangement should be made to apply a controlled amount of tension during carbonization.

- In this study, carbonization is performed at 1000°C due to limitations of the tubular furnace. However, increasing carbonization temperature may cause higher mechanical properties.
- In this research, a statistical model is developed to estimate single filament ECNF tensile strength from bundle test. Only one gauge length is experimentally tested. However, it is reported that tensile strength of a single carbon fiber varies depending on gauge length [171, 172]. Different gauge length tensile tests of ECNF may yield at different tensile strength. In order to compare MEMS based single filament ECNF tensile test results, the statistical model can be extended by incorporating the gauge length parameter.
- Nanofibers can be deposited in window frames that are utilized for mechanical test in lower fiber quantities. Under microscope, these deposited nanofibers can be identified in terms of fiber angle and diameter. Knowing the composition of nanofibers that are tested will result in more accurate information in terms of the effects of diameter and fiber orientation on mechanical properties.

References

- [1] P. Morgan, *Carbon fibers and their composites*. Boca Raton, FL: Taylor & Francis, 2005.
- [2] Y. L. Han Gi Chae, Bradley A. Newcomb, Prabhakar V. Gulgunje, S. G. Kishor K. Gupta, Manjeshwar G. Kamath, Kevin M. Lyons, I. C. Chandrani Pramanik, Lucille Giannuzzi, Korhan Sahin, and S. Kumar, “High Strength and High Modulus Carbon Fibers,” *Carbon*, (2015).
- [3] S.-J. Park and G.-Y. Heo, “Precursors and Manufacturing of Carbon Fibers,” Springer, Dordrecht, 2015, pp. 31–66.
- [4] E. Fitzer and B. Terwiesch, “Carbon-Carbon Composites Unidirectionally Reinforced with Carbon and Graphite Fibers,” *Carbon*, vol. 10, pp. 385–390, (1972).
- [5] S. Ōtani, K. Yamada, T. Koitabashi, and A. Yokoyama, “On the raw materials of MP carbon fiber,” *Carbon*, vol. 4, no. 3, pp. 425–432, (1966).
- [6] E. Frank, F. Hermanutz, and M. R. Buchmeiser, “Carbon Fibers: Precursors, Manufacturing, and Properties,” *Macromolecular Materials and Engineering*, vol. 297, no. 6, pp. 493–501, (2012).
- [7] D. D. Edie and M. G. Dunham, “Melt spinning pitch-based carbon fibers,” *Carbon*, vol. 27, no. 5, pp. 647–655, (1989).
- [8] S.-H. Yoon, Y. Korai, I. Mochida, and I. Kato, “The flow properties of mesophase pitches derived from methylnaphthalene and naphthalene in the temperature range of their spinning,” *Carbon*, vol. 32, no. 2, pp. 273–280, (1994).

- [9] Z. Yue, C. Liu, and A. Vakili, “Meltblown Solvated Mesophase Pitch-Based Carbon Fibers: Fiber Evolution and Characteristics,” *Journal of Carbon Research*, vol. 3, no. 4, p. 26, (2017).
- [10] L. S. Singer, “The mesophase and high modulus carbon fibers from pitch,” *Carbon*, vol. 16, no. 6, pp. 409–415, (1978).
- [11] X. Huang, “Fabrication and Properties of Carbon Fibers,” *Materials*, vol. 2, no. 4, pp. 2369–2403, (2009).
- [12] J. Meinl, M. Kirsten, C. Cherif, and A. Michaelis, “Influence of PAN-Fiber Stretching during Thermal Treatment on the Stabilization Reactions,” *American Journal of Analytical Chemistry*, vol. 07, no. 03, pp. 282–293, (2016).
- [13] S. F. Fennessey, “Continuous Carbon Nanofibers Prepared From Electrospun Polyacrylonitrile Precursor Fibers,” PhD Dissertation, University of Massachusetts Amherst, 2006.
- [14] F. Lian, J. Liu, Z. Ma, and J. Liang, “Stretching-induced deformation of polyacrylonitrile chains both in quasicrystals and in amorphous regions during the in situ thermal modification of fibers prior to oxidative stabilization,” *Carbon*, vol. 50, no. 2, pp. 488–499, (2012).
- [15] Torayca®, “High-performance carbon fiber Torayca®.” [Online]. Available: <http://www.torayca.com/en/download/pdf/torayca.pdf>. [Accessed: 20-Jun-2018].
- [16] J. Liu, Z. Yue, and H. Fong, “Continuous Nanoscale Carbon Fibers with Superior Mechanical Strength,” *Small*, vol. 5, no. 5, pp. 536–542, (2009).
- [17] S. Das, J. Warren, and D. West, “Global Carbon Fiber Composites Supply Chain

- Competitiveness Analysis,” Knoxville, TE, (2016).
- [18] K.-H. Jung, J.-H. Byun, Y.-S. Lee, and S.-J. Park, “Synthesis and characterization of chemically modified polystyrene as processable carbon fiber precursors,” *Research on Chemical Intermediates*, vol. 36, no. 6–7, pp. 621–627, (2010).
- [19] T. Mikolajczyk and I. Krucińska, “Correlation Between Copolymer Characteristics, Conditions of Fiber Formation, and Mechanical Properties of PAN Carbon Fiber Precursor,” *Textile Research Journal*, vol. 59, no. 9, pp. 536–540, (1989).
- [20] C. A. Leon y Leon, R. A. O’Brien, J. J. McHugh, H. Dasarathy, and W. C. Schimpf, “Polyethylene and polypropylene as low cost carbon fiber (LCCF) precursors,” *International SAMPE Technical Conference*, vol. 33, no. 1, pp. 1289–1296, (2001).
- [21] X. Society of Wood Science and Technology (U.S.) and G. Forest Products Research Society., *Wood and fiber science : journal of the Society of Wood Science and Technology.*, vol. 40, no. 3. The Society, 1983.
- [22] N. Yusof and A. F. Ismail, “Polyacrylonitrile/acrylamide-based carbon fibers prepared using a solvent-free coagulation process: Fiber properties and its structure evolution during stabilization and carbonization,” *Polymer Engineering & Science*, vol. 52, no. 2, pp. 360–366, (2012).
- [23] E. Fitzer, W. Frohs, and M. Heine, “Optimization of stabilization and carbonization treatment of PAN fibres and structural characterization of the resulting carbon fibres,” *Carbon*, vol. 24, no. 4, pp. 387–395, (1986).

- [24] S. Wang, Z.-H. Chen, W.-J. Ma, and Q.-S. Ma, "Influence of heat treatment on physical–chemical properties of PAN-based carbon fiber," *Ceramics International*, vol. 32, no. 3, pp. 291–295, (2006).
- [25] M.-S. Park, M.-J. Jung, and Y.-S. Lee, "Significant reduction in stabilization temperature and improved mechanical/electrical properties of pitch-based carbon fibers by electron beam irradiation," *Journal of Industrial and Engineering Chemistry*, vol. 37, pp. 277–287, (2016).
- [26] H. Chen, Y. Pan, S. Hou, Z. Shao, Y. Hong, and A. Ju, "Poly(acrylonitrile- *co* -2-methylenesuccinamic acid) as a potential carbon fiber precursor: preparation and stabilization," *RSC Advances*, vol. 7, no. 85, pp. 54142–54152, (2017).
- [27] E. Fitzer, "Pan-based carbon fibers—present state and trend of the technology from the viewpoint of possibilities and limits to influence and to control the fiber properties by the process parameters," *Carbon*, vol. 27, no. 5, pp. 621–645, (1989).
- [28] G. G. Tibbetts, "Vapor-grown carbon fibers: Status and prospects," *Carbon*, vol. 27, no. 5, pp. 745–747, (1989).
- [29] M. H. Al-Saleh and U. Sundararaj, "A review of vapor grown carbon nanofiber/polymer conductive composites," *Carbon*, vol. 47, no. 1, pp. 2–22, (2009).
- [30] S. Iijima, "Helical microtubules of graphitic carbon," *Nature*, vol. 354, no. 6348, pp. 56–58, (1991).
- [31] B. Peng *et al.*, "Measurements of near-ultimate strength for multiwalled carbon nanotubes and irradiation-induced crosslinking improvements," *Nature*

- Nanotechnology*, vol. 3, no. 10, pp. 626–631, (2008).
- [32] B. Ribeiro *et al.*, “Carbon nanotube buckypaper reinforced polymer composites: a review,” *Polímeros*, vol. 27, no. 3, pp. 247–255, (2017).
- [33] A. G. Rinzler *et al.*, “Large-scale purification of single-wall carbon nanotubes: process, product, and characterization,” *Applied Physics A: Materials Science & Processing*, vol. 67, no. 1, pp. 29–37, (1998).
- [34] Z. F. Ren *et al.*, “Synthesis of large arrays of well-aligned carbon nanotubes on glass,” *Science (New York, N.Y.)*, vol. 282, no. 5391, pp. 1105–7, (1998).
- [35] N. Grobert, “Carbon nanotubes – becoming clean,” *Materials Today*, vol. 10, no. 1–2, pp. 28–35, (2007).
- [36] E. Pfautsch, *Challenges in Commercializing Carbon Nanotube Composites*. 2007.
- [37] J. H. Du, *The present status and key problems of carbon nanotube based polymer composites*, vol. 1. 2007.
- [38] N. Tucker, J. Stanger, M. Staiger, H. Razzaq, and K. Hofman, “The History of the Science and Technology of Electrospinning from 1600 to 1995.,” *Journal of Engineered Fibers and Fabrics*, vol. 7, no. SPECIAL ISSUE, pp. 63–73, (2012).
- [39] John F Cooley, “Apparatus for electrically dispersing fluids.,” 06-Oct-1899.
- [40] J. Zeleny, “The Electrical Discharge from Liquid Points, and a Hydrostatic Method of Measuring the Electric Intensity at Their Surfaces,” *Physical Review*, vol. 3, no. 2, pp. 69–91, (1914).
- [41] G. Taylor, “Electrically Driven Jets,” *Proceedings of the Royal Society A:*

- Mathematical, Physical and Engineering Sciences*, vol. 313, no. 1515, pp. 453–475, (1969).
- [42] G. Taylor, “Disintegration of Water Drops in an Electric Field,” *Proceedings of the Royal Society A: Mathematical, Physical and Engineering Sciences*, vol. 280, no. 1382, pp. 383–397, (1964).
- [43] G. Taylor, “Studies in Electrohydrodynamics. I. The Circulation Produced in a Drop by Electrical Field,” *Proceedings of the Royal Society A: Mathematical, Physical and Engineering Sciences*, vol. 291, no. 1425, pp. 159–166, (1966).
- [44] Harold L Simons, “Process and apparatus for producing patterned non-woven fabrics,” 15-Jan-1963.
- [45] J. Doshi and D. H. Reneker, “Electrospinning process and applications of electrospun fibers,” *Journal of Electrostatics*, vol. 35, no. 2–3, pp. 151–160, (1995).
- [46] Dan Li, A. Yuliang Wang, and Y. Xia*, “Electrospinning of Polymeric and Ceramic Nanofibers as Uniaxially Aligned Arrays,” (2003).
- [47] S. Koombhongse, W. Liu, and D. H. Reneker, “Flat polymer ribbons and other shapes by electrospinning,” *Journal of Polymer Science Part B: Polymer Physics*, vol. 39, no. 21, pp. 2598–2606, (2001).
- [48] B. Barua and M. C. Saha, “Investigation on jet stability, fiber diameter, and tensile properties of electrospun polyacrylonitrile nanofibrous yarns,” *Journal of Applied Polymer Science*, vol. 132, no. 18, (2015).
- [49] K. Garg and G. L. Bowlin, “Electrospinning jets and nanofibrous structures,”

- Biomicrofluidics*, vol. 5, no. 1, p. 013403, (2011).
- [50] G. Zou *et al.*, “Carbon nanofibers: Synthesis, characterization, and electrochemical properties,” *Carbon*, vol. 44, no. 5, pp. 828–832, (2006).
- [51] R. Palazzetti, “Flexural behavior of carbon and glass fiber composite laminates reinforced with Nylon 6,6 electrospun nanofibers,” *Journal of Composite Materials*, vol. 49, no. 27, pp. 3407–3413, (2015).
- [52] R. Palazzetti and A. Zucchelli, “Electrospun nanofibers as reinforcement for composite laminates materials – A review,” *Composite Structures*, vol. 182, pp. 711–727, (2017).
- [53] T. M. Brugo, G. Minak, A. Zucchelli, H. Saghafi, and M. Fotouhi, “An Investigation on the Fatigue based Delamination of Woven Carbon-epoxy Composite Laminates Reinforced with Polyamide Nanofibers,” *Procedia Engineering*, vol. 109, pp. 65–72, (2015).
- [54] H. S. Yoo, T. G. Kim, and T. G. Park, “Surface-functionalized electrospun nanofibers for tissue engineering and drug delivery,” *Advanced Drug Delivery Reviews*, vol. 61, no. 12, pp. 1033–1042, (2009).
- [55] W.-J. Li, C. T. Laurencin, E. J. Caterson, R. S. Tuan, and F. K. Ko, “Electrospun nanofibrous structure: A novel scaffold for tissue engineering,” *Journal of Biomedical Materials Research*, vol. 60, no. 4, pp. 613–621, (2002).
- [56] T. J. Sill and H. A. von Recum, “Electrospinning: Applications in drug delivery and tissue engineering,” *Biomaterials*, vol. 29, no. 13, pp. 1989–2006, (2008).
- [57] D. S. Katti, K. W. Robinson, F. K. Ko, and C. T. Laurencin, “Bioresorbable

- nanofiber-based systems for wound healing and drug delivery: Optimization of fabrication parameters,” *Journal of Biomedical Materials Research*, vol. 70B, no. 2, pp. 286–296, (2004).
- [58] C. J. Buchko, K. M. Kozloff, and D. C. Martin, “Surface characterization of porous, biocompatible protein polymer thin films,” *Biomaterials*, vol. 22, no. 11, pp. 1289–1300, (2001).
- [59] X. Mo and H.-J. Weber, “Electrospinning P(LLA-CL) nanofiber: A tubular scaffold fabrication with circumferential alignment,” 2004, vol. 217, pp. 413–416.
- [60] C. . Xu, R. Inai, M. Kotaki, and S. Ramakrishna, “Aligned biodegradable nanofibrous structure: a potential scaffold for blood vessel engineering,” *Biomaterials*, vol. 25, no. 5, pp. 877–886, (2004).
- [61] N. Naveen, R. Kumar, S. Balaji, T. S. Uma, T. S. Natrajan, and P. K. Sehgal, “Synthesis of Nonwoven Nanofibers by Electrospinning - A Promising Biomaterial for Tissue Engineering and Drug Delivery,” *Advanced Engineering Materials*, vol. 12, no. 8, pp. B380–B387, (2010).
- [62] V. Thavasi, G. Singh, and S. Ramakrishna, “Electrospun nanofibers in energy and environmental applications,” (2008).
- [63] J. A. Howell, “Future of membranes and membrane reactors in green technologies and for water reuse,” *Desalination*, vol. 162, pp. 1–11, (2004).
- [64] C. Liu, Z. Noda, K. Sasaki, and K. Hayashi, “Development of a polyaniline nanofiber-based carbon monoxide sensor for hydrogen fuel cell application,” *International Journal of Hydrogen Energy*, vol. 37, no. 18, pp. 13529–13535,

(2012).

- [65] S. Peng *et al.*, “Electrospun carbon nanofibers and their hybrid composites as advanced materials for energy conversion and storage,” *Nano Energy*, vol. 22, pp. 361–395, (2016).
- [66] P. Suresh Kumar *et al.*, “Free-standing electrospun carbon nanofibres - A high performance anode material for lithium-ion batteries,” *Journal of Physics D: Applied Physics*, vol. 45, no. 26, (2012).
- [67] C. Li, X. Yin, L. Chen, Q. Li, and T. Wang, “Porous carbon nanofibers derived from conducting polymer: Synthesis and application in lithium-ion batteries with high-rate capability,” *Journal of Physical Chemistry C*, vol. 113, no. 30, pp. 13438–13442, (2009).
- [68] G. Zheng, Y. Yang, J. J. Cha, S. S. Hong, and Y. Cui, “Hollow Carbon Nanofiber-Encapsulated Sulfur Cathodes for High Specific Capacity Rechargeable Lithium Batteries.”
- [69] H.-M. Lee, H.-G. Kim, S.-J. Kang, S.-J. Park, K.-H. An, and B.-J. Kim, “Effects of pore structures on electrochemical behaviors of polyacrylonitrile (PAN)-based activated carbon nanofibers,” *Journal of Industrial and Engineering Chemistry*, vol. 21, pp. 736–740, (2015).
- [70] C. Liu, F. Li, L. Ma, and H. Cheng, “Advanced Materials for Energy Storage,” *Advanced Materials*, vol. 22, no. 8, pp. E28–E62, (2010).
- [71] X. G. Zhao, E. M. Jin, J.-Y. Park, and H.-B. Gu, “Hybrid polymer electrolyte composite with SiO₂ nanofiber filler for solid-state dye-sensitized solar cells,”

- Composites Science and Technology*, vol. 103, pp. 100–105, (2014).
- [72] B.-J. Kim, Y.-S. Lee, and S.-J. Park, “A study on the hydrogen storage capacity of Ni-plated porous carbon nanofibers,” *International Journal of Hydrogen Energy*, vol. 33, no. 15, pp. 4112–4115, (2008).
- [73] R. Ramya and M. V. Sangaranarayanan, “Electrochemical sensing of glucose using polyaniline nanofiber dendrites-amperometric and impedimetric analysis,” *Journal of Applied Polymer Science*, vol. 129, no. 2, pp. 735–747, (2013).
- [74] N. J. Pinto *et al.*, “Electrospun polyaniline/polyethylene oxide nanofiber field-effect transistor,” *Applied Physics Letters*, vol. 83, no. 20, pp. 4244–4246, (2003).
- [75] M. H. Al-Saleh and U. Sundararaj, “Review of the mechanical properties of carbon nanofiber/polymer composites,” *Composites Part A: Applied Science and Manufacturing*, vol. 42, no. 12, pp. 2126–2142, (2011).
- [76] M. Zhang and J. Li, “Carbon nanotube in different shapes,” *Materials Today*, vol. 12, no. 6, pp. 12–18, (2009).
- [77] M. Inagaki, Y. Yang, and F. Kang, “Carbon nanofibers prepared via electrospinning,” *Advanced Materials*, vol. 24, no. 19, pp. 2547–2566, (2012).
- [78] N. Yusof and A. F. Ismail, “Post spinning and pyrolysis processes of polyacrylonitrile (PAN)-based carbon fiber and activated carbon fiber: A review,” *Journal of Analytical and Applied Pyrolysis*, vol. 93, pp. 1–13, (2012).
- [79] A. T. Kalashnik, T. N. Smirnova, O. P. Chernova, and V. V. Kozlov, “Properties and structure of polyacrylonitrile fibers,” *Polymer Science Series A*, vol. 52, no. 11, pp. 1233–1238, (2010).

- [80] O. Karatay, M. Dogan, T. Uyar, D. Cokeliler, and I. C. Kocum, "An alternative electrospinning approach with varying electric field for 2-D-aligned nanofibers," *IEEE Transactions on Nanotechnology*, vol. 13, no. 1, pp. 101–108, (2014).
- [81] M. Acharya, G. K. Arumugam, and P. A. Heiden, "Dual electric field induced alignment of electrospun nanofibers," *Macromolecular Materials and Engineering*, vol. 293, no. 8, pp. 666–674, (2008).
- [82] Y. Song, Z. Sun, L. Xu, and Z. Shao, "Preparation and characterization of highly aligned carbon nanotubes/polyacrylonitrile composite nanofibers," *Polymers*, vol. 9, no. 1, (2017).
- [83] W. E. Teo and S. Ramakrishna, "A review on electrospinning design and nanofibre assemblies," *Nanotechnology*, vol. 17, no. 14, pp. R89–R106, (2006).
- [84] L. Yu, Z. Shao, L. Xu, and M. Wang, "High throughput preparation of aligned nanofibers using an improved bubble-electrospinning," *Polymers*, vol. 9, no. 12, pp. 1–9, (2017).
- [85] L. Wannatong, A. Sirivat, and P. Supaphol, "Effects of solvents on electrospun polymeric fibers: preliminary study on polystyrene," *Polymer International*, vol. 53, no. 11, pp. 1851–1859, (2004).
- [86] J. A. Matthews, G. E. Wnek, D. G. Simpson, and G. L. Bowlin, "Electrospinning of Collagen Nanofibers," *Biomacromolecules*, vol. 3, pp. 232–238, (2002).
- [87] W. E. Teo, M. Kotaki, X. M. Mo, and S. Ramakrishna, "Porous tubular structures with controlled fibre orientation using a modified electrospinning method," *Nanotechnology*, vol. 16, no. 6, pp. 918–924, (2005).

- [88] P. Katta, M. Alessandro, A. R. D. Ramsier, and G. G. Chase*, “Continuous Electrospinning of Aligned Polymer Nanofibers onto a Wire Drum Collector,” (2004).
- [89] S. Park, K. Park, H. Yoon, J. Son, T. Min, and G. Kim, “Apparatus for preparing electrospun nanofibers: designing an electrospinning process for nanofiber fabrication,” *Polymer International*, vol. 56, no. 11, pp. 1361–1366, (2007).
- [90] A. Haider, S. Haider, and I.-K. Kang, “A comprehensive review summarizing the effect of electrospinning parameters and potential applications of nanofibers in biomedical and biotechnology,” *Arabian Journal of Chemistry*, (2015).
- [91] A. Koski, K. Yim, and S. Shivkumar, “Effect of molecular weight on fibrous PVA produced by electrospinning,” *Materials Letters*, vol. 58, no. 3–4, pp. 493–497, (2004).
- [92] M. G. McKee, G. L. Wilkes, R. H. Colby, and T. E. Long, “Correlations of Solution Rheology with Electrospun Fiber Formation of Linear and Branched Polyesters,” *Macromolecules*, vol. 37, no. 5, pp. 1760–1767, (2004).
- [93] H. Fong, I. Chun, and D. . Reneker, “Beaded nanofibers formed during electrospinning,” *Polymer*, vol. 40, no. 16, pp. 4585–4592, (1999).
- [94] K. H. Lee, H. Y. Kim, H. J. Bang, Y. H. Jung, and S. G. Lee, “The change of bead morphology formed on electrospun polystyrene fibers,” *Polymer*, vol. 44, no. 14, pp. 4029–4034, (2003).
- [95] Y. Liu, J.-H. He, J. Yu, and H. Zeng, “Controlling numbers and sizes of beads in electrospun nanofibers,” *Polymer International*, vol. 57, no. 4, pp. 632–636,

(2008).

- [96] G. Cadafalch Gazquez *et al.*, “Influence of Solution Properties and Process Parameters on the Formation and Morphology of YSZ and NiO Ceramic Nanofibers by Electrospinning.,” *Nanomaterials (Basel, Switzerland)*, vol. 7, no. 1, (2017).
- [97] V. Beachley and X. Wen, “Effect of electrospinning parameters on the nanofiber diameter and length.,” *Materials science & engineering. C, Materials for biological applications*, vol. 29, no. 3, pp. 663–668, (2009).
- [98] S. Y. Gu, J. Ren, and G. J. Vancso, “Process optimization and empirical modeling for electrospun polyacrylonitrile (PAN) nanofiber precursor of carbon nanofibers,” *European Polymer Journal*, vol. 41, no. 11, pp. 2559–2568, (2005).
- [99] V. Jacobs, R. D. Anandjiwala, and M. Maaza, “The influence of electrospinning parameters on the structural morphology and diameter of electrospun nanofibers,” *Journal of Applied Polymer Science*, vol. 115, no. 5, pp. 3130–3136, (2010).
- [100] K. Arayanarakul, N. Choktaweasap, D. Aht-ong, C. Meechaisue, and P. Supaphol, “Effects of Poly(ethylene glycol), Inorganic Salt, Sodium Dodecyl Sulfate, and Solvent System on Electrospinning of Poly(ethylene oxide),” *Macromolecular Materials and Engineering*, vol. 291, no. 6, pp. 581–591, (2006).
- [101] J. Du and X. Zhang, “Role of polymer–salt–solvent interactions in the electrospinning of polyacrylonitrile/iron acetylacetonate,” *Journal of Applied Polymer Science*, vol. 109, no. 5, pp. 2935–2941, (2008).
- [102] D. Fallahi, M. Rafizadeh, N. Mohammadi, and B. Vahidi, “Effect of applied

- voltage on jet electric current and flow rate in electrospinning of polyacrylonitrile solutions,” *Polymer International*, vol. 57, no. 12, pp. 1363–1368, (2008).
- [103] S. S. S. Bakar, K. C. Fong, A. Eleyas, and M. F. M. Nazeri, “Effect of Voltage and Flow Rate Electrospinning Parameters on Polyacrylonitrile Electrospun Fibers,” *IOP Conference Series: Materials Science and Engineering*, vol. 318, no. 1, p. 012076, (2018).
- [104] Y. Liu, J. Sun, and M. Zhou, “Electrospinning EPDM Oil Sorption Fiber: Effect of Solution Flow Rate,” (2010).
- [105] X. Yuan, Y. Zhang, C. Dong, and J. Sheng, “Morphology of ultrafine polysulfone fibers prepared by electrospinning,” *Polymer International*, vol. 53, no. 11, pp. 1704–1710, (2004).
- [106] C. S. Ki, D. H. Baek, K. D. Gang, K. H. Lee, I. C. Um, and Y. H. Park, “Characterization of gelatin nanofiber prepared from gelatin–formic acid solution,” *Polymer*, vol. 46, no. 14, pp. 5094–5102, (2005).
- [107] S. Tripatanasuwan, Z. Zhong, and D. H. Reneker, “Effect of evaporation and solidification of the charged jet in electrospinning of poly(ethylene oxide) aqueous solution,” *Polymer*, vol. 48, no. 19, pp. 5742–5746, (2007).
- [108] S. De Vrieze, T. Van Camp, A. Nelvig, B. Hagström, P. Westbroeck, and K. De Clerck, “The effect of temperature and humidity on electrospinning,” *Journal of Materials Science*, vol. 44, no. 5, pp. 1357–1362, (2009).
- [109] B. Barua and M. C. Saha, “Influence of humidity, temperature, and annealing on microstructure and tensile properties of electrospun polyacrylonitrile nanofibers,”

Polymer Engineering & Science, vol. 58, no. 6, pp. 998–1009, (2018).

- [110] L. Huang, N.-N. Bui, S. S. Manickam, and J. R. McCutcheon, “Controlling electrospun nanofiber morphology and mechanical properties using humidity,” *Journal of Polymer Science Part B: Polymer Physics*, vol. 49, no. 24, pp. 1734–1744, (2011).
- [111] H. Fashandi and M. Karimi, “Pore formation in polystyrene fiber by superimposing temperature and relative humidity of electrospinning atmosphere,” *Polymer*, vol. 53, no. 25, pp. 5832–5849, (2012).
- [112] B. Barua and M. C. Saha, “Studies of reaction mechanisms during stabilization of electrospun polyacrylonitrile carbon nanofibers,” *Polymer Engineering & Science*, (2017).
- [113] D. Papkov, Y. Zou, M. N. Andalib, A. Goponenko, S. Z. D. Cheng, and Y. A. Dzenis, “Simultaneously Strong and Tough Ultrafine Continuous Nanofibers,” *ACS Nano*, vol. 7, no. 4, pp. 3324–3331, (2013).
- [114] Z. Zhou *et al.*, “Development of carbon nanofibers from aligned electrospun polyacrylonitrile nanofiber bundles and characterization of their microstructural, electrical, and mechanical properties,” *Polymer*, vol. 50, no. 13, pp. 2999–3006, (2009).
- [115] Z.-M. Huang, Y.-Z. Zhang, M. Kotaki, and S. Ramakrishna, “A review on polymer nanofibers by electrospinning and their applications in nanocomposites,” *Composites Science and Technology*, vol. 63, no. 15, pp. 2223–2253, (2003).
- [116] P. Kiselev and J. Rosell-Llompart, “Highly aligned electrospun nanofibers by

- elimination of the whipping motion,” *Journal of Applied Polymer Science*, vol. 125, no. 3, pp. 2433–2441, (2012).
- [117] S. Haider *et al.*, “Highly aligned narrow diameter chitosan electrospun nanofibers,” *Journal of Polymer Research*, vol. 20, no. 4, (2013).
- [118] C. Wang, Y.-W. Cheng, C.-H. Hsu, H.-S. Chien, and S.-Y. Tsou, “How to manipulate the electrospinning jet with controlled properties to obtain uniform fibers with the smallest diameter?—a brief discussion of solution electrospinning process,” *Journal of Polymer Research*, vol. 18, no. 1, pp. 111–123, (2011).
- [119] E. Jentsch, Ö. Gül, and E. Öznergiz, “A comprehensive electric field analysis of a multifunctional electrospinning platform,” *Journal of Electrostatics*, vol. 71, no. 3, pp. 294–298, (2013).
- [120] M. S. Zarnik and D. Belavic, “An Experimental and Numerical Study of the Humidity Effect on the Stability of a Capacitive Ceramic Pressure Sensor,” vol. 21, no. 1, (2012).
- [121] F.-L. Zhou, G. J. M. Parker, S. J. Eichhorn, and P. L. Hubbard Cristinacce, “Production and cross-sectional characterization of aligned co-electrospun hollow microfibrillar bulk assemblies,” *Materials Characterization*, vol. 109, pp. 25–35, (2015).
- [122] Y. Yang, X. Zhu, W. Cui, X. Li, and Y. Jin, “Electrospun composite mats of poly[(D, L)lactide)-co-glycolide] and collagen with high porosity as potential scaffolds for skin tissue engineering,” *Macromolecular Materials and Engineering*, vol. 294, no. 9, pp. 611–619, (2009).

- [123] S. Moon and R. J. Farris, "Strong electrospun nanometer-diameter polyacrylonitrile carbon fiber yarns," *Carbon*, vol. 47, no. 12, pp. 2829–2839, (2009).
- [124] S. A. H. Ravandi and M. Sadrjahani, "Mechanical and structural characterizations of simultaneously aligned and heat treated PAN nanofibers," *Journal of Applied Polymer Science*, vol. 124, no. 5, pp. 3529–3537, (2012).
- [125] M. Yu *et al.*, "Recent Advances in Needleless Electrospinning of Ultrathin Fibers: From Academia to Industrial Production," *Macromolecular Materials and Engineering*, vol. 302, no. 7, pp. 1–19, (2017).
- [126] Y. Zheng, X. Liu, and Y. Zeng, "Electrospun nanofibers from a multihole spinneret with uniform electric field," *Journal of Applied Polymer Science*, vol. 130, no. 5, pp. 3221–3228, (2013).
- [127] F.-L. Zhou, R.-H. Gong, and I. Porat, "Needle and needleless electrospinning for nanofibers," *Journal of Applied Polymer Science*, vol. 115, no. 5, pp. 2591–2598, (2010).
- [128] F.-L. Zhou, R.-H. Gong, and I. Porat, "Polymeric nanofibers via flat spinneret electrospinning," *Polymer Engineering & Science*, vol. 49, no. 12, pp. 2475–2481, (2009).
- [129] J. Holopainen, T. Penttinen, E. Santala, and M. Ritala, "Needleless electrospinning with twisted wire spinneret," *Nanotechnology*, vol. 26, no. 2, p. 025301, (2015).
- [130] E. Kostakova, L. Meszaros, and J. Gregr, "Composite nanofibers produced by modified needleless electrospinning," *Materials Letters*, vol. 63, no. 28, pp. 2419–

2422, (2009).

- [131] G. Jiang, S. Zhang, and X. Qin, “High throughput of quality nanofibers via one stepped pyramid-shaped spinneret,” *Materials Letters*, vol. 106, pp. 56–58, (2013).
- [132] J. F. De La Mora, “The effect of charge emission from electrified liquid cones,” *Journal of Fluid Mechanics*, vol. 243, no. 1, p. 561, (1992).
- [133] C.-I. Su, Y.-X. Huang, J.-W. Wong, C.-H. Lu, and C.-M. Wang, “PAN-based carbon nanofiber absorbents prepared using electrospinning,” *Fibers and Polymers*, vol. 13, no. 4, pp. 436–442, (2012).
- [134] E. Cipriani, M. Zanetti, P. Bracco, V. Brunella, M. P. Luda, and L. Costa, “Crosslinking and carbonization processes in PAN films and nanofibers,” *Polymer Degradation and Stability*, vol. 123, pp. 178–188, (2016).
- [135] J.-H. Yun, B.-H. Kim, K. S. Yang, Y. H. Bang, S. R. Kim, and H.-G. Woo, “Process optimization for preparing high performance PAN-based carbon fibers,” *Bulletin of the Korean Chemical Society*, vol. 30, no. 10, pp. 2253–2258, (2009).
- [136] Q. Duan, B. Wang, and H. Wang, “Effects of Stabilization Temperature on Structures and Properties of Polyacrylonitrile (PAN)-Based Stabilized Electrospun Nanofiber Mats,” *Journal of Macromolecular Science, Part B*, vol. 51, no. 12, pp. 2428–2437, (2012).
- [137] H. Khayyam, M. Naebe, O. Zabihi, R. Zamani, S. Atkiss, and B. Fox, “Dynamic Prediction Models and Optimization of Polyacrylonitrile (PAN) Stabilization Processes for Production of Carbon Fiber,” *IEEE Transactions on Industrial Informatics*, vol. 11, no. 4, pp. 887–896, (2015).

- [138] S. Xiao, B. Wang, C. Zhao, L. Xu, and B. Chen, "Influence of oxygen on the stabilization reaction of polyacrylonitrile fibers," *Journal of Applied Polymer Science*, vol. 127, no. 3, pp. 2332–2338, (2013).
- [139] M. G. Dunham and D. D. Edie, "Model of stabilization for pan-based carbon fiber precursor bundles," *Carbon*, vol. 30, no. 3, pp. 435–450, (1992).
- [140] Y. J. Kim and C. R. Park, "The effect of the interaction between transition metal and precursor on the stabilization reaction of polyacrylonitrile (PAN)," *Carbon*, vol. 43, no. 11, pp. 2420–2423, (2005).
- [141] W. WATT, "Nitrogen Evolution during the Pyrolysis of Polyacrylonitrile," *Nature Physical Science*, vol. 236, no. 62, pp. 10–11, (1972).
- [142] B. Barua, "Investigation of Electrospinning Process Parameters and Studies of Stabilization Kinetics of Polyacrylonitrile-based Electrospun Carbon Nanofibers," PhD Dissertation, The University of Oklahoma, 2015.
- [143] C. Lai *et al.*, "Investigation of post-spinning stretching process on morphological, structural, and mechanical properties of electrospun polyacrylonitrile copolymer nanofibers," *Polymer*, vol. 52, no. 2, pp. 519–528, (2011).
- [144] J. . Chen and I. . Harrison, "Modification of polyacrylonitrile (PAN) carbon fiber precursor via post-spinning plasticization and stretching in dimethyl formamide (DMF)," *Carbon*, vol. 40, no. 1, pp. 25–45, (2002).
- [145] Z. Song, X. Hou, L. Zhang, and S. Wu, "Enhancing Crystallinity and Orientation by Hot-Stretching to Improve the Mechanical Properties of Electrospun Partially Aligned Polyacrylonitrile (PAN) Nanocomposites.," *Materials (Basel)*,

- Switzerland*), vol. 4, no. 4, pp. 621–632, (2011).
- [146] M. K. Jain, M. Balasubramanian, P. Desai, and A. S. Abhiraman, “Conversion of acrylonitrile-based precursors to carbon fibres,” *Journal of Materials Science*, vol. 22, no. 1, pp. 301–312, (1987).
- [147] S. Z. Wu, F. Zhang, X. X. Hou, and X. P. Yang, “Stretching-Induced Orientation for Improving the Mechanical Properties of Electrospun Polyacrylonitrile Nanofiber Sheet,” *Advanced Materials Research*, vol. 47–50, pp. 1169–1172, (2008).
- [148] S. A. Hosseini Ravandi, E. Hassanabadi, H. Tavanai, and R. A. Abuzade, “Mechanical properties and morphology of hot drawn polyacrylonitrile nanofibrous yarn,” *Journal of Applied Polymer Science*, vol. 124, no. 6, p. n/a-n/a, (2011).
- [149] A. Gupta and I. . Harrison, “New Aspects in the Oxidative Stabilization of PAN-Based Carbon Fibers: II,” *Carbon*, vol. 34, no. 11, pp. 1427–1445, (1996).
- [150] C. Liu, L. Hu, Y. Lu, and W. Zhao, “Evolution of the crystalline structure and cyclization with changing tension during the stabilization of polyacrylonitrile fibers,” *Journal of Applied Polymer Science*, vol. 132, no. 27, pp. 1–10, (2015).
- [151] S. B. Warner, L. H. Peebles, and D. R. Uhlmann, “Oxidative stabilization of acrylic fibres,” *Journal of Materials Science*, vol. 14, no. 3, pp. 565–572, (1979).
- [152] E. Fitzer and D. J. Müller, “Zur Bildung von gewinkelten Leiterpolymeren in Polyacrylnitril-Fasern,” *Die Makromolekulare Chemie*, vol. 144, no. 1, pp. 117–133, (1971).

- [153] S. B. Warner, L. H. Peebles, and D. R. Uhlmann, "Oxidative stabilization of acrylic fibres," *Journal of Materials Science*, vol. 14, no. 3, pp. 565–572, (1979).
- [154] M. R'Mili, T. Bouchaour, and P. Merle, "Estimation of Weibull parameters from loose-bundle tests," *Composites Science and Technology*, vol. 56, no. 7, pp. 831–834, (1996).
- [155] B. W. Rosen, "Tensile failure of fibrous composites," *AIAA Journal*, vol. 2, no. 11, pp. 1985–1991, (1964).
- [156] ASTM, "ASTM C3379 Tensile Strength and Young's Modulus for High-Modulus Single-Filament Materials," Philadelphia, PA, (1982).
- [157] ASTM, "ASTM D 3822 – 01 - Standard Test Method for Tensile Properties of Single Textile Fibers," *American Society for Testing and Materials*, no. November, pp. 1–10, (2014).
- [158] ASTM, "ASTM D7846 – 16 Standard Practice for Reporting Uniaxial Strength Data and Estimating Weibull Distribution Parameters for Advanced Ceramics," *American Society for Testing and Materials, West Conshohocken, Pennsylvania*, vol. i, no. January, pp. 1–17, (2000).
- [159] ASTM, "ASTM D1445 Standard Test Method for Breaking Strength and Elongation of Textile Fabrics," *American Society for Testing and Materials, West Conshohocken, Pennsylvania, USA*, vol. i, no. Reapproved, pp. 1–8, (2015).
- [160] Z. Chi, T.-W. Chou, and G. Shen, "Determination of single fibre strength distribution from fibre bundle testings," *Journal of Materials Science*, vol. 19, no. 10, pp. 3319–3324, (1984).

- [161] J. Yao and W. Yu, “Tensile strength and its variation for PAN-based carbon fibers. II. Calibration of the variation from testing,” *Journal of Applied Polymer Science*, vol. 104, no. 4, pp. 2625–2632, (2007).
- [162] H. Rinne, *The Weibull Distribution*. Sound Parkway, NJ: Taylor & Francis Group, 2005.
- [163] D. N. P. Murthy, M. Xie, and R. Jiang, *Weibull Models*, vol. 46, no. 4. Hoboken, NJ: Jhon Wiley & Sons, Inc., 2004.
- [164] W. Weibull, “A statistical distribution function of wide applicability,” *Journal of applied mechanics*, vol. 18. pp. 293–297, 1951.
- [165] W. J. Padgett, S. D. Durham, and A. M. Mason, “Weibull Analysis of the Strength of Carbon Fibers Using Linear and Power Law Models for the Length Effect,” *Journal of Composite Materials*, vol. 29, no. 14, pp. 1873–1884, (1995).
- [166] B. Moser, L. Weber, A. Rossoll, and A. Mortensen, “The influence of non-linear elasticity on the determination of Weibull parameters using the fibre bundle tensile test,” *Composites Part A: Applied Science and Manufacturing*, vol. 34, no. 9, pp. 907–912, (2003).
- [167] ASTM, “ASTM C1557 – 14 Standard Test Method for Tensile Strength and Young’s Modulus of Fibers,” *ASTM International, 100 Barr Harbor Drive, PO Box C700, West Conshohocken, PA*, pp. 1–10, (2014).
- [168] T. Ozkan, M. Naraghi, and I. Chasiotis, “Mechanical properties of vapor grown carbon nanofibers,” *Carbon*, vol. 48, no. 1, pp. 239–244, (2010).
- [169] S. Chawla, J. Cai, and M. Naraghi, “Mechanical tests on individual carbon

nanofibers reveals the strong effect of graphitic alignment achieved via precursor hot-drawing,” *Carbon*, vol. 117, pp. 208–219, (2017).

[170] S. N. Arshad, M. Naraghi, and I. Chasiotis, “Strong carbon nanofibers from electrospun polyacrylonitrile,” *Carbon*, vol. 49, no. 5, pp. 1710–1719, (2011).

[171] K. . Pickering and T. . Murray, “Weak link scaling analysis of high-strength carbon fibre,” *Composites Part A: Applied Science and Manufacturing*, vol. 30, no. 8, pp. 1017–1021, (1999).

[172] K. Naito, J. M. Yang, Y. Tanaka, and Y. Kagawa, “The effect of gauge length on tensile strength and Weibull modulus of polyacrylonitrile (PAN)- and pitch-based carbon fibers,” *Journal of Materials Science*, vol. 47, no. 2, pp. 632–642, (2012).